Abstract

Title of Dissertation: DESIGN, FABRICATION, AND TESTING OF TIME DELAY MICROMECHANISMS FOR FUZING SYSTEMS

Jing Liu, Doctor of Philosophy, 2005

Dissertation directed by: Associate Professor Don DeVoe
Department of Mechanical Engineering

Micromechanical sequential-leaf time delay mechanisms based on SOI/DRIE technology have been designed, fabricated, and characterized. The devices were designed as elements of a larger fuzing system for rifled munitions, in which a passive timing mechanism triggers at a predetermined rotational speed, followed by a desired delay time before the next element of the munition fuzing train is activated. Analytical models for the micromechanical timing mechanisms have been developed and a variety of designs was simulated from the linear and nonlinear models, and using dynamics simulation software. Fabricated mechanism arrays designed to initiate switching at centripetal accelerations from 44 to 263 g were characterized using a high-speed camera, with delay times of between 0.67 and 0.95 ms achieved for single elements within the arrays.

Measured delay times and switching accelerations follow predicted trends based on analytical and numerical models. Runaway escapement mechanism was coupled with the sequential-leaf time delay mechanisms to increase the delay time of each mechanism element. Mechanism switching at 2,000 g have been designed and simulated. The predicted delay time of each mechanism element was approximately doubled with the coupled runaway escapement mechanism.

Two types of locking mechanisms were developed to increase reliability of operation of the sequential-leaf time delay mechanisms. The fish-bone type locking mechanism had been successfully demonstrated.

A generic testing method for rotational dynamics that could image small displacement of object with high-speed off axis rotation was developed, which demonstrated for the first time of real time monitoring for rotational time delay mechanism. Image processing technology was used to improve image quality of high-speed images and extend the capability of high-speed camera to adapt to high rotation speed tests and to assist in post image analyses.

DESIGN, FABRICATION, AND TESTING OF TIME DELAY MICROMECHANISMS FOR FUZING SYSTEMS

by

Jing Liu

Dissertation submitted to the Faculty of the Graduate School of the
University of Maryland, College Park in partial fulfillment
of the requirements for the degree of
Doctor of Philosophy
2005

Advisory Committee:

Associate Professor Don DeVoe, ME Dept., Chairman / Advisor
Associate Professor Bongtae Han, ME
Professor John Melngailis, ECE
Associate Professor Peter Sandborn, ME
Associate Professor Guangming Zhang, ME

Dedication

To my mother, father, and sister who gave me enormous support from my hometown Beijing, and to my grandfather in law who passed away during my Ph. D. study in the U.S.

Acknowledgements

This dissertation is based on unselfish love and education. Numerous people devoted their time and endeavors during my grown-up time.

First of all, I would like to thank my mother, father, and sister who have been providing the best support they can throughout my education. I must also thank my former teachers in primary school, middle school, high school, and universities in China who put countless time and endeavors on my education. My city, Beijing shaped the basic frame of my character with enormous information, resources, and opportunities.

My understanding and capability of using engineering knowledge have been leveraged to a new level during my study in the University of Maryland, College Park. I get to know so many friends from all over the world here. Thanks Dr. Don DeVoe, my advisor who helped and directed me to finish this dissertation. Those discussions and emails are self-explaining of his efforts.

Thanks those people who helped me in my study, research, and daily life both in China and in U.S.

Table of Contents

List of Tables

List of Figures

Chapter 1 - Introduction

1.1 Background and Motivation

In the context of military explosive systems or devices such as munitions, a fuze is a device, which prevents premature arming of the explosive during storing, handling, and transportation. For munitions, fuzing may also prevent arming during the process of launching or emplacing, while ensuring that the explosive becomes armed when appropriate. Generally, it is desirable to sense the munition environment in order to sense the point in space or time at which arming is to occur, and affecting such arming [1]. Safety and arming (S&A) devices that provide the functionality for fuzing systems are currently developed, stocked, and issued as individual end-items, which must be assembled and integrated to realize the fuzing system [1]. However, this approach leads to high system cost and large system volume, which presents a significant challenge for next generation weapons which require a radical approach in which S&A devices will be required to have ultra-miniature size (less than 0.5 $inch^3$), low cost (under $10/unit), and producible at high volume, (~1 million units/year) [2]. Recently, MicroElectroMechanical Systems (MEMS) technology has been leveraged as an enabling approach to next-generation S&A systems. MEMS offers the capability of integrating mechanical and electronic sensors and actuators on a single substrate. The batch processing capability of MEMS technology makes large volume production of MEMS systems feasible, thereby providing significant reductions in system cost. A number of researchers have utilized MEMS technology to develop S&A components. In addition to providing on-chip actuators for aligning detonation trains [3], MEMS sensors for

monitoring the munition environment have been described. Air Force Research Laboratory (AFRL) developed single crystal 6H-SiC piezoresistive accelerometers for high-g application. 40,000 g safe operation had been testified. Sensitivities ranging between 50 and 343 nV/g were measured for differing accelerometer sensing elements [4][5]. Non-powered shock sensor that latched above a predetermined threshold acceleration had been developed at Naval Surface Warfare Center (NSWC). Sensors responding to shock from 30 g to 1,100 g and surviving up to 30,000 g had been demonstrated [6]. NSWC also developed differential pressure flow sensor [7], which senses the pressure difference created by fluid momentum. The fluid momentum is created by flow drawn into the flow ports of a body due to viscous force interaction between the body and the fluid. The differential sensor is a commercial off the shelf product from Honeywell. The NSWC shock sensor senses the launch acceleration environment and differential pressure flow sensor senses the water flow pressure environment. Upon sensing these two separate and independent environments, respective locks are deactivated and the munition is ready for firing and moves from safe state to armed state. A MEMS optical switched with integrated optical switch is then closed after receiving signal from environmental sensor. The optical detector will output 80-100 mA, 5 V electrical signal to initiate micro power electronics [8][9]. These MEMS sensors and devices serve to change the munition state from safe state to armed state, and firing. However, to prevent the munition from detonating in the early launch stage and endangering safety of launch vehicle and launch people, these MEMS devices, except the shock sensor are not allowed to work unless the munition leaves the launch barrel for certain amount of time or certain safe distance. A MEMS timer that can be integrated

with other S&A devices is desired to provide timing for this period.

One key measurand that may be used to monitor the environment for rifled munitions is the rotation rate. Upon firing, rifled munitions experience a rapid linear acceleration along the full barrel length, with a corresponding angular acceleration about the firing axis, with the maximum linear and angular velocities reached upon exit from the barrel. To prevent premature detonation, rotation speed may be measured, and the munition arms only after reaching some percentage of the maximum rotation rate. Furthermore, it is desirable to arm the munition after it has reached a safe distance from the launch site. To this end, a timing mechanism that is initiated at a set rotation rate may be used as an element in the arming train between sensing the launch conditions and arming the explosive. While simple electronic timers would certainly be sufficient for this application, they require an active power source that is not suitable for military applications where the munition may be stored for over 20 years. Furthermore, electronic components may be susceptible to hostile electromagnetic interference designed to jam or damage the timer. Thus, a purely mechanical time delay device that operates in a passive mode is required for many applications.

To be suitable for a wide range of rifled munitions, the time delay mechanisms must be able to trigger at centrifugal accelerations up to 2,000 g, with required time delays ranging from around 10 ms to several hundred ms, depending on the final barrel speed. Conceptually, the time delay mechanism undergoes a two-stage working environment, consisting of a launch stage and a sustaining stage. During the launch stage, the munition is subjected to accelerations in the munitions axial direction. Figure 1 shows three acceleration curves of linear acceleration, angular acceleration, and centrifugal

acceleration of typical projectile. It could be seen from the acceleration curves that inside the launch barrel, the projectile undergoes high initial linear and angular accelerations. After the peak point, these accelerations decrease until projectile goes out of the launch barrel. The angular acceleration is approximately proportional to the linear acceleration. It is noted that when the munition leaves the launch barrel, the linear and angular accelerations do not go to zero immediately. The gas goes out of the launch barrel continue propelling the munition in a very short period. After this short period, those accelerations drop to zero. The centrifugal acceleration, however, is proportional to square of angular velocity. Unlike the linear acceleration curve and the angular acceleration curve, the centrifugal acceleration keeps increasing until the munition leaves the launch barrel and then keeps approximately constant value. For self-propelled munitions, like missiles or rockets, the linear accelerations inside launch barrel do not increase as sharp as that for projectile. After leaving the launch barrels, their engines propel the munitions forward. They typically experience low-to-medium acceleration, for example from 5 g to 5,000 g [1]. The launch environment of interests here is the projectile launch environment [1].

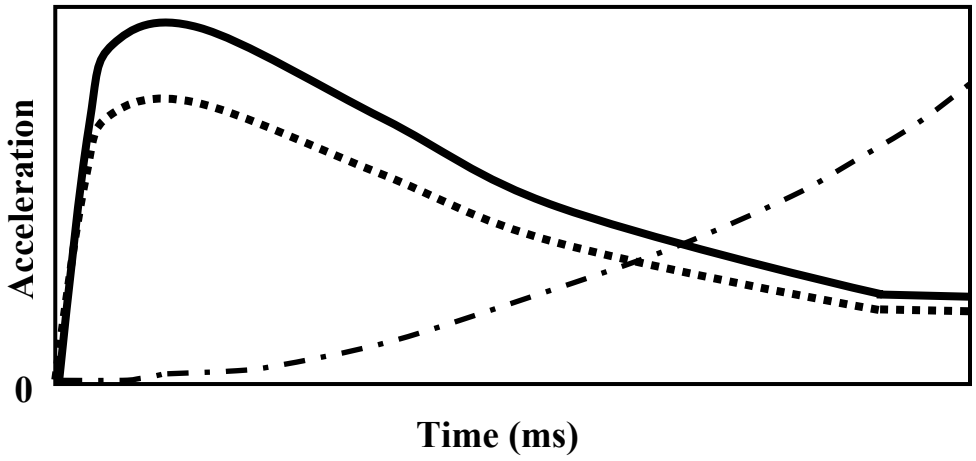

Figure 1 Munition launch environment (linear acceleration (—), angular acceleration (···), and centrifugal acceleration (-·-).

During the launch stage, the rotation speed of the projectile is accelerated approximately linearly from 0 g to peak value. In the next 10-15 ms after exiting the launch barrel, the munition rotation speed remains unchanged during the sustaining stage. The influences of air resistance and gravity on the munition rotation are generally negligible during this stage over the relevant time period of interest for the S&A system. Near the end of the launching stage, if, for example a point of 80% of the peak centrifugal acceleration is picked from the centrifugal acceleration curve, it could be estimated for a given projectile that it reaches the end of the launch stage. This threshold projectile centrifugal acceleration (rotational speed) could be used to trigger the time delay mechanism. Once the time delay mechanism is initiated, it will continue to work under the successive constant projectile rotation during the projectile sustaining stage. For different projectiles, different numbers will be chosen as the threshold points to initiate the time delay mechanism according to their specific acceleration curves.

While a number of macro-scale time delay mechanisms have been developed and

integrated into existing fuzing systems, the primary goal of this dissertation is to investigate the feasibility of micro-scale time delay mechanisms based on silicon microfabrication technology, which can meet the requirements of next-generation S&A systems. The specific goal of this dissertation is to develop a pure mechanical micro time delay mechanism for rifled torpedo as one component of MEMS S&A system. Ideally, this micro time delay mechanism is capable of providing delay time in the order of millisecond or longer under the munition launch environment, which includes initiating near the maximum munition rotation speed and responds to sustained rotation.

In order for the micro time delay mechanism to be integrated with other MEMS based S&A components, high-aspect-ratio processing techniques need to be adapted. Both LIGA [10] and SOI/DRIE [10] processing techniques have been evaluated on other type of S&A components for Canistered Countermeasure Anti-torpedo Torpedo (CCAT) [7]. Because of the additional electroplating and molding processes, the dimension tolerance of LIGA processing technology is not as good as that of SOI/DRIE processing technology. The cost for LIGA processed mechanism is approximately five times as DRIE processed mechanism [7]. As a result, the SOI/DRIE processing technology was selected to realize the micro time delay mechanism. Although the SOI/DRIE fabrication technology had been widely used in processing MEMS devices, its design dependent features requires processing exploration from both design and fabrication aspects.

It is necessary to develop measurement technologies to capture vibration dynamics of micro time delay mechanism rotating in high-speed, with resolution in the order of tens of micrometer. The time resolution need to be achieved is in the order of sub millisecond.

1.2 Macro-Scale Time Delay Mechanism

A number of macro-scale time delay mechanisms have been developed for use in S&A systems. Rotary-type time delay mechanisms, in which each element within the mechanism chain is anchored to the substrate by an in-plane torsional spring, have been designed to trigger by both centrifugal and linear launch forces [1][5]. Similarly, escapement mechanisms have been used to regulate displacement and "escape" energy at a controlled rate to produce a desired delay time [1]. Since the 1960's, so-called runaway escapements, in which rotation of a gear train is regulated by an inertial pallet, have been extensively studied both theoretically and experimentally [13]-[17]. Gearless-type runaway escapements which replace the functionality of the gear train with a larger and unbalanced pallet inertia, have also been developed [18][19]. A related mechanism is the tuned escapement, such as Junghan's escapement design, [20]-[22], in which the oscillation frequency of a pallet is regulated by an attached spring and is independent of the magnitude of the driving torque.

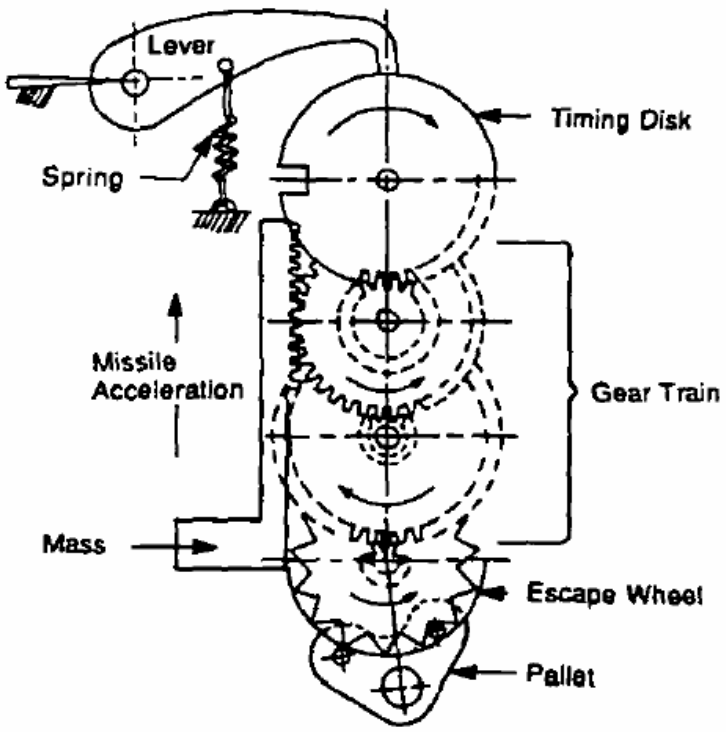

Figure 2 Runaway escapement ([1]).

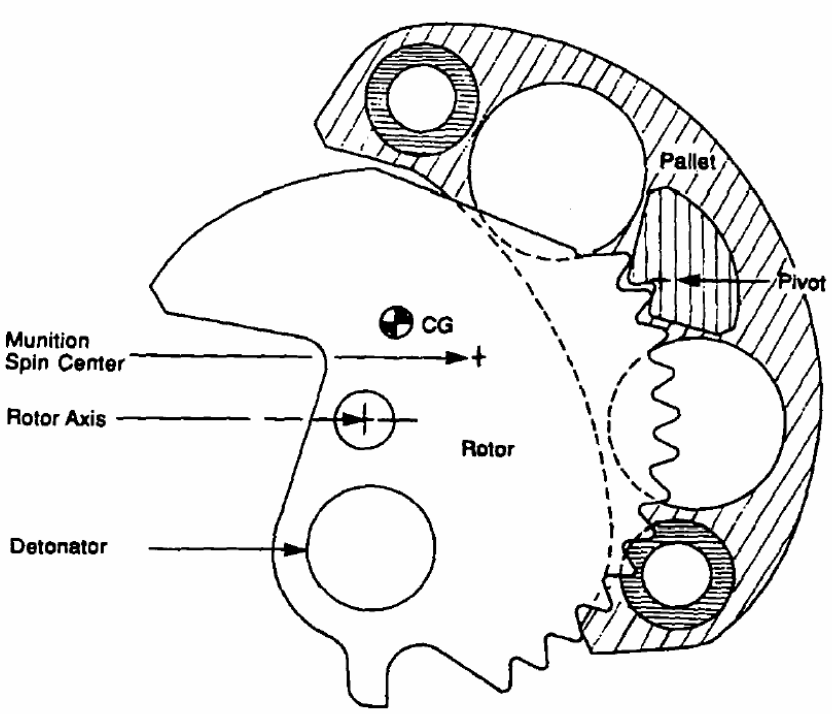

Figure 3 Gearless mechanism ([1]).

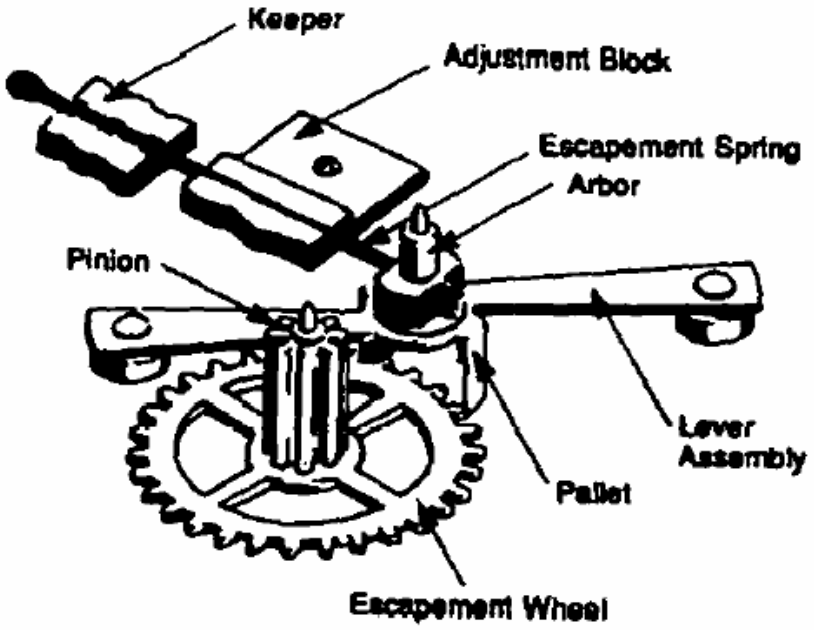

Figure 4 Junghan's escapement ([1]).

Sequential leaf time delay mechanisms, as depicted in Figure 5, belong to the class of rotary-type mechanisms. Sequential leaf mechanisms have been designed to respond to linear accelerations in the direction of the launch barrel axis [1]. These mechanisms consist of a series of interlocked elements, with each element pivoted for angular displacement about the pivot, and held in position using a torsional spring. Initially, each element in the series is constrained from rotating by its previous neighbor in the series, with the exception of the first element. Under the action of a sustained linear acceleration, the first element rotates under the action of its own inertial load. When a critical angle is reached, the second element becomes unconstrained and begins rotating. This sequence continues until the last element finishes its rotation and releases other components in the fuzing train.

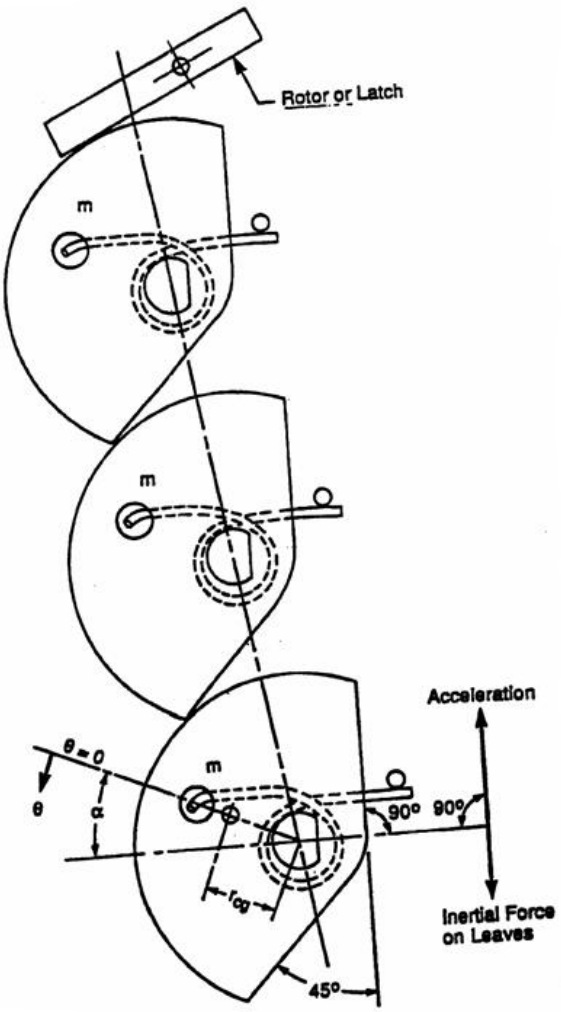

Figure 5 Sequential leaf time delay mechanism.

The dynamics of the elements define the time required for each leaf to rotate through its critical angle. By properly selecting the springs, inertial masses, and number of elements, a desired delay time may be achieved. Furthermore, since the first element in the sequence determines the acceleration required to reach the first critical angle, proper design of the first element will define the rotational speed at which the dynamic chain is triggered. Sequential leaf time delay mechanisms are primarily used in the S&A systems of projectiles to respond to linear launching acceleration. Examples are M532 S&A

system and 8-inch Semi-Active Laser Guide Projectile (SALGP) S&A system, which are used to respond to acceleration of 500 g to 900 g and 1,000 to 1,500g. They ensure that the S&A system will change from safe state to arm state only if the acceleration lasts for a sufficient period of time. They also provide safety against arming caused by accidental handling accelerations of short duration, i. e. dropping. They usually consist of three leaf elements [23].

1.3 Micro-Scale Time Delay Mechanism Overview

Microfabrication has been widely applied to the development of safety and arming systems, which sense the environment of a munition and arm the explosive at the appropriate point in space or time. Examples of recent efforts in this arena include optical microswitches for detonator charging [11], micromechanical energy interrupters [23], and integrated sensors capable of monitoring the munition environment [25].

Recently, a microfabricated escapement mechanism for projectile fuzing applications was described using both SOI/DRIE and LIGA methods [3]. These escapement devices were first fabricated using microfabrication methods and then assembled, including pre-tensioning spring to store energy prior to releasing a slotted peg. The following figures show the safe state and arm state of the escapement after experiencing the launch environment, 45,000 g linear peak linear acceleration and 490 rps in a 20 mm diameter munition. In order for the transfer charge to move to the armed position, the setback slide needs to go downward against spring tension and zig-zag delay timing and lock and disengage the setback lock lever from the arming slider under linear

acceleration [3]. After the command slider clears its foot overhanging in the arming slider by the expansion of propellant charge, the arming slider moves to the right against spring tension and latches under the influence of continued centrifugal acceleration, putting the transfer charge in the armed position [3]. Typical device size is approximately 12×15 mm [3]. The spring force, peg inertia, and frictional interactions with the slot determined the delay time. Although time delay measurements were not reported, overall operation of the devices was demonstrated in tested munitions.

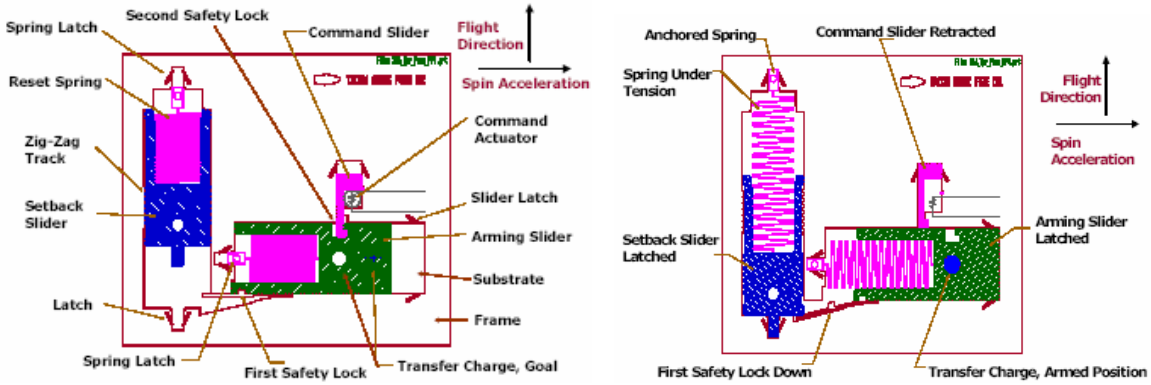

Figure 6 Schematic of MEMS based S&A device (safe state – left and armed state – right).

For rifled munitions, which can experience high rotation rates, spin rate provides a highly effective measurand that can be used to initiate the arming cycle. This dissertation addresses the development of a silicon-based rotation rate switch as a new S&A sensor, combined with a micromechanical timing mechanism to provide the desired delay between munition launch and arming.

Mechanical time delays are commonly used in existing S&A systems to prevent accidental arming before achieving a safe distance from the launch site. MEMS

technology offers the potential to significantly reduce size and cost of these systems. Many different passive mechanical timing mechanism designs have been extensively evaluated, and several candidate designs were considered during the course of this work. While several designs will be discussed in the following chapters, the sequential leaf design shown previously in Figure 5 is particularly attractive for miniaturization. Not like the escapement designs, in the sequential leaf design, the profile of contact surfaces between adjacent leaf elements are point to regular surface contact, not irregular surface to irregular surface contact. The profile of contact surfaces do not need to be specifically considered, which require precision match to prevent the moving mechanism from being self-locked due to poor surface profile match. The precision match requirement challenges fabrication tolerance of high-aspect-ratio micro devices. In the escapement design, the necessary element rotation angle during each effective match is large in order to avoid self-locking phenomenon. Realizing large rotation angle on suspended MEMS device demands high on element suspension spring design. Whereas the sequential leaf design does not have such constraint, which allows low acceleration proof tests to be done without high demanding testing environments. Another benefit of adopting the sequential leaf design is that contacts and frictions between adjacent leaf elements do not vary in direction, which makes it easy to build theoretical model to describe vibration dynamics. Thus, this remainder of this dissertation is primarily focused on the design, fabrication, and characterization of mechanical time delay systems derived from the sequential leaf concept. There are several key differences between the traditional sequential leaf design and the microscale devices investigated here. First, while the macro-scale design was developed for non-rifled munitions and operates with a linear

acceleration in the direction of the projectile axis [1][26], the micro-scale design is extended to respond to centrifugal acceleration resulting from munition rotation.

More fundamentally, several design challenges were presented by the need for miniaturization. While the configurations of the micro-scale sequential leaf time delay mechanism explored in this work are conceptually similar to their macro-scale counterparts, one underlying difference comes from the configuration of the element pivot. In the macro-scale mechanism, each element is connected to the substrate by a revolute joint and balanced by a torsional spring centered at the pivot. In the micro-scale mechanism, the true revolute joints are replaced with pseudo-revolute compliant joints, with each element anchored by a compliant element, which also serves as a nonlinear spring. Each inertial element consists of a fan-shaped seismic mass suspended above the substrate by the compliant beams, which share a common anchor point. A schematic diagram of the basic micromechanism configuration is shown in Figure 7 for a 3-stage time delay device.

Labor-intensive assembly work needs to be conducted for the macro-scale mechanism after fabrication of every element and torsional spring. On the contrary, no assembly work needs to be done after micro-scale device is fabricated, which saves time and reduces cost. The materials of the elements and the torsional springs are different for macro-scale mechanism. In the micro-scale mechanism fabricated on SOI wafers, both of them are made from silicon material. The size and dimension tolerance of the macro-scale mechanism are constraint by macro fabrication technology. In the micro-scale mechanism, device size is allowed to be much smaller. The dimension tolerance is determined by micro fabrication technology and is much smaller. The assembly tolerance

does not need to be considered in the micro-scale mechanism, which contribute to improve the entire mechanism tolerance. Due to the one mask SOI/DRIE fabrication technology adapted, the shape of the components of micro-scale mechanism that can be fabricated does not have the same constraint as the macro-scale mechanism.

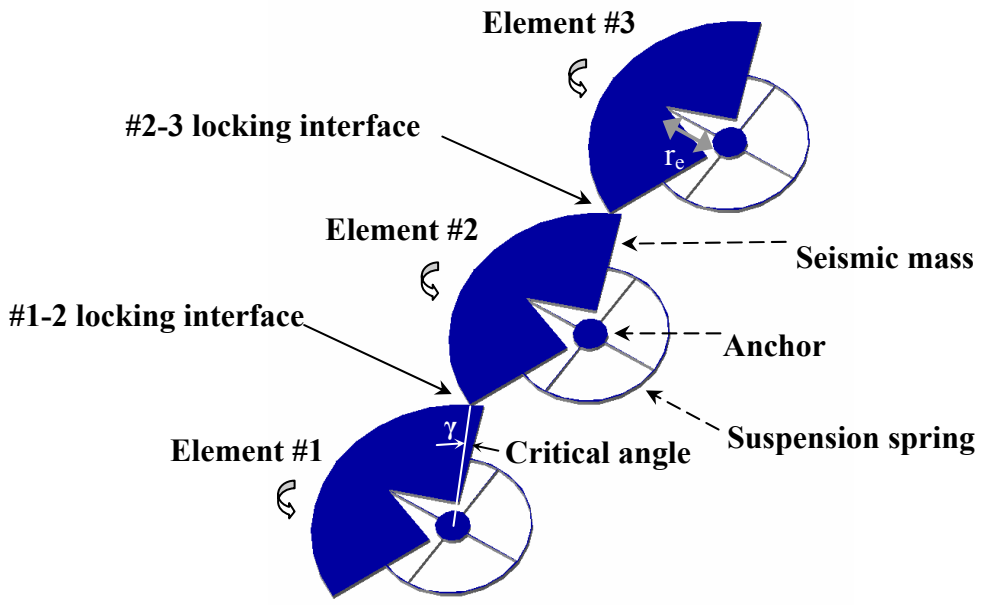

Figure 7 Schematic of a three-element leaf time delay mechanism.

1.4 Thesis Organization

The remainder of this dissertation is organized in the following manner. In Chapter 2, device design issues are addressed, including the development of analytic and numerical models for device dynamics, which incorporate nonlinear spring designs and relevant damping mechanisms including inter-element friction. Chapter 3 details the fabrication process used to realize a variety of device designs. In Chapter 4 device

testing, testing methodology, testing improvement as well as testing results are described. Chapter 5 focuses on optimizing device performance, attempts to improve device delay time, locking mechanisms to increase device reliability, and mass release mechanism design for possible mechanism interfacing. Chapter 6 introduces an all-fiber optical switch that can be applied with the micro time delay mechanism for fuzing. Chapter 7 summarizes achieved results and future work.

Chapter 2 – Device Design

Design of the time delay mechanism started from miniaturizing clock and watch escapement mechanisms to explore the constraints of miniaturizing escapement mechanisms. Sequential leaf time delay mechanism without these constraints was selected for miniaturization. Full non-linear analytical dynamic model that considering non-linear suspension spring, friction and air damping was developed for the sequential leaf micro time delay mechanism. Linearized model was derived for evaluation purpose at design stage. The linearized model was validated with numerical dynamic simulation conducted with dynamic simulation software ADAMS. Different designs were calculated from the dynamic models for testing.

2.1 Escapement Mechanism Design

Many clock, watch, and timer escapement mechanisms have been developed for timing purposed in the past, such as Graham escapement, recoil escapement, Swiss lever, Brocot escapement, pin wheel escapement, runaway escapement and Junghan's Escapement [20][27][28][29].

In these escapements, energy from escapement wheel is escaped at controlled rate determined by mass and configuration of escapement pallet, the escapement wheel and profile of contact surfaces between the escapement wheel and the escapement pallet. The Graham escapement, as an example, experiences a few vibration stages during one cycle of controlled energy escapement procedure. As seen form Figure 8, the escapement wheel

and the escapement pallet are designed to rotate around their respective rotation centers. Torque is applied on the escapement wheel to rotate it in clockwise (CW) direction. In Figure 8(a) and Figure 8(b), the escapement pallet rotates counter clockwise (CCW). The escapement wheel is prevented from rotating forward and locked in position. Under the action of restoring spring torque applied on the rotation axis of the escapement pallet, the escapement pallet starts to rotate CW, which unlocks the escapement wheel and allows it to continue rotating CW. The tooth of unlocked escapement wheel interacts with that on the escapement pallet and impulse it to move CW, Figure 8(c) and put it to drop into a locked position that stops the escapement from continue moving CW, Figure 8(d) and Figure 8(e). The escapement pallet torsional spring releases the locked escapement wheel and rotates the escapement pallet CCW. After an impulsion process by the escapement wheel, Figure 8(f), the entire escapement goes back to the state depicted in Figure 8(a) and another vibration cycle is started over.

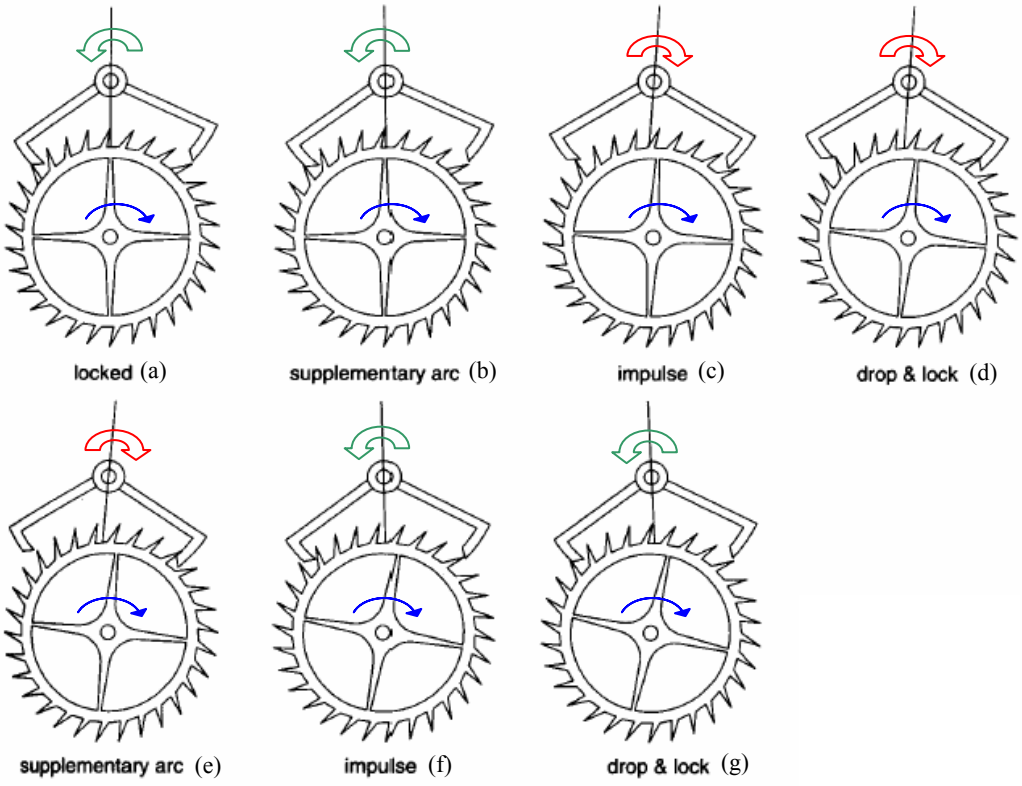

Figure 8 Operation of Graham escapement ([28]).

To study torque transfer procedure of the Graham escapement, numerical dynamics simulations were conducted by using numerical simulation software ADAMS. In the numerical model, the escapement wheel and the escapement pallet are allowed to rotate around their own rotation axes. After applying driving torque on the escapement wheel, vibrations of the escapement pallet and the escapement wheel were simulated.

It was found from the numerical simulation results that the Graham escapement is sensitive to the variations of driving torque applied on the escapement wheel. Quite easily, the mechanism was locked due to contact and interaction between escapement wheel teeth and escapement pallet teeth. The escapement vibration process becomes irregular, i.e., the energy escapement procedure could not be controlled. Other escapement

mechanisms that require high on tooth profile designs were also studies using numerical simulations. The escapement design that is most tolerant to input torque variation is the runaway escapement. As a result, the runaway escapement was investigated.

Similar to the Graham escapement, the runaway escapement is comprised of an escapement wheel and an escapement pallet. Driving torque is applied on the rotation axis of the escapement pallet. Under the action of this driving torque, the escapement pallet vibrates to escapement the diving energy. Different from the Graham escapement design in which the energy escapement is mainly controlled by the lock stage in the escapement pallet vibration procedure, the energy escapement in a runaway escapement is controlled by the moment of inertia of the escapement pallet and there is no lock stage in the escapement pallet vibration procedure. A few runaway escapement examples are shown in Figure 9.

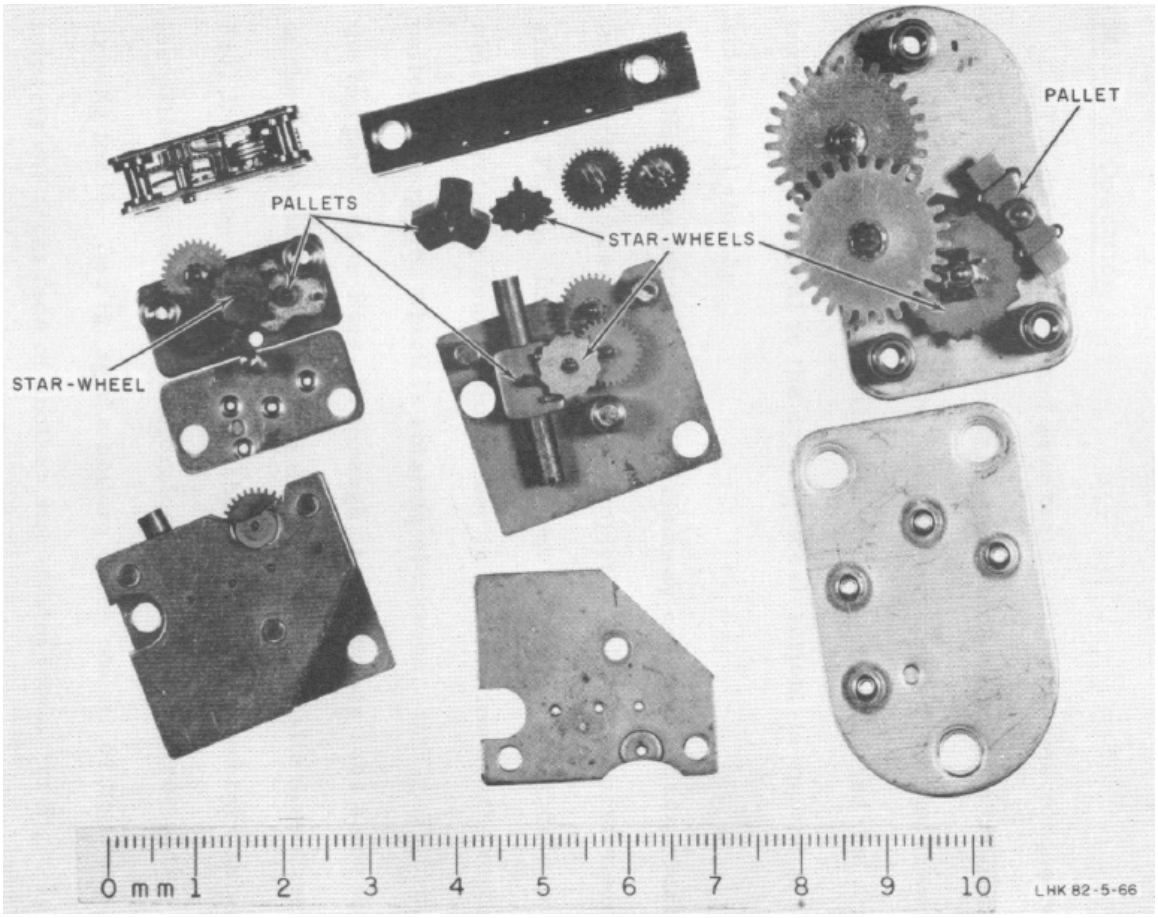

Figure 9 Examples of runaway escapement ([13]).

To design the runaway escapement, both theoretical analytic modeling and numerical dynamics simulations were conducted to find its time delay and dynamic vibration properties.

The delay time of the runaway escapement, T_{delay}, is described by the following equation from which the delay time from one escapement vibration cycle is calculated [18][30].

$$T_{delay} = \sqrt{\frac{2I_{pallet}\theta_{\max}}{(M_{wheel} - f_{wheel})/n^{*} - M_{b} - f_{pallet}}} \tag{2.1}$$

$$\boldsymbol{M_b = m_{wheel}\omega^2 r_s r_p \sin\psi} \tag{2.2}$$

the parameters in the above equations are listed as follows:

I_{pallet}: moment of Inertia of escapement pallet;

θ_{max}: maximum rotation angle of escapement pallet;

M_{wheel}: torque on escapement wheel;

M_b: bias torque from rotation;

f_{wheel}: spring force from escapement wheel suspension structure;

f_{pallet}: spring force from escapement pallet suspension structure;

n*: torque transmission ratio between escapement wheel and escapement pallet;

m_{wheel}: escapement wheel mass;

ω: spin rate of escapement unit;

r_s: center of gravity offset from pivot of escapement pallet;

r_p: escapement pallet pivot offset from spin axis;

ψ: included angle between and r_s and r_p .

Numerical simulations were conducted to verify the theoretical delay time results and to obtain vibration dynamics of both the escapement wheel and the escapement pallet. The following figure shows a typical vibration procedure.

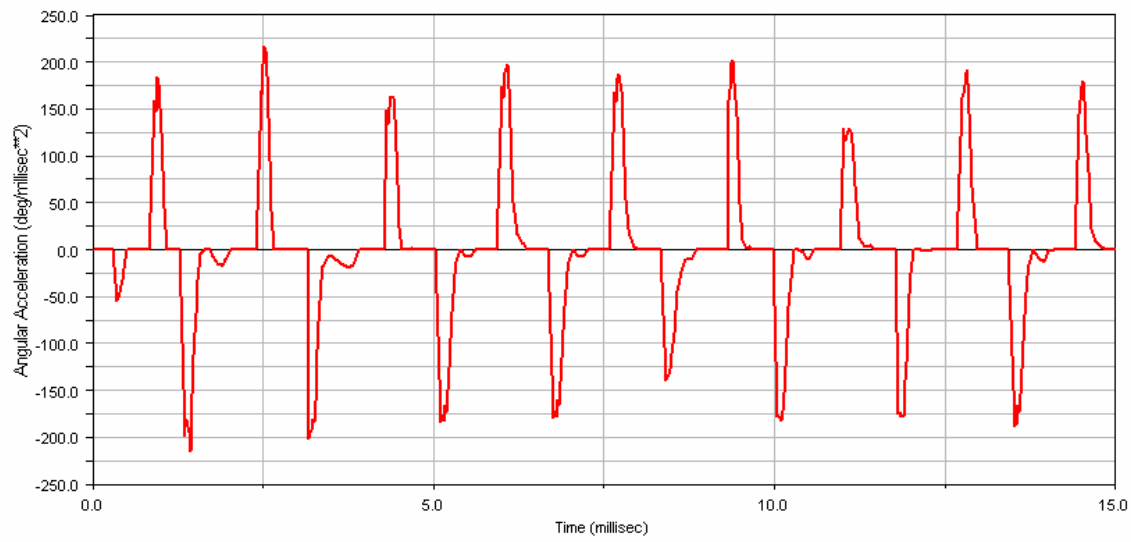

Figure 10 Vibration dynamics of a runaway escapement.

Y-axis in the figure reflects the angular acceleration of the escapement pallet. Positive angular acceleration value indicates vibration of the escapement pallet in CW direction from the equilibrium position. The negative value indicates vibration of the escapement pallet in the CCW direction from the equilibrium position. The time difference between peak angular acceleration values is the delay time of that acceleration cycle of the runaway escapement. The delay time is approximately 1.5 ms in this specific simulation and it matches the theoretical result.

Compared to other escapement designs, the runaway escapement is more suitable to work in the environment where driving torque may change. However, there are a few reasons that makes it not ideal for miniaturization. The more demanding geometry tolerance on matching profiles of miniaturized mechanism makes the energy escapement procedure difficult to realize. The influence of centrifugal force on the suspended microfabricated device makes precision match between mechanism elements more

difficult to realize in rotational environment. In order to keep enough tolerance on matching profiles, the rotation angles of the escapement wheel in one vibration cycle are large and could not be easily realized in the microfabricated device. As a result, sequential leaf mechanism design that is less demanding on these constraints was considered.

2.2 Sequential Leaf Mechanism Design

Unlike the escapement mechanism design described in the previous section, the sequential leaf mechanism discussed in Sections 1.2 and 1.3 offers several benefits, which make the design more suitable for miniaturization via silicon microfabrication. The sequential leaf mechanism does not require the same level of precision match as required between escapement wheel and escapement pallet in an escapement mechanism. The rotation algle of element suspension spring of the sequential leaf mechanism is not necessarily as large as in an escapement mechanism, which is in to be realized using microfabricated torsional suspension spring.

The microscale sequential leaf time delay mechanism dynamics have been investigated both theoretically and numerically. Theoretical analyses considering element friction and air damping were conducted on single mechanism element. Element vibration dynamics and theoretical single element time delay was obtained from out of the theoretical dynamic model. To consider the influence of contact between mechanism elements, dynamic simulations using ADAMS were studied. The simulation results testified the interlocking nature of multiple-element leaf time delay mechanism. Element

vibration dynamics, switching speed as well as time delay were obtained through the full model simulations, which considered element friction and element contact. The theoretical delay times of a single mechanism were compared with those from numerical ADAMS simulation results.

2.2.1 Analytical Dynamics Model

Followings are the nomenclatures used to derive the analytical dynamica model.

P: element carrier rotation center;

O: pivot point of element on element carrier;

r_c: distance from O to P;

r_e: element radius;

$\underline{\hat{\boldsymbol{c}}}_1$, $\underline{\hat{\boldsymbol{c}}}_2$: unit vectors of element carrier coordinate system;

$\underline{\hat{\boldsymbol{e}}}_1$, $\underline{\hat{\boldsymbol{e}}}_2$: unit vectors of element coordinate system;

T: kinetic energy;

T_c: kinetic energy of element carrier;

T_e: kinetic energy of element;

V: potential energy;

D: Rayleigh dissipation function;

Q: generalized force;

$\theta_{c:}$ element carrier rotation angle with respect to ground reference;

θ_e: element rotation angle with respect to ground reference;

$\omega_{c:}$ element carrier rotation angle with respect to ground reference;

ω_e: element rotation angle with respect to ground reference;

$\underline{L_e}$: vector connects element *C.G.* and element carrier rotation center *P*;

m_c: mass of element carrier;

m_e: mass of element;

I_c: element carrier moment of inertia;

I_e: element moment of inertia;

α: orientation of unit vector $\underline{\hat{e}_1}$ with respect to line *P*-*O*;

α_0: angle between line *P*-*O* and line *C.G.*-*O*;

k: torsional spring constant of element suspension spring;

$c_{air\_camping}$: damping coefficient that considering air damping effect;

$Q_{friction}$: friction torque applied on one element by adjacent element;

ω_n: natural resonant frequency;

θ_{sta_eqi}: static-equilibrium position;

k_{const}: linear spring constant;

γ: critical angle;

t_{delay}: element delay time;

L_{e1}: distance from *C.G.* of element #1 to element carrier rotation center;

d_{1a}: distance from element #1 rotation center to line connecting *C.G.* of element #1 to *C.G.* of the element carrier;

β: angle between line connecting element #1 rotation center to element #1 *C.G.* and the shortest line from element #1 rotation center to line from element #1 rotation center to element carrier rotation center;

f_{21}: friction force applied on element #1 by element #2;

f_{32}: friction force on applied on element #2 by element #3;

F_{12}: normal force applied by element #2 on element #1;

F_{32}: normal force applied by element #2 on element #1;

μ_{dyn}: dynamic friction coefficient;

μ_{sta}: static friction coefficient;

I_{center}: moment inertia of element #1 with respect to its center of rotation;

ψ: element carrier angular acceleration;

τ: shear stress;

μ: viscosity of air;

v: element linear velocity;

h: gap between element and substrate;

R_2: outer radius of element;

R_1: effective inner radius used to account for notch removed from element to provide connection to suspension spring;

C_{air}: damping coefficient;

T_{spring}: restoration torque of suspension spring.

The idealized geometry of a sequential leaf timing mechanism used as the basis for developing an analytic dynamics model is shown in Figure 11. The element carrier rotates with respect to ground reference around a fixed rotation center P. The mechanism element is pivoted at O on the element carrier, with distance r_c away from the element carrier rotation center P.

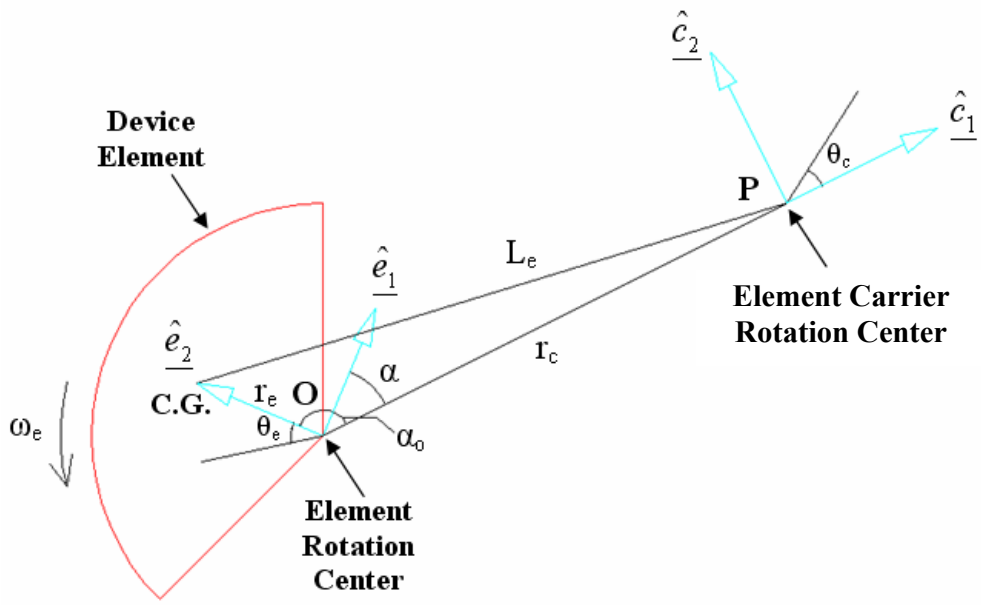

Figure 11 Sequential leaf element (theoretical derivation).

To derive an analytic model for the system dynamics, two coordinate systems are introduced. The first coordinate system is defined by two perpendicular unit vectors $\underline{\hat{\boldsymbol{c}}_1}$ and $\underline{\hat{\boldsymbol{c}}_2}$, which rotate with the leaf element carrier. The other coordinate system is defined by two perpendicular unit vectors $\underline{\hat{\boldsymbol{e}}_1}$ and $\underline{\hat{\boldsymbol{e}}_2}$ that rotate with the leaf element.

A Lagrangian approach [31] was used to derive the theoretical element vibration dynamics. From the Lagrangian, the equation of motion is given by,

$$\frac{\boldsymbol{d}}{\boldsymbol{dt}}\left(\frac{\partial \boldsymbol{T}}{\partial \dot{\theta}_i}\right)-\frac{\partial \boldsymbol{T}}{\partial \theta_i}+\frac{\partial \boldsymbol{V}}{\partial \theta_i}+\frac{\partial \boldsymbol{D}}{\partial \dot{\theta}_i}=\boldsymbol{Q}_i \quad \boldsymbol{i}=\boldsymbol{e},\boldsymbol{c} \tag{2.3}$$

In equation (2.2), T is kinetic energy, V is potential energy, D is the Rayleigh dissipation function, and Q_i is generalized force. θ_e and θ_c are the rotation angles of the element and element carrier with respect to the ground reference.

Kinetic energy T is the summation of translational and rotational kinetic energy of the element (T_e) and the element carrier (T_c).

$$\begin{aligned}
\boldsymbol{T} &= \boldsymbol{T}_e + \boldsymbol{T}_c \\
&= \left[\frac{1}{2}\boldsymbol{m}_e \underline{\boldsymbol{v}_e}^2 + \frac{1}{2}\boldsymbol{I}_e \underline{\omega_e}^2\right] + \left[\frac{1}{2}\boldsymbol{m}_c \underline{\boldsymbol{v}_c}^2 + \frac{1}{2}\boldsymbol{I}_c \underline{\omega_c}^2\right] \\
&= \frac{1}{2}\boldsymbol{m}_e \underline{\boldsymbol{v}_e}^2 + \frac{1}{2}\boldsymbol{I}_e \underline{\omega_e}^2 + \frac{1}{2}\boldsymbol{I}_c \underline{\omega_c}^2 \\
&= \frac{1}{2}\boldsymbol{m}_e \underline{\dot{\boldsymbol{L}}_e} \cdot \underline{\dot{\boldsymbol{L}}_e} + \frac{1}{2}\boldsymbol{I}_e \dot{\theta}_e^2 + \frac{1}{2}\boldsymbol{I}_c \dot{\theta}_c^2
\end{aligned} \tag{2.4}$$

The translational kinetic energy of the element is obtained through self-dot product of the time derivative of vector $\underline{L_e}$, which connects the element center of gravity

(*C.G.*) and element carrier rotation center *P*. In the equation, m_e, I_e, m_c, and I_c are the mass and moment of inertia of element and element carrier, where,

$$\begin{aligned} \omega_e &= \dot{\theta}_e \\ \omega_c &= \dot{\theta}_c \end{aligned} \tag{2.5}$$

are angular velocities of element and element carrier with respect to the ground reference.

$$\underline{\boldsymbol{L_e}} = -\boldsymbol{r_c}\underline{\hat{\boldsymbol{c}}_1} + \boldsymbol{r_e}\underline{\hat{\boldsymbol{e}}_2} \tag{2.6}$$

$\underline{L_e}$ is expressed within the element carrier coordinate system, r_e is the distance from the element rotation center P to element C.G.

$$\begin{aligned} \underline{\dot{\boldsymbol{L}}_e} &= -\boldsymbol{r_c}\frac{\boldsymbol{d}}{\boldsymbol{dt}}\underline{\hat{\boldsymbol{c}}_1} + \boldsymbol{r_e}\frac{\boldsymbol{d}}{\boldsymbol{dt}}\underline{\hat{\boldsymbol{e}}_2} \\ &= -\boldsymbol{r_c}\underline{\omega_c}\times\underline{\hat{\boldsymbol{c}}_1} + \boldsymbol{r_e}\underline{\omega_e}\times\underline{\hat{\boldsymbol{e}}_2} \\ &= -\boldsymbol{r_c}\omega_c\underline{\hat{\boldsymbol{c}}_2} - \boldsymbol{r_e}\omega_e\underline{\hat{\boldsymbol{e}}_1} \\ &= -\boldsymbol{r_c}\omega_c\underline{\hat{\boldsymbol{c}}_2} - \boldsymbol{r_e}\omega_e(\cos\alpha\underline{\hat{\boldsymbol{c}}_1} + \sin\alpha\underline{\hat{\boldsymbol{c}}_2}) \\ &= -\boldsymbol{r_c}\omega_c\underline{\hat{\boldsymbol{c}}_2} - \boldsymbol{r_e}\omega_e\{\cos[(\alpha_0 - 90^\circ) + (\theta_e - \theta_c)]\underline{\hat{\boldsymbol{c}}_1} + \sin[(\alpha_0 - 90^\circ) + (\theta_e - \theta_c)]\underline{\hat{\boldsymbol{c}}_2}\} \\ &= -\boldsymbol{r_c}\omega_c\underline{\hat{\boldsymbol{c}}_2} - \boldsymbol{r_e}\omega_e\{\cos[(\theta_e - \theta_c + \alpha_0) - 90^\circ]\underline{\hat{\boldsymbol{c}}_1} + \sin[(\theta_e - \theta_c + \alpha_0) - 90^\circ]\underline{\hat{\boldsymbol{c}}_2}\} \\ &= -\boldsymbol{r_c}\omega_c\underline{\hat{\boldsymbol{c}}_2} - \boldsymbol{r_e}\omega_e[\sin(\theta_e - \theta_c + \alpha_0)\underline{\hat{\boldsymbol{c}}_1} - \cos(\theta_e - \theta_c + \alpha_0)\underline{\hat{\boldsymbol{c}}_2}] \\ &= -\boldsymbol{r_e}\omega_e\sin(\theta_e - \theta_c + \alpha_0)\underline{\hat{\boldsymbol{c}}_1} - [\boldsymbol{r_c}\omega_c - \boldsymbol{r_e}\omega_e\cos(\theta_e - \theta_c + \alpha_0)]\underline{\hat{\boldsymbol{c}}_2} \end{aligned} \tag{2.7}$$

where α is the orientation of unit vector $\underline{\hat{e}_1}$ with respect to line *P*-*O* connecting the

element carrier rotation center P and the element rotation center O. The orientation of the element is determined by angle α_0, which is formed by the line P-O and line $C.G.$-O connecting the element center of gravity $C.G.$ and the element rotation center O.

$$\begin{aligned}\frac{1}{2}\boldsymbol{m}_e\underline{\dot{\boldsymbol{L}}_e}\cdot\underline{\dot{\boldsymbol{L}}_e} &= \frac{1}{2}\boldsymbol{m}_e[\boldsymbol{r}_c^{\,2}\omega_c^{\,2}+\boldsymbol{r}_e^{\,2}\omega_e^{\,2}-2\boldsymbol{r}_c\boldsymbol{r}_e\omega_c\omega_e\cos(\theta_e-\theta_c+\alpha_0)] \\ &= \frac{1}{2}\boldsymbol{m}_e[\boldsymbol{r}_c^{\,2}\dot{\theta}_c^{\,2}+\boldsymbol{r}_e^{\,2}\dot{\theta}_e^{\,2}-2\boldsymbol{r}_c\boldsymbol{r}_e\dot{\theta}_c\dot{\theta}_e\cos(\theta_e-\theta_c+\alpha_0)]\end{aligned} \tag{2.8}$$

$$\boldsymbol{T}=\frac{1}{2}\boldsymbol{m}_e[\boldsymbol{r}_c^{\,2}\dot{\theta}_c^{\,2}+\boldsymbol{r}_e^{\,2}\dot{\theta}_e^{\,2}-2\boldsymbol{r}_c\boldsymbol{r}_e\dot{\theta}_c\dot{\theta}_e\cos(\theta_e-\theta_c+\alpha_0)]+\frac{1}{2}\boldsymbol{I}_e\dot{\theta}_e^{\,2}+\frac{1}{2}\boldsymbol{I}_c\dot{\theta}_c^{\,2} \tag{2.9}$$

The potential energy of the element comes from the rotational deflection of element suspension spring.

$$\boldsymbol{k}(\theta_e,\theta_c)=\boldsymbol{k}(\theta_e-\theta_c) \tag{2.10}$$

is torsional spring constant of the element suspension spring, which is function of θ_e-θ_c, relative rotation angle of the element with respect to the element carrier. As a result, the potential energy V is expressed as

$$\boldsymbol{V}=\boldsymbol{V}(\boldsymbol{k},\theta_e-\theta_c) \tag{2.11}$$

For the micro time delay mechanism, the Rayleigh's dissipation function comes from air damping between the element and the element carrier below,

$$\boldsymbol{D}=\frac{1}{2}\boldsymbol{c}_{air\_damping}(\dot{\theta}_e-\dot{\theta}_c)^2 \tag{2.12}$$

where $c_{air\_camping}$ is damping coefficient that considering air damping effect.

Considering element rotation angle θ_e,

$$\frac{\boldsymbol{d}}{\boldsymbol{dt}}\left(\frac{\partial \boldsymbol{T}}{\partial \dot{\theta}_e}\right)-\frac{\partial \boldsymbol{T}}{\partial \theta_e}+\frac{\partial \boldsymbol{D}}{\partial \dot{\theta}_e}+\frac{\partial \boldsymbol{V}}{\partial \theta_e}=\boldsymbol{Q}_e \tag{2.13}$$

$$\begin{aligned}&\frac{\boldsymbol{d}}{\boldsymbol{dt}}[\boldsymbol{m}_e\boldsymbol{r}_e^{\,2}\dot{\theta}_e-\boldsymbol{m}_e\boldsymbol{r}_c\boldsymbol{r}_e\dot{\theta}_c\cos(\theta_e-\theta_c+\alpha_0)+\boldsymbol{I}_e\dot{\theta}_e]-\boldsymbol{m}_e\boldsymbol{r}_c\boldsymbol{r}_e\dot{\theta}_c\dot{\theta}_e\sin(\theta_e-\theta_c+\alpha_0)\\&+\boldsymbol{c}_{air\_damping}(\dot{\theta}_e-\dot{\theta}_c)+\frac{\partial \boldsymbol{V}(\boldsymbol{k},\theta_e-\theta_c)}{\partial \theta_e}=-\boldsymbol{Q}_{friction}\end{aligned} \tag{2.14}$$

where, $Q_{friction}$ is the friction torque applied on element by the adjacent element.

$$\begin{aligned}&\ddot{\theta}_e(\boldsymbol{m}_e\boldsymbol{r}_e^{\,2}+\boldsymbol{I}_e)-\ddot{\theta}_c\boldsymbol{m}_e\boldsymbol{r}_c\boldsymbol{r}_e\cos(\theta_e-\theta_c+\alpha_0)+\boldsymbol{m}_e\boldsymbol{r}_c\boldsymbol{r}_e\dot{\theta}_c\sin(\theta_e-\theta_c+\alpha_0)(\dot{\theta}_e-\dot{\theta}_c)\\&-\boldsymbol{m}_e\boldsymbol{r}_c\boldsymbol{r}_e\dot{\theta}_c\dot{\theta}_e\sin(\theta_e-\theta_c+\alpha_0)+\boldsymbol{c}_{air\_damping}(\dot{\theta}_e-\dot{\theta}_c)+\frac{\partial \boldsymbol{V}(\boldsymbol{k},\theta_e-\theta_c)}{\partial \theta_e}=-\boldsymbol{Q}_{friction}\end{aligned} \tag{2.15}$$

$$\begin{aligned}&\ddot{\theta}_e(\boldsymbol{m}_e\boldsymbol{r}_e^{\,2}+\boldsymbol{I}_e)-\ddot{\theta}_c\boldsymbol{m}_e\boldsymbol{r}_c\boldsymbol{r}_e\cos(\theta_e-\theta_c+\alpha_0)-\dot{\theta}_c^{\,2}\boldsymbol{m}_e\boldsymbol{r}_c\boldsymbol{r}_e\sin(\theta_e-\theta_c+\alpha_0)\\&+\boldsymbol{c}_{air\_damping}(\dot{\theta}_e-\dot{\theta}_c)+\frac{\partial \boldsymbol{V}(\boldsymbol{k},\theta_e-\theta_c)}{\partial \theta_e}=-\boldsymbol{Q}_{friction}\end{aligned} \tag{2.16}$$

$$\theta_e-\theta_c=\theta \tag{2.17}$$

$$\begin{aligned}&\ddot{\theta}_e(\boldsymbol{m}_e\boldsymbol{r}_e^{\,2}+\boldsymbol{I}_e)-\ddot{\theta}_c\boldsymbol{m}_e\boldsymbol{r}_c\boldsymbol{r}_e\cos(\theta+\alpha_0)-\dot{\theta}_c^{\,2}\boldsymbol{m}_e\boldsymbol{r}_c\boldsymbol{r}_e\sin(\theta+\alpha_0)\\&+\boldsymbol{c}_{air\_damping}\dot{\theta}+\frac{\partial \boldsymbol{V}(\boldsymbol{k},\theta)}{\partial \theta_e}=-\boldsymbol{Q}_{friction}\end{aligned} \tag{2.18}$$

Because time duration of element vibration cycle is in the order of millisecond, the element carrier rotational speed is assumed constant.

$$\dot{\theta}_c = \omega_c = constant$$
$$\ddot{\theta}_c = 0 \tag{2.19}$$

$$\ddot{\theta}_e(\boldsymbol{m}_e\boldsymbol{r}_e^2 + \boldsymbol{I}_e) - \omega_c^2 \boldsymbol{m}_e\boldsymbol{r}_c\boldsymbol{r}_e \sin(\theta + \alpha_0) + \boldsymbol{c}_{air\_damping}\dot{\theta} + \frac{\partial \boldsymbol{V}(\boldsymbol{k},\theta)}{\partial \theta_e} = -\boldsymbol{Q}_{friction} \tag{2.20}$$

$$\ddot{\theta}(\boldsymbol{m}_e\boldsymbol{r}_e^2 + \boldsymbol{I}_e) - \omega_c^2 \boldsymbol{m}_e\boldsymbol{r}_c\boldsymbol{r}_e(\sin\theta\cos\alpha_0 + \cos\theta\sin\alpha_0) + \boldsymbol{c}_{air\_damping}\dot{\theta} + \frac{\partial \boldsymbol{V}(\boldsymbol{k},\theta)}{\partial \theta_e} = -\boldsymbol{Q}_{friction} \tag{2.21}$$

Assuming the element rotation angle θ is small,

$$\begin{cases} \sin\theta \approx \theta \\ \cos\theta \approx 1 \end{cases} \tag{2.22}$$

$$\ddot{\theta}(\boldsymbol{m}_e\boldsymbol{r}_e^2 + \boldsymbol{I}_e) - \omega_c^2 \boldsymbol{m}_e\boldsymbol{r}_c\boldsymbol{r}_e(\theta\cos\alpha_0 + \sin\alpha_0) + \boldsymbol{c}_{air\_damping}\dot{\theta} + \frac{\partial \boldsymbol{V}(\boldsymbol{k},\theta)}{\partial \theta_e} = -\boldsymbol{Q}_{friction} \tag{2.23}$$

With initial condition,

$$\theta(0) = \dot{\theta}(0) = 0 \tag{2.24}$$

the torque from friction, $Q_{friction}$ is considered by using constant dynamic friction coefficient and constant static friction coefficient.

For linear spring,

$$\boldsymbol{k}(\theta_e, \theta_c) = \boldsymbol{k}(\theta) = \boldsymbol{k}_{const} \tag{2.25}$$

the potential energy $V(k,\theta)$ is

$$\boldsymbol{V}(\boldsymbol{k},\theta) = \frac{1}{2}\boldsymbol{k}_{const}\theta^2 \tag{2.26}$$

When omitting the effect of air damping, the dynamic equation becomes

$$\ddot{\theta}(\boldsymbol{m}_e\boldsymbol{r}_e^2 + \boldsymbol{I}_e) - \omega_c^2 \boldsymbol{m}_e\boldsymbol{r}_c\boldsymbol{r}_e(\theta\cos\alpha_0 + \sin\alpha_0) + \boldsymbol{k}_{const}\theta = -\boldsymbol{Q}_{friction} \tag{2.27}$$

$$(\boldsymbol{m}_e\boldsymbol{r}_e^2 + \boldsymbol{I}_e)\ddot{\theta} + (\boldsymbol{k}_{const} - \omega_c^2 \boldsymbol{m}_e\boldsymbol{r}_c\boldsymbol{r}_e\cos\alpha_0)\theta = \omega_c^2 \boldsymbol{m}_e\boldsymbol{r}_c\boldsymbol{r}_e\sin\alpha_0 - \boldsymbol{Q}_{friction} \tag{2.28}$$

The element vibration solution is,

$$\theta = \boldsymbol{c}_1 \cos(\omega_n \boldsymbol{t}) + \boldsymbol{c}_2 \sin(\omega_n \boldsymbol{t}) + \frac{\omega_c{}^2 \boldsymbol{m}_e \boldsymbol{r}_c \boldsymbol{r}_e \sin\alpha_0 - \boldsymbol{Q}_{friction}}{-\omega_c{}^2 \boldsymbol{m}_e \boldsymbol{r}_c \boldsymbol{r}_e \cos\alpha_0 + \boldsymbol{k}_{const}} \tag{2.29}$$

where, constant c_1 and c_2 are

$$\boldsymbol{c}_1 = \frac{-\omega_c{}^2 \boldsymbol{m}_e \boldsymbol{r}_c \boldsymbol{r}_e \sin\alpha_0 + \boldsymbol{Q}_{friction}}{-\omega_c{}^2 \boldsymbol{m}_e \boldsymbol{r}_c \boldsymbol{r}_e \cos\alpha_0 + \boldsymbol{k}_{const}} \tag{2.30}$$

$$\boldsymbol{c}_2 = 0 \tag{2.31}$$

Angular natural resonant frequency ω_n is

$$\omega_n = \sqrt{\frac{\omega_c{}^2 \boldsymbol{m}_e \boldsymbol{r}_c \boldsymbol{r}_e (-\cos\alpha_0) + \boldsymbol{k}_{const}}{\boldsymbol{m}_e \boldsymbol{r}_e{}^2 + \boldsymbol{I}_e}} \qquad (-\cos\alpha_0) > 0 \tag{2.32}$$

$$\theta = \frac{\omega_c{}^2 \boldsymbol{m}_e \boldsymbol{r}_c \boldsymbol{r}_e \sin\alpha_0 - \boldsymbol{Q}_{friction}}{-\omega_c{}^2 \boldsymbol{m}_e \boldsymbol{r}_c \boldsymbol{r}_e \cos\alpha_0 + \boldsymbol{k}_{const}} [1 - \cos(\omega_n \boldsymbol{t})] \tag{2.33}$$

For a single element, during the vibration procedure, it oscillates about static-equilibrium position θ_{sta_eqi} [31]. From dynamics equation

$$\begin{aligned} &\ddot{\theta}_e(\boldsymbol{m}_e \boldsymbol{r}_e{}^2 + \boldsymbol{I}_e) - \ddot{\theta}_c \boldsymbol{m}_e \boldsymbol{r}_c \boldsymbol{r}_e \cos(\theta_e - \theta_c + \alpha_0) - \dot{\theta}_c{}^2 \boldsymbol{m}_e \boldsymbol{r}_c \boldsymbol{r}_e \sin(\theta_e - \theta_c + \alpha_0) + \boldsymbol{k}(\theta_e - \theta_c) \\ &= -\boldsymbol{Q}_{friction} \end{aligned} \tag{2.34}$$

Let,

$$\begin{cases} \dot{\theta}_e = 0 \\ \\ \ddot{\theta}_e = 0 \end{cases} \qquad \textbf{\textit{and}} \qquad \ddot{\theta}_c = 0 \tag{2.35}$$

$$-\dot{\theta}_c{}^2 \boldsymbol{m}_e \boldsymbol{r}_c \boldsymbol{r}_e \sin(\theta_e - \theta_c + \alpha_0) + \boldsymbol{k}(\theta_e - \theta_c) = -\boldsymbol{Q}_{friction} \tag{2.36}$$

$$\theta_e - \theta_c = \theta \tag{2.37}$$

$$-\dot{\theta}_c{}^2 \boldsymbol{m}_e \boldsymbol{r}_c \boldsymbol{r}_e \sin(\theta + \alpha_0) + \boldsymbol{k}\theta = -\boldsymbol{Q}_{friction} \tag{2.38}$$

$$\boldsymbol{k}\theta - \dot{\theta}_c^{\,2}\boldsymbol{m}_e\boldsymbol{r}_c\boldsymbol{r}_e(\sin\theta\cos\alpha_0 + \cos\theta\sin\alpha_0) = -\boldsymbol{Q}_{friction} \tag{2.39}$$

$$\boldsymbol{k}\theta - \dot{\theta}_c^{\,2}\boldsymbol{m}_e\boldsymbol{r}_c\boldsymbol{r}_e\sin\theta\cos\alpha_0 - \dot{\theta}_c^{\,2}\boldsymbol{m}_e\boldsymbol{r}_c\boldsymbol{r}_e\cos\theta\sin\alpha_0 = -\boldsymbol{Q}_{friction} \tag{2.40}$$

Assuming the element rotation angle θ is small,

$$\begin{cases}\sin\theta \approx \theta \\ \cos\theta \approx 1\end{cases} \tag{2.41}$$

$$\boldsymbol{k}\theta_{sta\_eqi} - \dot{\theta}_c^{\,2}\boldsymbol{m}_e\boldsymbol{r}_c\boldsymbol{r}_e\cos\alpha_0\theta_{sta\_eqi} - \dot{\theta}_c^{\,2}\boldsymbol{m}_e\boldsymbol{r}_c\boldsymbol{r}_e\sin\alpha_0 = -\boldsymbol{Q}_{friction} \tag{2.42}$$

$$(\boldsymbol{k} - \dot{\theta}_c^{\,2}\boldsymbol{m}_e\boldsymbol{r}_c\boldsymbol{r}_e\cos\alpha_0)\theta_{sta\_eqi} = \dot{\theta}_c^{\,2}\boldsymbol{m}_e\boldsymbol{r}_c\boldsymbol{r}_e\sin\alpha_0 - \boldsymbol{Q}_{friction} \tag{2.43}$$

$$\theta_{sta\_eqi} = \frac{\dot{\theta}_c^{\,2}\boldsymbol{m}_e\boldsymbol{r}_c\boldsymbol{r}_e\sin\alpha_0 - \boldsymbol{Q}_{friction}}{\boldsymbol{k} - \dot{\theta}_c^{\,2}\boldsymbol{m}_e\boldsymbol{r}_c\boldsymbol{r}_e\cos\alpha_0} \tag{2.44}$$

$$\theta_{sta\_eqi} = \frac{\omega_c^{\,2}\boldsymbol{m}_e\boldsymbol{r}_c\boldsymbol{r}_e\sin\alpha_0 - \boldsymbol{Q}_{friction}}{-\omega_c^{\,2}\boldsymbol{m}_e\boldsymbol{r}_c\boldsymbol{r}_e\cos\alpha_0 + \boldsymbol{k}} \tag{2.45}$$

Equation (2.45) verifies results in equation (2.33).

2.2.1.1 Time Delay Derivation

From equation (2.33), time for element to rotate through a given critical angle γ is found by setting $\theta = \gamma$ and solving for t:

$$\boldsymbol{t}_{delay} = \frac{1}{\omega_n}\cos^{-1}\left[1 + \frac{(-\omega_c^{\,2}\boldsymbol{m}_e\boldsymbol{r}_c\boldsymbol{r}_e\cos\alpha_0 + \boldsymbol{k}_{const})\gamma}{-\omega_c^{\,2}\boldsymbol{m}_e\boldsymbol{r}_c\boldsymbol{r}_e\sin\alpha_0 + \boldsymbol{Q}_{friction}}\right] \tag{2.46}$$

where, the linear spring constant k_{const} can be determined by taking the average value of $k(\theta)$, i.e.

$$\boldsymbol{k}_{const} = \frac{1}{\gamma}\int_0^{\gamma}\boldsymbol{k}(\theta)\boldsymbol{d}\theta \tag{2.47}$$

2.2.1.2 Switching Speed Analysis

During the operation of the micro time delay mechanism, the switching sequence starts when the first mechanism element passes its critical angle. The switching speed of the time delay mechanism is the mechanism rotation speed at which the first mechanism element passes its critical angle.

For element #1, the equation is setup by considering torque balance of element #1.

$$\boldsymbol{m}_e\dot{\theta}_c^{\,2}\boldsymbol{L}_{e1}\boldsymbol{d}_{1a} - \boldsymbol{f}_{21}\boldsymbol{R}_e - \boldsymbol{k}(\theta)\theta_1 = \boldsymbol{I}_{center}\ddot{\theta}_1 \tag{2.48}$$

where $m_e\dot{\theta}_c^{\,2}L_{e1}$ is the centrifugal force on element #1 coming from element carrier rotation, L_{e1} is distance from *C.G.* of the element #1 to the element carrier rotation center.

In the above equation,

$$\boldsymbol{d}_{1a} = \boldsymbol{r}_e\cos\beta \tag{2.49}$$

is the distance from the element #1 rotation center to line connecting *C.G.* of the element #1 to the *C.G.* of the element carrier. And β is the angle between line connecting the element #1 rotation center to element #1 center of gravity and the shortest line from element #1 rotation center to line from the element #1 rotation center to the element carrier rotation center.

$$\boldsymbol{f}_{21} = \mu_{dyn}\boldsymbol{F}_{21} \tag{2.50}$$

is the friction force applied on the element #1 by the element #2. It is the product of the dynamic coefficient of friction μ_{dyn} and normal force F_{12} applied by the element #2 on the element #1. The term $k(\theta)\theta_1$ represents the restoring torque produced by the torsional suspension spring of the element #1 with rotation angle θ_1. I_{center} is moment inertia of element #1 with respect to its center of rotation.

$$\boldsymbol{I}_{center} = \boldsymbol{I}_{e} + \boldsymbol{m}_{e}\boldsymbol{r}_{e}^{2} \tag{2.51}$$

From torque balance equation of the element #2,

$$\boldsymbol{m}_{e}\dot{\theta}_{c}^{2}\boldsymbol{L}_{e2}\boldsymbol{d}_{2a} - \boldsymbol{f}_{32}\boldsymbol{R}_{e} - \boldsymbol{f}_{12}\boldsymbol{d}_{2b} - \boldsymbol{F}_{12}\boldsymbol{d}_{2c} = 0 \tag{2.52}$$

In the above torque balance equation, $m_e\dot{\theta}_c^{\,2}L_{e2}d_{2a}$ is torque on the element #2 generated through element carrier rotation. $f_{32}R_e$ is torque from friction between the element #2 and the element #3. $f_{12}d_{2b}$ is torque due to friction between the element #1 and the element #2, where d_{2b} is the distance from the element #2 center of rotation to line in the direction normal to contact surface of the element #1 and the element #2 and passing through the surface contact point. $F_{21}d_{2c}$ is torque comes from the normal contact force between the element #1 and the element #2, where d_{2c} is distance from the element #2 center of rotation to line in the direction normal to contact surface of the element #1 and the element #2 and passing their contact point.

$$\boldsymbol{f}_{32} = \mu_{sta}\boldsymbol{F}_{32} \tag{2.53}$$

where, f_{32} is the friction force on the element #2 applied by the element #3. It is the product of the static coefficient of friction μ_{sta} and normal force F_{32} applied by the element #3 on the element #2.

The following equation comes from torque balance on the element #3.

$$\boldsymbol{m}_{e}\dot{\theta}_{c}^{2}\boldsymbol{L}_{e3}\boldsymbol{d}_{3a} - \boldsymbol{f}_{23}\boldsymbol{d}_{3b} - \boldsymbol{F}_{23}\boldsymbol{d}_{3c} = 0 \tag{2.54}$$

where, $m_e\dot{\theta}_c^{\,2}L_{e3}d_{3a}$ is torque on the element #3 due to the element carrier rotation. $f_{23}d_{3b}$ is torque due to friction between the element #2 and the element #3. $F_{23}d_{3c}$ is torque comes from the normal contact force between the element #2 and the element #3.

The element delay time was calculated based on the above equations.

$$\begin{cases} \boldsymbol{m}_e \dot{\theta}_c^{\,2} \boldsymbol{L}_{e1} \boldsymbol{d}_{1a} - \boldsymbol{f}_{21} \boldsymbol{R}_e - \boldsymbol{k}(\theta_1)\theta_1 = \boldsymbol{I}_{center} \ddot{\theta}_1 \\ \boldsymbol{m}_e \dot{\theta}_c^{\,2} \boldsymbol{L}_{e2} \boldsymbol{d}_{2a} - \boldsymbol{f}_{32} \boldsymbol{R}_e - \boldsymbol{f}_{12} \boldsymbol{d}_{2b} - \boldsymbol{F}_{12} \boldsymbol{d}_{2c} = 0 \\ \boldsymbol{m}_e \dot{\theta}_c^{\,2} \boldsymbol{L}_{e3} \boldsymbol{d}_{3a} - \boldsymbol{f}_{23} \boldsymbol{d}_{3b} - \boldsymbol{F}_{23} \boldsymbol{d}_{3c} = 0 \\ \boldsymbol{I}_{center} = \boldsymbol{I}_e + \boldsymbol{m}_e \boldsymbol{r}_e^{\,2} \\ \boldsymbol{d}_{1a} = \boldsymbol{r}_e \cos\beta \\ \boldsymbol{d}_{2a} = \boldsymbol{d}_{3a} = \boldsymbol{const} \\ \boldsymbol{f}_{12} = \boldsymbol{f}_{21} \\ \boldsymbol{f}_{23} = \boldsymbol{f}_{32} \end{cases} \tag{2.55}$$

The solution of the above equations is:

$$(\boldsymbol{I}_e + \boldsymbol{m}_e \boldsymbol{r}_e^{\,2})\ddot{\theta}_1 + \boldsymbol{k}(\theta_1)\theta_1 - \boldsymbol{m}_e \dot{\theta}_c^{\,2}[\boldsymbol{L}_{e1}\boldsymbol{d}_{1a} - \frac{\boldsymbol{R}_e}{\mu_{dyn}\boldsymbol{d}_{2b} + \boldsymbol{d}_{2c}}(\boldsymbol{L}_{e2}\boldsymbol{d}_{2a} - \frac{\boldsymbol{L}_{e3}\boldsymbol{d}_{3a}\boldsymbol{R}_e}{\boldsymbol{d}_{3b} - \mu_{sta}\boldsymbol{d}_{3c}})] = 0 \tag{2.56}$$

Because the element carrier is accelerated linearly, the angular velocity $\dot{\theta}_c$ is,

$$\dot{\theta}_c = \psi \boldsymbol{t} \tag{2.57}$$

where, angular acceleration ψ is constant. The above ODE is expressed as:

$$(\boldsymbol{I}_e + \boldsymbol{m}_e \boldsymbol{r}_e^{\,2})\ddot{\theta}_1 + \boldsymbol{k}(\theta_1)\theta_1 - \boldsymbol{m}_e \psi^2[\boldsymbol{L}_{e1}\boldsymbol{d}_{1a} - \frac{\boldsymbol{R}_e}{\mu_{dyn}\boldsymbol{d}_{2b} + \boldsymbol{d}_{2c}}(\boldsymbol{L}_{e2}\boldsymbol{d}_{2a} - \frac{\boldsymbol{L}_{e3}\boldsymbol{d}_{3a}\boldsymbol{R}_e}{\boldsymbol{d}_{3b} - \mu_{sta}\boldsymbol{d}_{3c}})]\boldsymbol{t}^2 = 0 \tag{2.58}$$

When employing linearized spring constant as in equation (2.45), the spring constant $k(\theta_1)$ becomes constant value. The above ODE equation can be solved theoretically with initial conditions,

$$\begin{cases} \theta_1(0) = 0 \\ \dot{\theta}_1(0) = 0 \end{cases} \tag{2.59}$$

The solution is:

$$\theta_1 = \frac{c_2}{c_1^2}(2 - c_1 t^2 - 2\cos(\sqrt{c_1 t})) \tag{2.60}$$

Where,

$$C_1 = \frac{k(\theta_1)}{I_e + m_e r_e^2}$$
$$C_2 = \frac{m_e \psi^2 [-L_{e1} d_{1a} + \frac{R_e}{\mu_{dyn} d_{2b} + d_{2c}} (L_{e2} d_{2a} - \frac{L_{e3} d_{3a} R_e}{d_{3b} - \mu_{sta} d_{3c}})]}{I_e + m_e r_e^2} \tag{2.61}$$

2.2.1.3 Air Damping

During and after the switching event, the mechanism element vibrated parallel with the element carrier at low frequency. Couette flow was used to describe the airflow under the moving element [35]. The damping coefficient C_{air} of this torsional air damper was derived according to the shape of the element [36]. The shear stress τ is proportional to the viscosity of air μ and velocity gradient $\frac{du}{dy}$ perpendicular to the direction of the airflow.

$$\tau = \mu \frac{du}{dy} \tag{2.62}$$

Couette flow was used to describe the airflow under the moving element, the velocities of intermediate fluid layers vary linearly between 0 and v.

$$\frac{du}{dy} = \frac{v}{h} \tag{2.63}$$

where, h is the gap between mechanism element and device substrate.

The shear torque dT acting on area dA is:

$$\begin{aligned} \boldsymbol{dT} &= \tau \boldsymbol{dA} \cdot r \\ &= \mu \frac{du}{dy} \boldsymbol{dA} \cdot \boldsymbol{r} \\ &= \mu \frac{\boldsymbol{v}}{\boldsymbol{h}} \boldsymbol{dA} \cdot \boldsymbol{r} \\ &= \mu \frac{\boldsymbol{r}\dot{\theta}}{\boldsymbol{h}} \boldsymbol{dA} \cdot \boldsymbol{r} \\ &= \mu \frac{\boldsymbol{r}\dot{\theta}}{\boldsymbol{h}} (\boldsymbol{r d\theta dr}) \cdot \boldsymbol{r} \\ &= \frac{\mu\dot{\theta}}{\boldsymbol{h}} \boldsymbol{r}^3 \boldsymbol{dr d\theta} \end{aligned} \tag{2.64}$$

where, r is the distance from element rotation center to area dA, θ, $\dot{\theta}$ are the rotation angle and angular velocity of the element.

Torque acting on the entire element is obtained by integrating the shear torque dT across the whole element area.

$$\begin{aligned} \boldsymbol{T} &= \iint_{\boldsymbol{S}} \boldsymbol{dT} = \iint_{\boldsymbol{S}} \frac{\mu\dot{\theta}}{\boldsymbol{h}} \boldsymbol{r}^3 \boldsymbol{dr d\theta} \\ &= \frac{\mu\dot{\theta}}{\boldsymbol{h}} \int_0^{\frac{3}{4}\pi} \boldsymbol{d\theta} \int_{\boldsymbol{R}_1}^{\boldsymbol{R}_2} \boldsymbol{r}^3 \boldsymbol{dr} \\ &= \frac{3\pi}{16} \frac{\mu(\boldsymbol{R}_2{}^4 - \boldsymbol{R}_1{}^4)}{\boldsymbol{h}} \dot{\theta} \end{aligned} \tag{2.65}$$

In the above equation, R_2 is the outer radius of the leaf element, and R_1 is an effective inner radius used to account for the notch removed from the leaf to provide connection to the spring.

Thus damping coefficient C_{air} is obtained.

$$\boldsymbol{C}_{\boldsymbol{air}} = \frac{3\pi}{16} \frac{\mu(\boldsymbol{R}_2{}^4 - \boldsymbol{R}_1{}^4)}{\boldsymbol{h}} \tag{2.66}$$

2.2.2 Device Design

To design the micro time delay mechanism, theoretical as well as numerical designs approaches were adopted. Based on the theories developed in Chapter 2, both the switching speed and the element delay time were calculated. The calculations either used simplified theoretical results or use numerical method to solve the non-linear ODE from the theoretical analyses. Besides, numerical analyses using dynamic simulation software ADAMS were conducted to obtain the vibration dynamics of the micro time delay mechanism composed of multiple elements. Results from theoretical analyses, from numerically solved theoretical ODE equations, and from ADAMS numerical analyses were compared. Finite Element Analysis (FEA) tool ANSYS was also used to obtain the torsional spring constant of the non-linear element suspension springs.

2.2.2.1 Device Element Design

2.2.2.1.1 Spring Design

Both the escapement and sequential leaf mechanism designs require a torsional spring element for proper operation. As seen in Figure 7, the spring suspends the inertial element of the micro time delay mechanism above the silicon substrate and provides a restoring torque against the actuation torque resulting from centrifugal acceleration. When designing the suspension spring, not only the torsional spring constant needs to be considered, the influence of transverse force to the torsional spring constant also needs to be accounted. The ability of the suspension spring to defend the transverse force during

element rotation determines the influence of spring deformation to element contact. The spring deformation should be as low as possible.

Three spring configurations have been simulated. They are straight beam suspension spring, straight beam suspension spring with relief structures, and curved beam suspension spring (Figure 12). The non-linear suspension spring constants were calculated through 2D and 3D Finite Element Analysis (FEA) simulation in ANSYS, [32], [33]. The 3D FEA structural analyses were conducted first by using 3D element, solid 95. Suspension spring structures with different thickness were simulated to find the relation between spring constant and device thickness. It was found that the torsional spring constant varies linearly with device thinness variation. As a result, 2D FEA element, plane 82, was used in the following FEA simulation to save calculation time. Large element deformation was included in the simulations to explore the non-linear spring deformation.

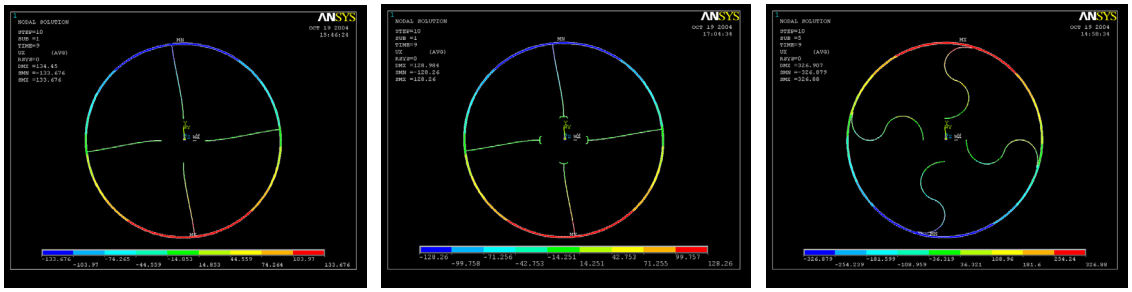

(a) (b) (c)

Figure 12 (a) Straight beam, (b) straight beam with relief structure, and (c) curved beam suspension spring designs.

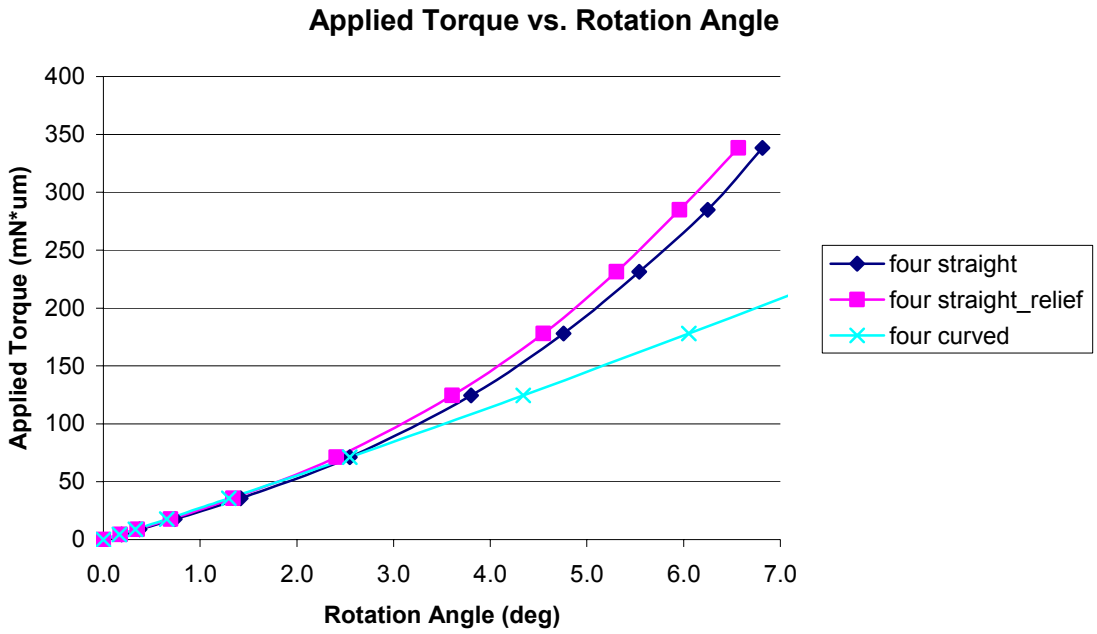

Figure 13 Non-linear suspension spring FEA results.

To determine the nonlinear behavior of the springs under the influence of a pure moment, torque was applied on the ring of the suspension spring by defining a force couple acting on opposite sides of the spring in the FEA simulations. Using ANSYS, torque was applied on the suspension spring, and the spring rotation angles under different applied torques were calculated. Results for the three different suspension spring designs are shown in Figure 13. In these designs, the inner and outer diameters of suspension ring, suspension beam anchor size, and width of the element suspension beams were the same. Radial distance from anchor to suspension ring was 853μm and beam width used was 5μm respectively. Maximum rotation angle of around 7^{o} have been obtained under torsional torque applied on the suspension ring.

The influence of transverse forces resulting from the centrifugal acceleration was

considered by applying a point force equal to 4.5 times that required to produce the maximum torque used in the spring modeling. This is because that in the experiment design the centrifugal force in the tangential direction of suspension ring is more than twice as that in the radial direction of the suspension ring. From simulation results, the influence of transverse force resulting from centrifugal acceleration was negligible, with a variation of the maximum rotation angle of less than 6.6%, and maximum in-plane deflections was reduced form 3.2 μm to 2.7 μm.

The torque-deflection relationship of the straight beam non-linear suspension spring may be described by a three-order polynomial. The parameters used in calculation are shown in Table 1.

$$T_{spring} = 21820\theta + 1153.7\theta^2 + 394.97\theta^3$$

Table 1 Suspension spring parameters.

Parameter	Value
Beam Width	5 μm
Beam Height	20 μm
Beam Length	853 μm
Anchor Radius	250 μm
Young's Modulus	165 GPa

From the FEA simulation results, the relief structure does not contribute much to reduce the spring constant, yet increases the complexity in FEA modeling and increases difficulty in meshing process of FEA. The ability of curved beam suspension spring to prevent transverse force is not enough. The maximum in-plane deflection was increased form 0.4 μm to 67.4 μm under according 7^o rotational deflection. As seen from the following figure, the curved beam was extended. The constraint is that it only allows

rotation deflection in one direction because of the mechanical interference from the folded beam structure itself. As a result, the straight beam suspension structure is used in the analysis.

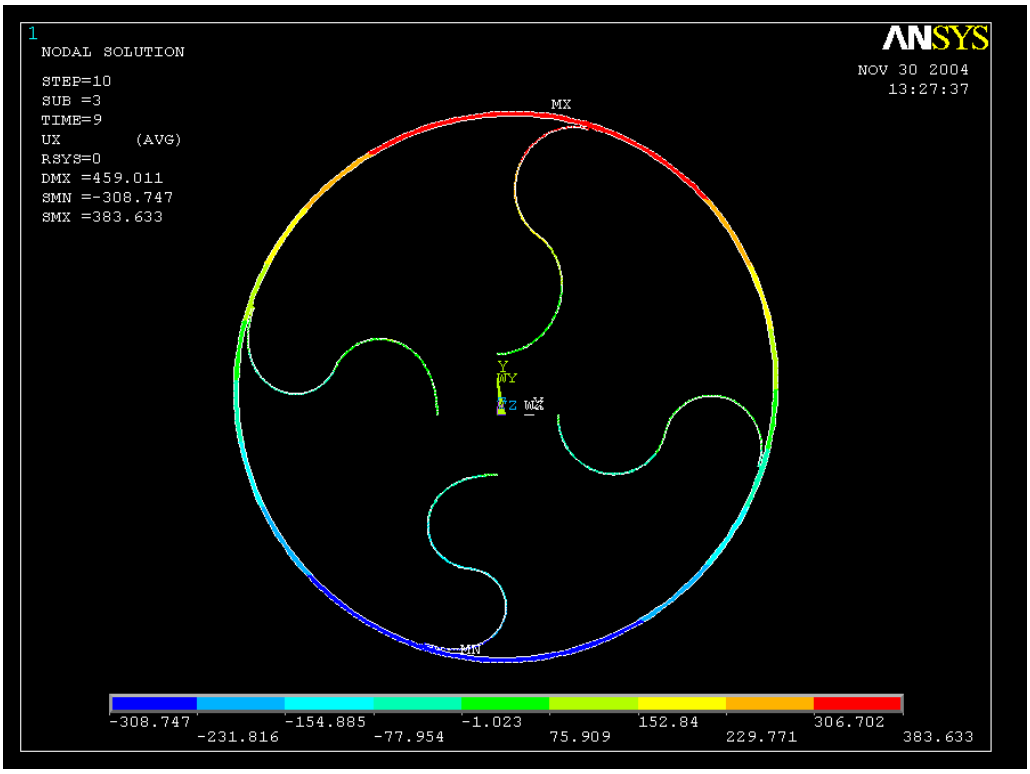

Figure 14 Transverse deflection of curved beam suspension spring.

2.2.2.1.2 Contact Friction

Element contact friction has been studied on macro-scale time delay mechanisms made from metallic materials [23], in which friction coefficient was described by an exponential function, $\mu = 0.275e^{-0.0023\omega}$, where ω is the element angular velocity with respect to its own rotation center. In the ADAMS simulation, a velocity-based friction model was used to simulate contact friction, with a dynamic friction coefficient (μ_d) used when relative velocity was higher than a friction-translation velocity (v_d) of 50 μm/s, and

a low-velocity friction coefficient varying between zero to a maximum static friction coefficient (μ_s) at a stiction-translation velocity (v_s) of 10 μm/s. While friction coefficients for bulk silicon have been previously studied [34], appropriate dynamic and static coefficients were selected here based on an initial comparison between ADAMS simulations and experimental results. In the ADAMS simulation, values ranging from 0.1 to 0.5 were tested as static and dynamic friction coefficients. Overall, switching speed and maximum vibration magnitude were found to increase with higher static and dynamic friction coefficients. As an example from a particular design, a 25% and 30% increase in static and dynamic friction coefficients, respectively, result in an increase in switching speed from 169 g to 260 g, and an increase in maximum vibration magnitude of approximate 0.2^o. Comparing the ADAMS results with initial experiment data, it was found that a static friction coefficient of 0.4 and dynamic friction coefficient of 0.3 provided a reasonable match between simulated and experimental results.

2.2.2.1.3 Air Damping

The damping coefficient equation from theoretical analysis was used to include the air damping effect,

$$\boldsymbol{C}_{air} = \frac{3\pi}{16}\frac{\mu(\boldsymbol{R}_2^{\,4} - \boldsymbol{R}_1^{\,4})}{\boldsymbol{h}}$$

Note that the leading 3π/16 factor results from the use of a leaf design, which consists of a partial disk covering an angular range of 3π/4 rad. Damping due to the spring beams and connection ring was assumed to be negligible compared to the leaf element. Using this expression, the damping coefficient is approximately 85 pN·m·s/rad.

2.2.2.2 System Modeling

2.2.2.2.1 Linear Analytic Model

Under the assumption of small element rotation angle, the non-linear ODE equation that governs the element vibration dynamics can be linearized by using linearized spring constant described in equation (2.44). Element delay time can be calculated by using equation (2.45), which provides an estimation of element delay time during the design stage.

2.2.2.2.2 Nonlinear Analytic Model

While the above equation provides a simple estimation for the switching time, it ignores significant nonlinearities inherent in the torsional spring and damping parameters. For a more accurate simulation, the full nonlinear equation of motion was solved numerically using MATLAB to determine device dynamics.

The equations (2.18) and (2.54) were solved numerically using ODE45 function in the MATLAB. The theoretical delay time is obtained by finding the time at element critical angle. And, the theoretical switching speed of the micro time delay mechanism is obtained by finding the rotation speed at element critical angle.

Figure 15 shows the typical relationship between time and the element rotation angle based on a specific design. The delay time at given critical angle can be obtained from this figure. Figure 16 shows the typical relationship between the switching speed and the element rotation angle based on a specific design. The element switching speed at

given critical angle can be obtained from this figure.

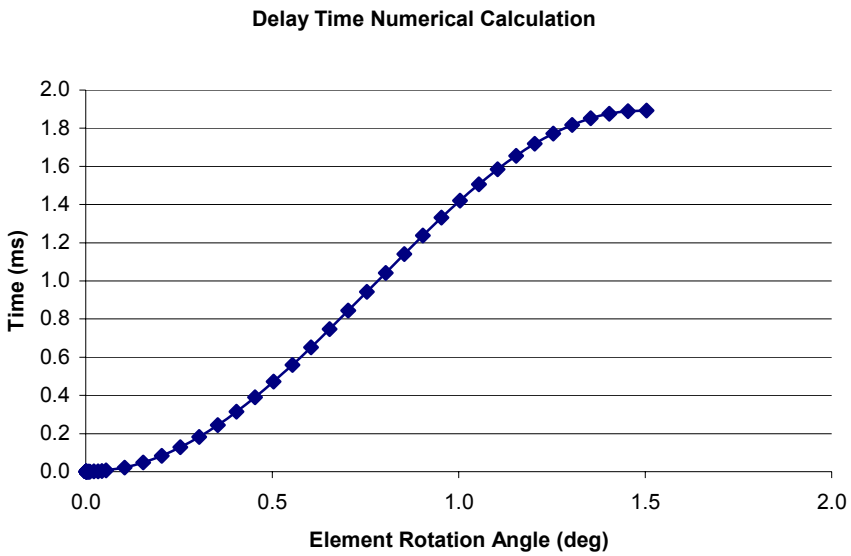

Figure 15 Numerical solution of non-linear analytic time delay ODE.

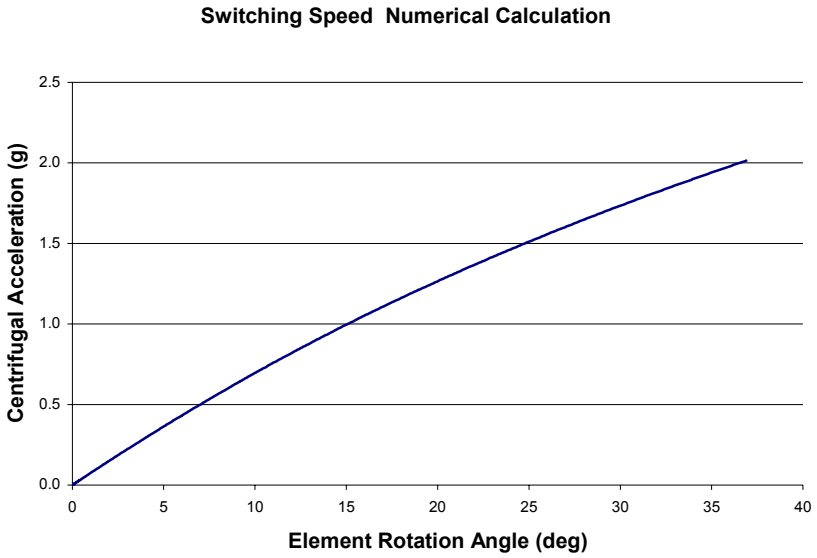

Figure 16 Numerical solution of non-linear analytic switching speed ODE.

2.2.2.2.3 Numerical Dynamics Simulation

Based on the MATLAB numerical simulation results, multiple-element numerical simulations were conducted in ADAMS. Impact and friction force between the micro time delay mechanism elements were considered in the simulations. In the ADAMS model, a device carrier with mass more than ten orders of magnitude bigger than the element mass was accelerated linearly to rotate from 0 rpm. The mechanism elements were arranged at locations approximately 28 mm away from the carrier rotation center. Each element was allowed to rotate around its own rotation center through a revolute joint. Torque was applied at the element rotation center to simulate the spring effect of the element suspension spring. The non-linear torque value was considered by introducing a spline curve for nonlinear spring constant. The element contacts including the element frictions were added between the adjacent elements.

From the ADAMS numerical simulation, the rotation angle of the element center of mass with respect to that of the element carrier was obtained from the ADAMS simulations. Figure 17 shows the typical numerical simulation results of a three-element micro time delay mechanism based on design #2. A linear angular velocity ramp of 54,000 deg/s^2 was applied to the device carrier to simulate the actual mechanism working environment. As shown in this figure, all three mechanism elements begin to oscillate with the same initial response. After the transient dynamics die down within the first 75 ms, the angular displacement of the second and third elements reach a steady-state value of approximately 0.3^o, and the first element increases linearly until the critical angle is reached at 160.4 ms. At this point, the first element is no longer in contact with the second element, which is itself unlocked and free to rotate. The second element reaches its critical angle 161.1 ms after the first element, unlocking the third element. Since the third element is the last element in the chain, it is not constrained by frictional contact once released, and exhibits somewhat different post-release response compared to the second element. The simulated switching time for the second element is most representative of the true unit delay time for a mechanism chain with an arbitrary number of elements, since it is constrained by friction after unlocking through contact with the third element. Thus the simulated delay time for this particular design was found to be 0.7 ms. In the simulations, the suspension of micro time delay mechanism elements were model by torsional springs. The variable spring constant came from Finite Element Analysis (FEA) with ANSYS by considering large deformation.

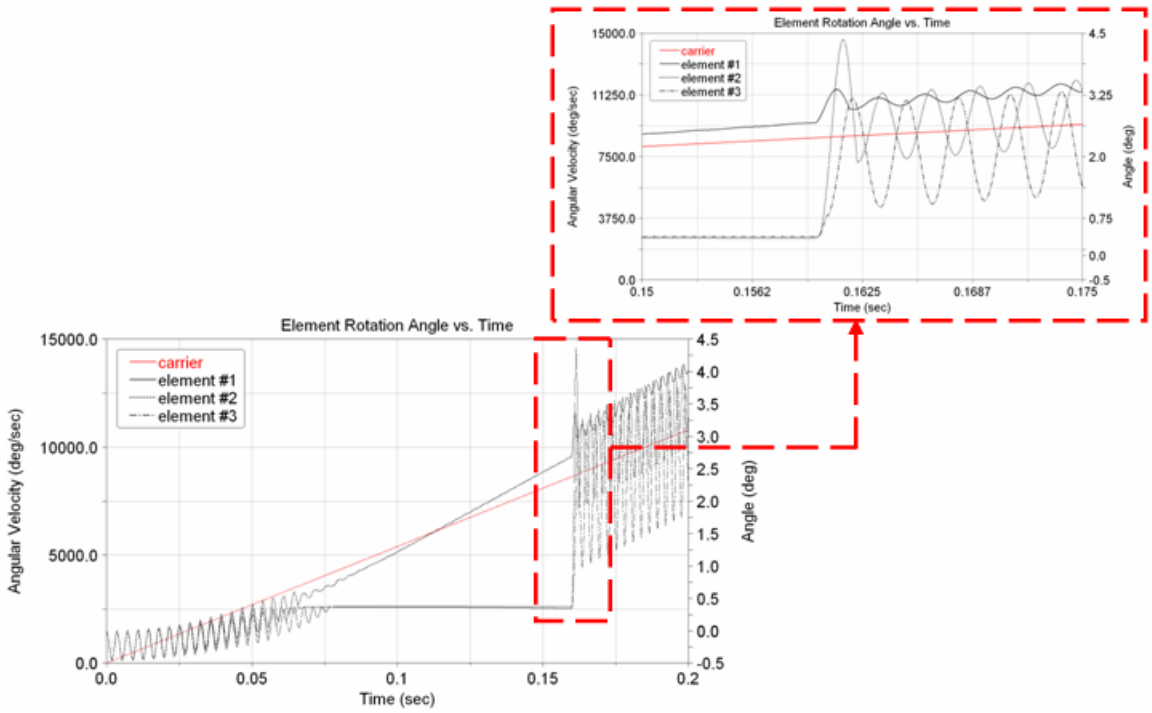

Figure 17 Three-element device numerical dynamic simulation.

2.2.2.3 Experimental Designs

Based on the above theoretical model and the device designs, four different device configurations were designed and fabricated. Each design used identical inertial masses and suspension springs, but with different critical angles. The devices were designed to be positioned with centers of mass located 28 mm from the center of rotation, and to initiate switching at angular speeds ranging from 20 rps (46 g) to 50 rps (285 g). System parameters for each of the four designs are provided in Table 2, including predicted time delays based on multi-body dynamics modeling. The switching speed increases with increase of critical angle of the first element. Delay time increases with increase of critical angle of the second element. Device and system geometric parameters are summarized in Table 3. The element sized was chosen to be about one fourth of that

of the macro-scale device.

Table 2 Summary of designed critical angles for the first and second elements in fabricated 3-element mechanisms.

	Design #1	**Design #2**	**Design #3**	**Design #4**
critical angle of 1st element (deg)	1.9	3.1	5.1	5.6
critical angle of 2nd element (deg)	1.2	1.8	3.8	4.3
theoretical switching acceleration (g)	34	72	184	223
theoretical delay time (ms)	1.1	0.8	0.7	0.7

Table 3 Summary of device and system parameters for simulated and experimental mechanisms.

α (deg)	**r_c (mm)**	**r_e (mm)**	**I ($kg \cdot m^2$)**	**m (kg)**	**leaf radius (mm)**
146	28	1.1	1.6×10^{-13}	1.7×10^{-7}	2

Two types of numerical simulations were conducted to obtain the element vibration dynamics. MATLAB numerical simulations were used to get numerical solution of the ODE formulas that theoretically describe the element delay time and element switching speed. Dynamic simulation software ADAMS was also applied to verify the theoretical results. In addition, the ADAMS simulation is also capable of obtaining element vibration dynamics of multiple-element micro time delay mechanism.

Chapter 3 – Device Fabrication

The micro time delay mechanism devices (Figure 18, Figure 19) were fabricated using a single mask, Silicon on Insulator (SOI) wafer and Deep Reactive Ion Etching (DRIE) process Figure 20. The starting substrates were 4" wafers with a 20μm thick single crystal <100> silicon device layer, 2μm thick buried oxide layer, and 500μm thick handle layer. The SOI wafers were first lithographically patterned and the device layer etched to the buried oxide using a DRIE tool (Surface Technology Systems, Newport, UK). The process parameters were tuned to achieve an etch rate of 1 μm/min or higher. Minimum resolution after DRIE processing was better than 3μm for both lines and spaces, allowing the gap between adjacent mechanism elements to be on the order of 2-3μm. The DRIE etching process was tuned to obtain relatively vertical and smooth sidewalls, and care was taken to minimize undercutting of the device layer through the well-known footing effect [37]. As a result, element contact area is believed to be evenly distributed along the vertical direction. The processed wafers were diced to obtain the desired chip size 7×12.3 mm. Diced chips were etched in 49% concentrated hydrofluoric acid (HF) for 35 minutes to remove buried oxide layer and release device mechanism. Released chips were transferred into a CO_2 supercritical point dryer (Tousimis, Rockville, MD) to prevent mechanism elements with high out-of-plane compliance from sticking to the device substrate [38].

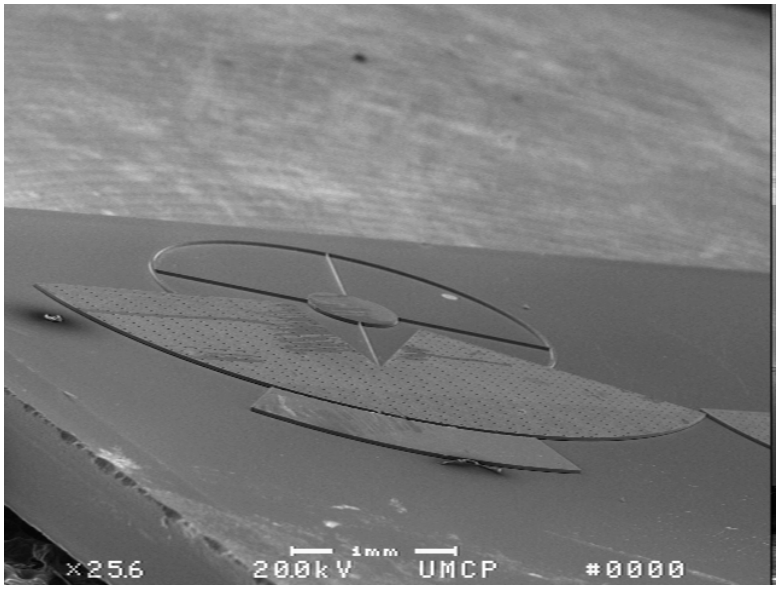

Figure 18 SEM of single element showing torsional suspension design.

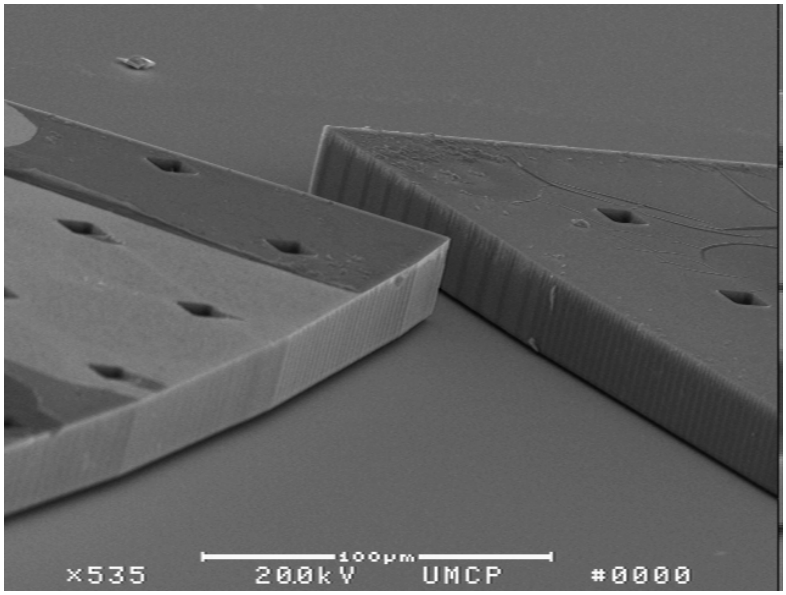

Figure 19 Closeup of pre-locked interface between mating inertial elements.

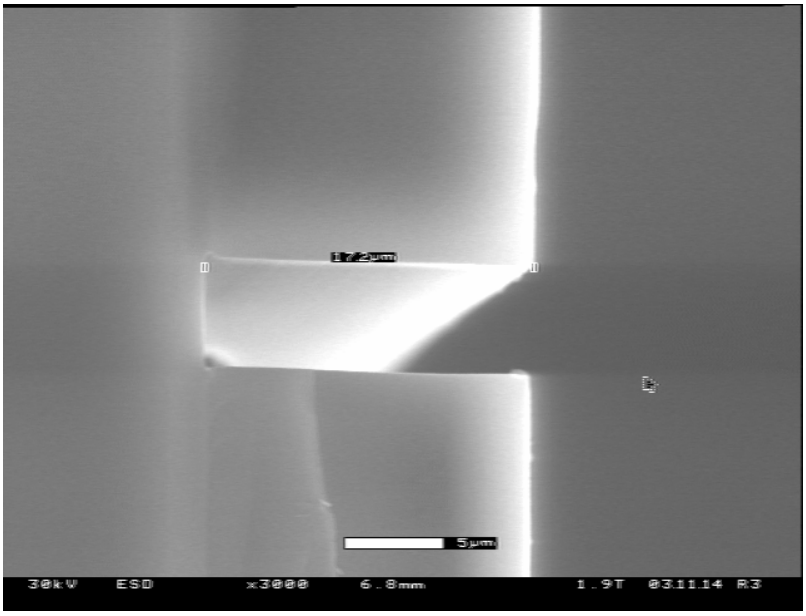

Figure 20 SEM of DRIE etched trench.

Typical dimension of the leaf time delay mechanism was 2mm. This large dimension element mass needed to be released after DRIE process ([38], [39], and [40]). It was found in the tests that the large dimension element mass was easy to stick on device substrate. This problem came from dewetting of released suspension structure after HF etching. After the HF release process, the device needs to go through several rinse and substitution steps before the super critical point drying process. The device was rinsed in DI water for three times, 5 minutes each time to remove HF residue. To check rinse effect, PH values of the rinse solutions were tested after every rinsing step. Typical PH values were 2.5, 5.5, and 7 after each of the three rinsing processes. Afterwards, device was rinse in Methanol for three times, 10 minutes each time to substitute water with Methanol solution. It was found that successful transfers between these rinse and substitution steps were critical in preventing device element from sticking on the substrate. This was realized by introducing a polyethanol transfer boat, Figure 21, to

carry chips from HF to deionized (DI) water and from DI water to methanol in wet environment, which prevented the 2μm gap between movable element and substrate from dewetting before the super critical point drying process. Results after super critical point drying process indicated that the transfer boat solution was testified to be able to solve transfer related stiction problems.

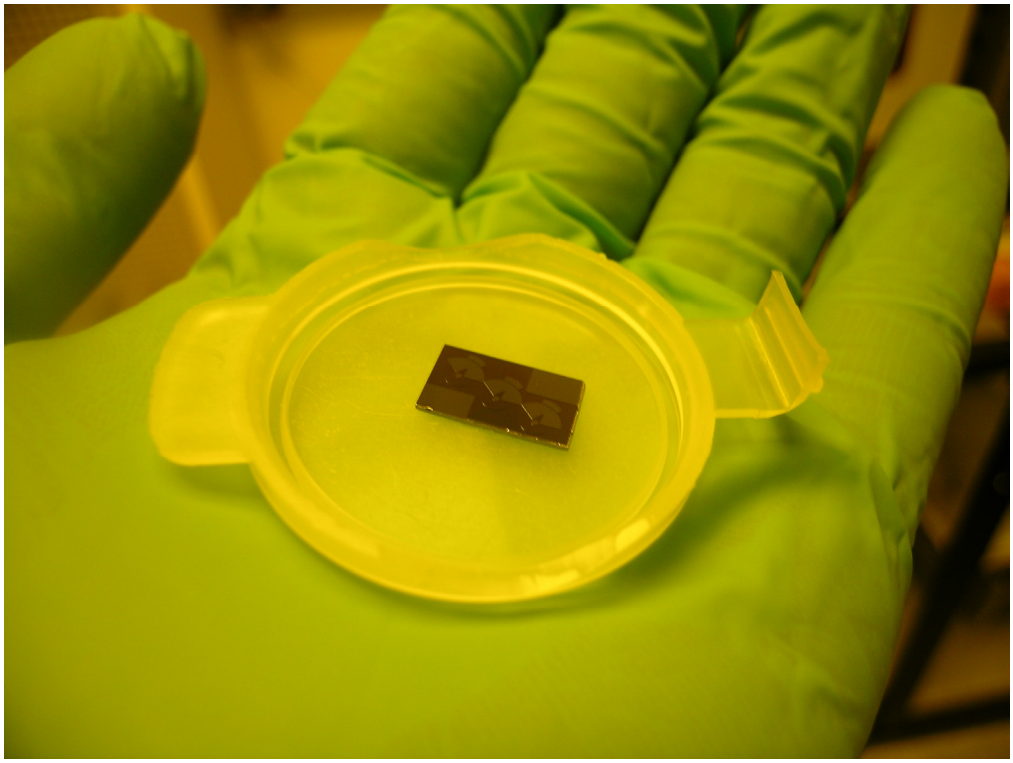

Figure 21 Device chip transfer boat.

The HF etching process is a diffusion-limited process [39]. Release hole size of 10 μm×10 μm ([39], [40]) was etched across the element area to allow the large dimension element mass to be released in reasonable time. The distance between adjacent etching holes was 60 μm, which accounted for less than 2.8% of surface area loss and element mass loss.

Chapter 4 – Device Testing

A testing system that could simulate the working environment of the leaf-type micro time delay mechanism by providing centrifugal force was setup. High-speed imaging technology was employed in testing of the leaf-type micro time delay mechanism. Selection of rotation platform and high-speed imaging system were detailed in this chapter. Generic testing method for rotational dynamics that could image small displacement on object with high-speed off axis rotation was developed, which demonstrated for the first time of real time monitoring for rotational time delay mechanism. Image processing technology was used to improve image quality of high-speed images and extend the capability of low end V4.0 high-speed camera to adapt to high rotation speed tests and to assist in post image analyses.

4.1 Image Processing to Improve Testing Results

4.1.1 Decrease Motion Blur

Endeavors of using image processing method to improve motion blur of high-speed images were conducted. Motion blur happens during high-speed imaging process. In order for the camera to image a moving object, the camera shutter needs to keep open during certain time period, i. e. exposure time. During this period, the object moves relative to the image sensor. The imaged object is projected at one location of the image sensor through the optical system at the moment the camera shutter is opened. Right before the shutter is closed, the imaged object moves and is projected at another location

of the image sensor. The displacment of the image projected on the optical sensor during the exposure time causes the high-speed image to be blurring. This motion blur exists on all cameras taking pictures of moving objects. Motion blur needs to be particularly considered when object being image moves in high speed, where the relative moving speed of the imaged object with respect to the camera is high. One general criterion for imaging acceptable motion blur is that the relative displacement of the moving object with respect to the camera during the exposure time is less than approximately 1/10 of the smallest feature to be resolved.

In the high-speed imaging tests that had been conducted in this dissertation, the relative moving speed of the imaged object with respect to the high-speed camera increases when the rotation speed of the rotation platform increase. When this relative moving speed reached certain level, the imaged object moved too much within the high-speed camera field of view during the shortest exposure time, which is determined by the highest shutter speed that is allowed to use. Motion blur becomes obvious under this large relative movement. Image processing was used to decrease this motion blur.

The image deblur processing is based on the Lucy-Richardson algorithm. For the motion blur induced in some of the high-speed imaging tests, the direction along which the object moves is known. The magnitude of the blur can be estimated from the platform rotation speed. A vector in spatial domain can be drawn to describe the direction and magnitude of the motion blur. Both the blur image and the blur vector are transformed into frequency domain. The frequency transform of the blurred image is then divided by the transform of the blur vector. After this calculation, retransforming the resulting image from the frequency domain back into the spatial domain restores the sharp image [42].

Figure 22 and Figure 23 show an example of how blurred image is improved by comparing images before and after the deblur image processing. From the deblur image processing tests, adopting image processing method to reduce motion blur approximately has the same effect of increasing the camera shutter speed of one to two levels. Figure 24 shows the boundary subtracted from the deblurred image by using Canny edge detection algorithm [42] to find the edge of the imaged mechanism element.

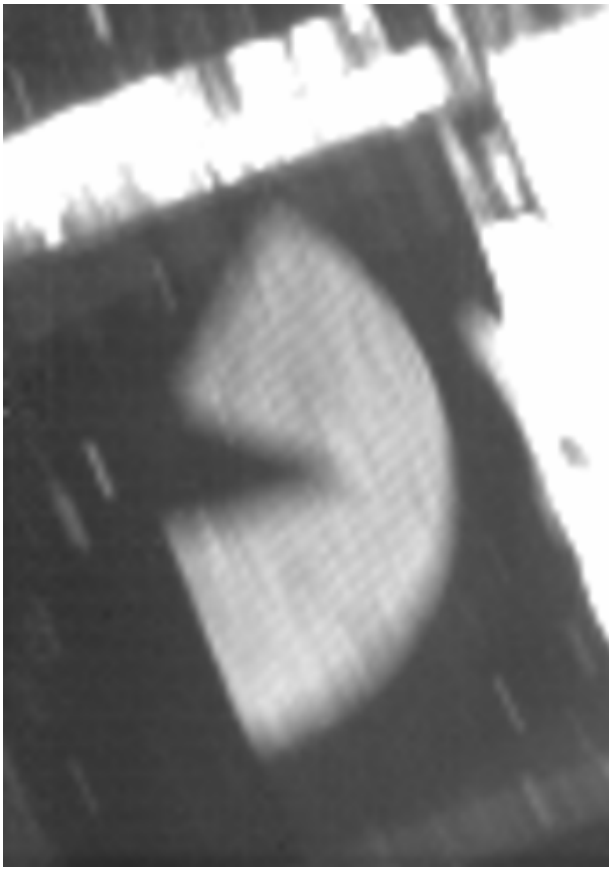

Figure 22 Blurred high-speed image.

Figure 23 Deblurred high-speed image.

Figure 24 Deblurred and edged high-speed image.

4.1.2 Identify Element Orientation

Besides image deblur, image processing was also used to was also applied to assist finding element orientation from high-speed camera images. In situation where the illumination is not enough, Radon transformation is helpful to find the orientation of the mechanism element of high-speed images. In the mechanism element high-speed images, the edges of the elements and element suspension springs are continued straight lines. And, the edges of the elements are the longest straight line. Using Radon transform [43] [44], the orientations of the longest straight lines in the images, which are the orientations

of the elements edges, can be determined.

The Radon transform is the projection of intensity of an image along a line with specific orientation. In Radon transform, the straight line is expressed by the line orientation angle (θ) and by the shortest distance from origin of coordinate system to the straight line (ρ). The Radon transform of a set of parameters (ρ, θ) is the line integral through intensity of the image *I(x,y)* along the line described by (ρ, θ) as in equation (4.1) [44]. The votes of many pixels in the image is summed up, and points in Radon space that have a large total vote are then interpreted as indicating the corresponding orientation in the real-space image. The transformation along different orientations can be summarized in two-dimensional plot. Figure 26 shows the Radon transform result from a high-speed image, Figure 25. Horizontal axis represents the angle of the orientation of the projection and the vertical axis represents the shortest distance from origin of the coordinate system to the straight line. The brightest point in Figure 26, the strongest projection, indicates the longest straight line. The slope of that straight line is 43^{o}, which is the slope of the edge of one element in Figure 25.

$$\boldsymbol{I}(\rho,\theta) = \int_{-\infty}^{\infty}\int_{-\infty}^{\infty} \boldsymbol{I}(\boldsymbol{x},\boldsymbol{y})\delta(\rho - \boldsymbol{x}\cos\theta - \boldsymbol{y}\sin\theta)\boldsymbol{dxdy} \tag{4.1}$$

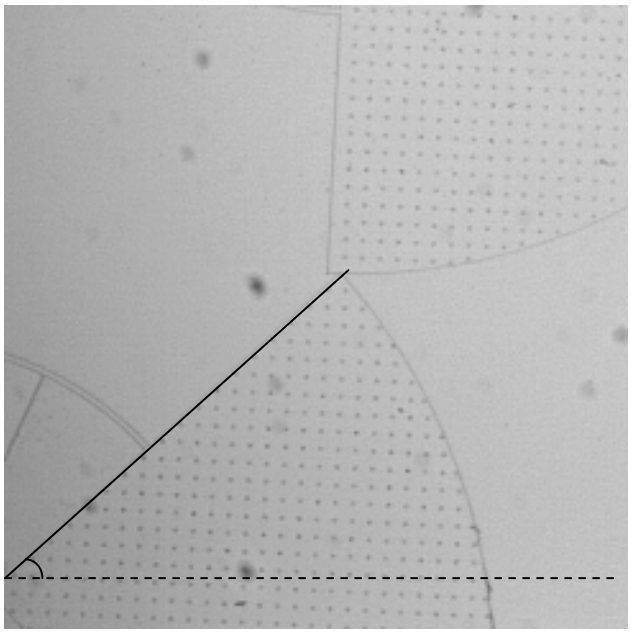

Figure 25 Original high-speed image.

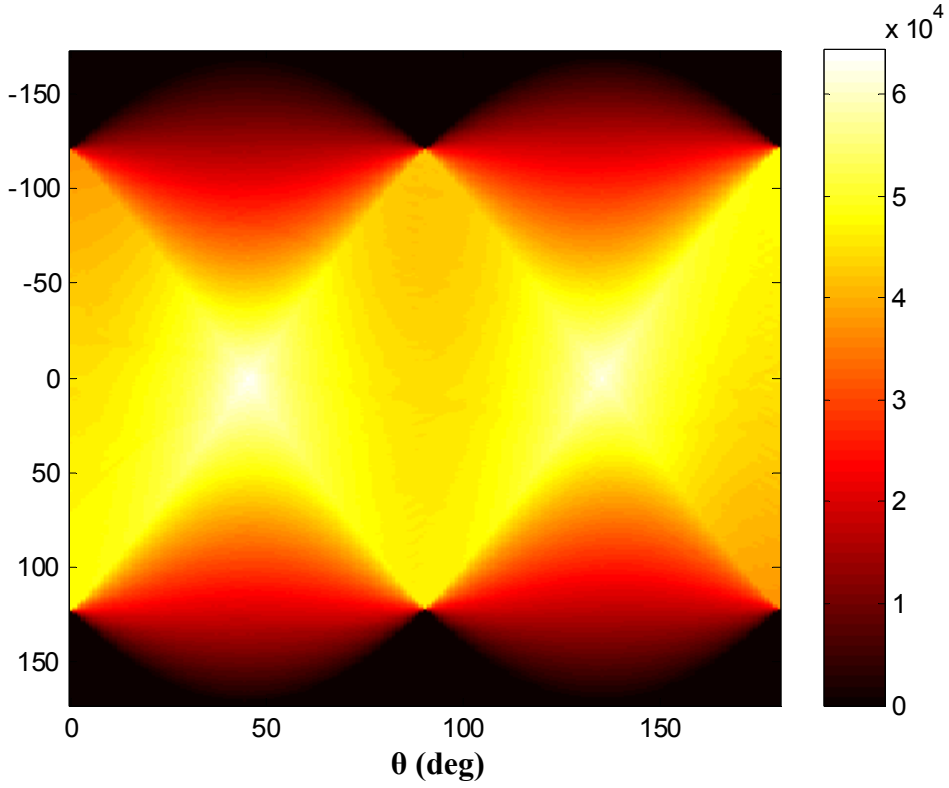

Figure 26 Radon transformation result from high-speed image.

4.2 Device Failure Mode Analysis

Single element devices with cantilever beam suspension springs were fabricated to explore their survivability at different rotation speeds and to explore influence of out of plane force from centrifuge vibration to the element vibrations. Cantilever beam suspension spring was selected because it was more sensitive to the out of plane force than the four-beam suspension structure. Devices were tested by using a single-speed (12,000 rpm) centrifuge, Eppendorf 5413 (Figure 27).

Figure 27 Single-speed centrifuge.

A plastic board was machined and fixed on the centrifuge rotor with four symmetrically positioned screws. A recess was machined on the plastic board to host the

device being tested. The device was fixed on the bottom of the recess using double side tape. A transparent glass slide covered and sealed recess opening to prevent the movable structure from being damaged by airflow generated during centrifuge rotation, Figure 28. The glass slide was fixed on the plastic board with single side tape.

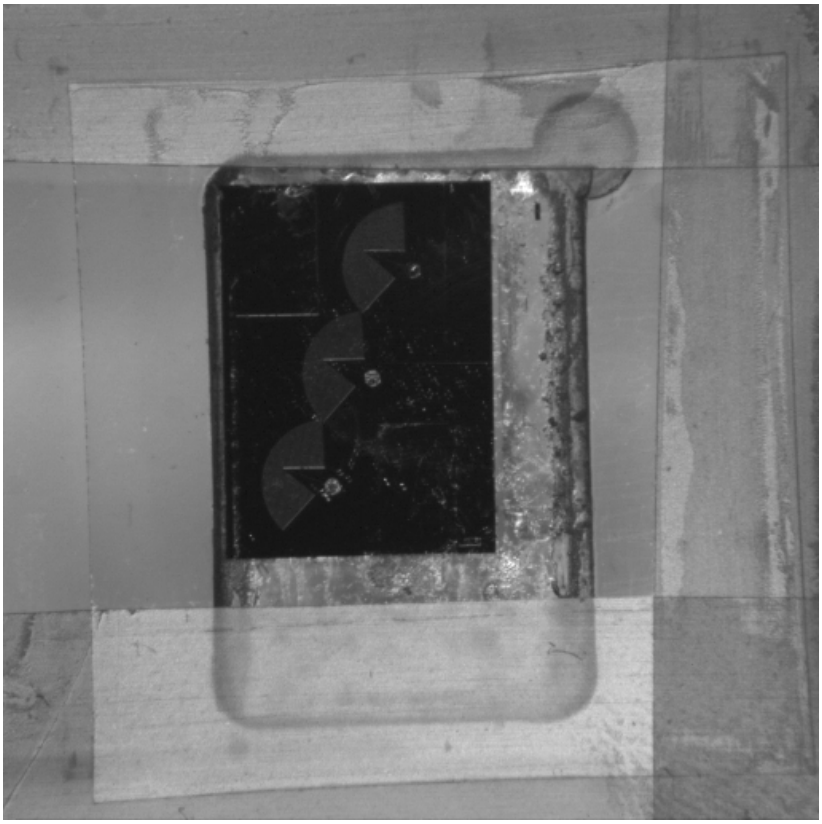

Figure 28 Sealed recess hosting test device.

The single-speed centrifuge used in the test is capable of accelerating its centrifuge rotor from 0 rpm to 12,000 rpm in approximately 60 seconds. Because the final centrifuge rotation speed is fixed and high for the testing purpose, device survivability tests were conducted by accelerating the centrifuge with different time durations so that rotation speeds less than 12,000 rpm could be realized. After the

acceleration procedure, the centrifuge was stopped to observe device status.

The single-element device successfully passed 3 seconds and 15 seconds acceleration tests. However, during 30 seconds acceleration test, device suspension beam broke. Fracture surface of the failed device was inspected under Scanning Electro Microscopy (SEM). Figure 29 gives overview of the element fracture and the element anchor after the 30 seconds acceleration test. Figure 30 shows the overall fracture surface. Figure 31 and Figure 32 tell details of bottom of the fracture surface. Figure 33 shows details of top of the fracture.

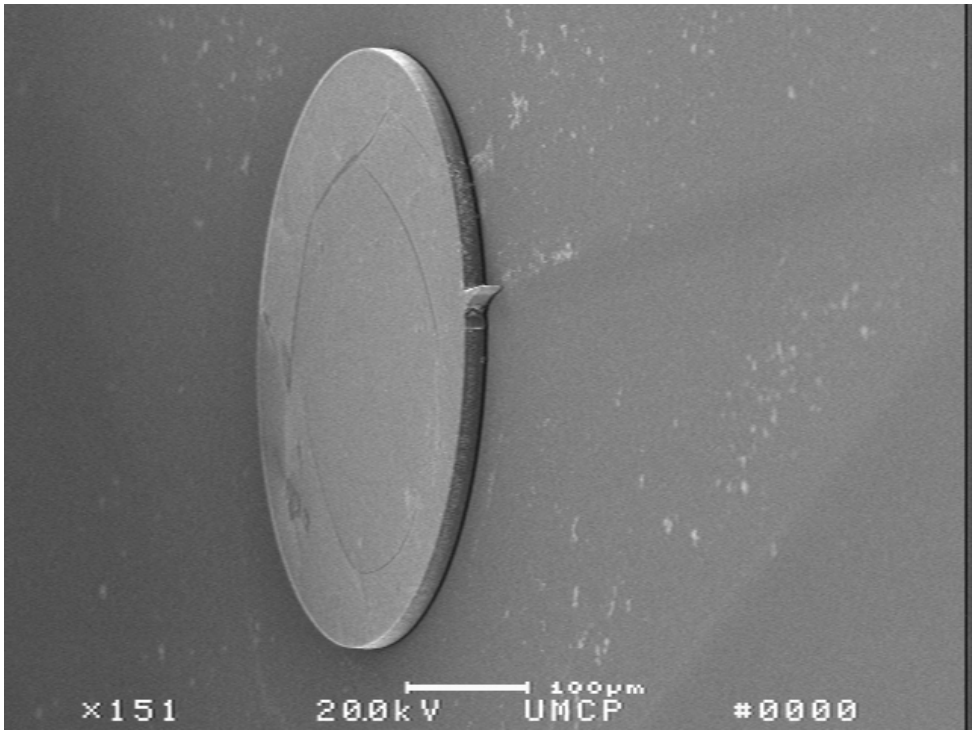

Figure 29 SEM of suspension beam breakage at device anchor.

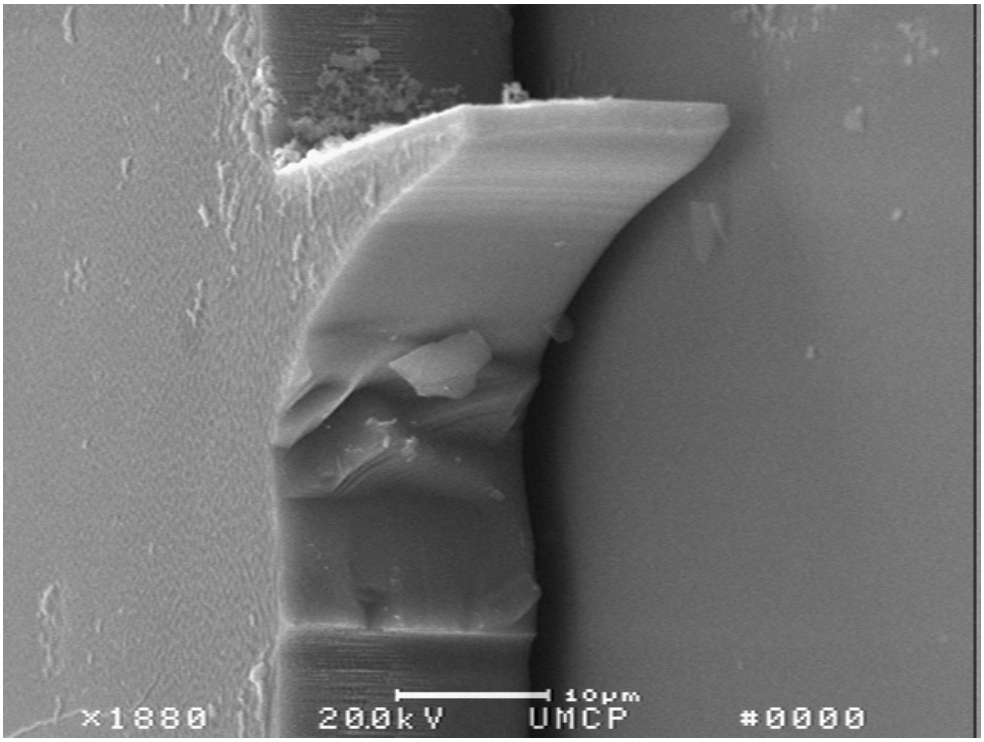

Figure 30 Overview of broken surface.

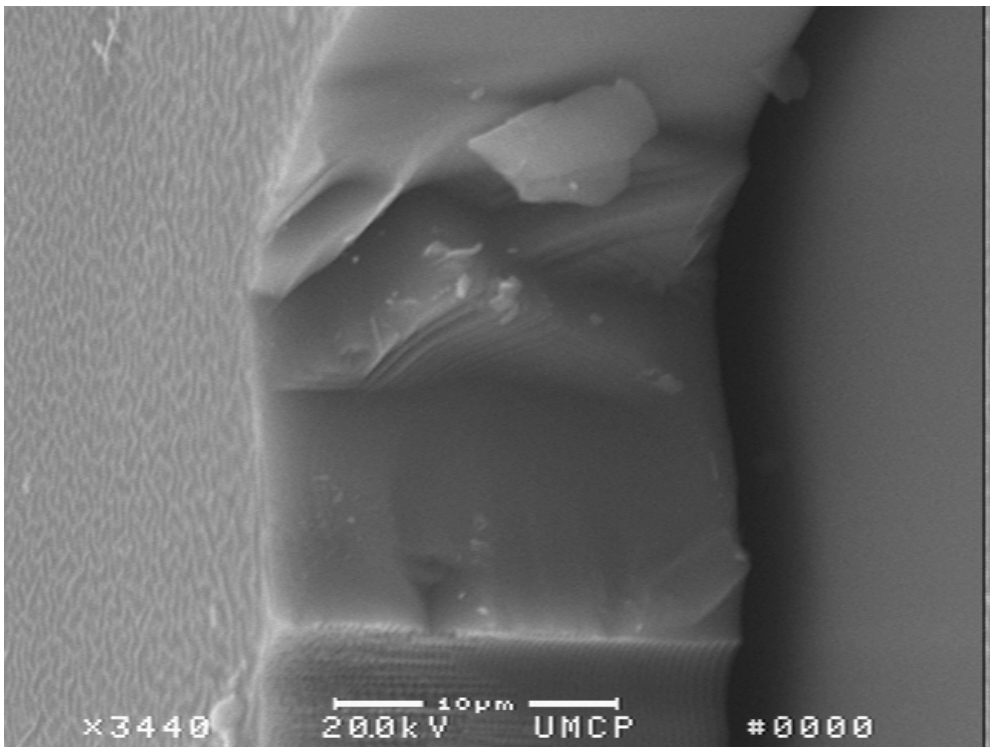

Figure 31 Closeup of broken surface (1).

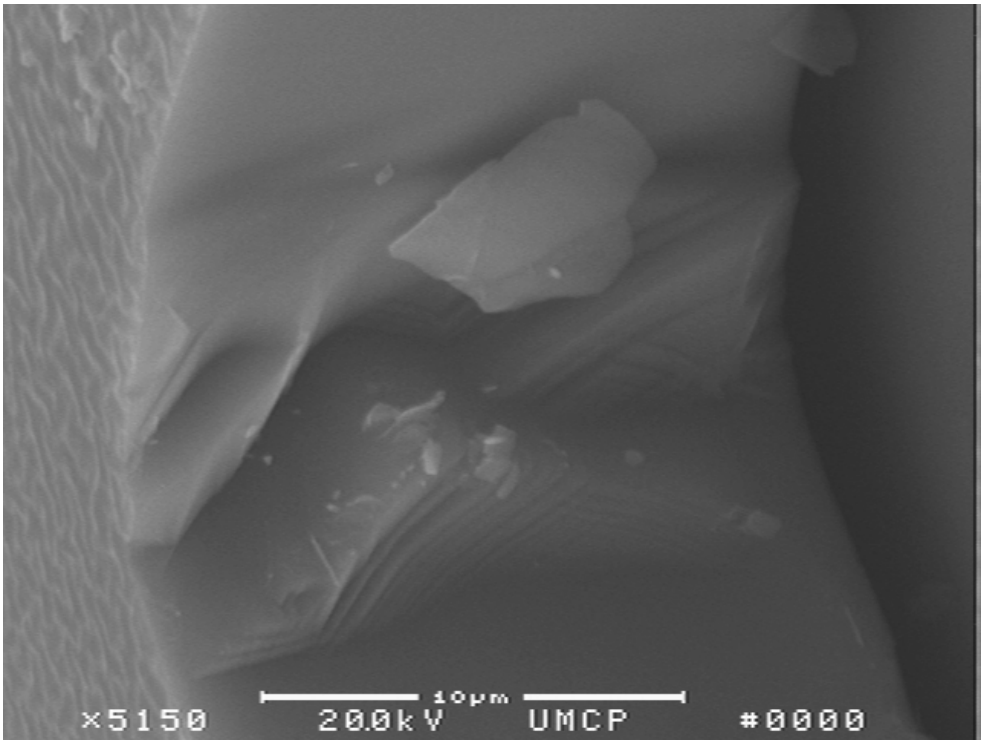

Figure 32 Closeup of broken surface (2).

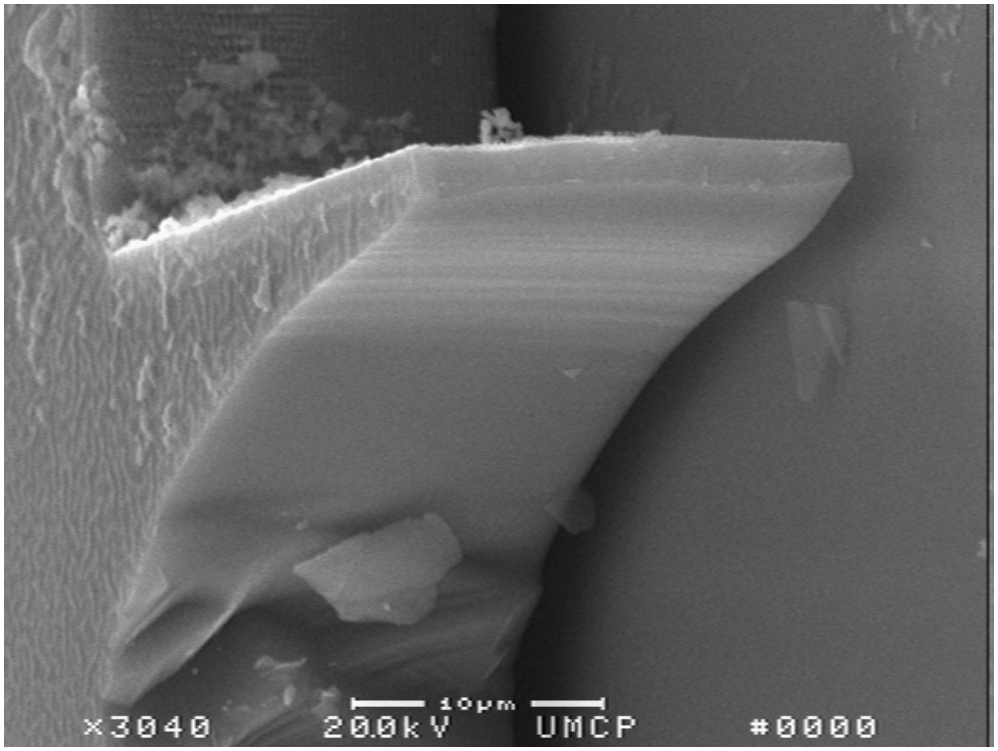

Figure 33 Closeup of broken surface (3).

To explore device failure mechanisms, failure mode analyses were conducted by comparing device failure fractures with typical failure fractures described in failure analysis reference [41]. Observed from the above SEM images, the fracture started and developed near the interface between end of the element suspension beam and the element anchor, where tensile stress was the largest, Figure 30. As seen from Figure 31, tensile bending overload was predominately presented. There was no sign of obvious torsion overload, [41]. After the fracture was initiated by the tensile stress, fracture area expanded while the suspended device element continued to vibrate. Out of plane fracture lines were observed when the fracture area expanded to the extent that the suspension beam could not be stable in the direction perpendicular to device substrate, Figure 32. At the end of the unstable fracture expansion stage, the suspension beam broke. The cracked

area created during this stage was smooth, as shown in Figure 33.

From the failure mode analyses, there was no sign of obvious failure due to torsional force. It was concluded that the current device element suspension design and the current experiment setup was able to keep the device vibrating parallel with the device substrate.

4.3 High-Speed Camera Demonstration Tests

To test the feasibility of using Phantom high-speed camera to record dynamics of the micro time delay mechanism rotating at high-speed and to explore tolerance of the image blur allowed by different camera exposure shutter speeds, high-speed camera demonstration tests were conducted.

Phantom V7.0 high-speed camera from manufacture was used in the demonstration tests. Because the available centrifuge has only one fixed rotation speed (12,000 rpm), photoresist spinner with adjustable rotation speed capability (SCS P-6708D, Figure 34) was used instead in the demonstration test to rotate device chip. A silicon substrate with a single-element device that was stuck on the substrate during the HF releasing process was fixed on a glass wafer by double side tape. The glass wafer was held on the photoresist spinner chuck by vacuum force during rotation. The size of the silicon substrate was 5mm×8mm. It was put at a location of approximately 40mm away from photoresist spinner rotation center. To illuminate the device element being imaged, a 250 Watt tungsten halogen lamp (Figure 35) was adopted.

In the test, the photoresist spinner was ramped up from 0 rpm to 6,000 rpm. The

high-speed camera shutter speed was set to 1μs, 2 μs, 5μs, and 10 μs respectively. Four videos were taken when photoresist spinner rotation speed reached 6,000 rpm with the above shutter speed settings respectively. Those high-speed camera shutter speeds were used to figure out which models of the available Phantom high-speed cameras were capable of imaging the device element with acceptable motion blur. The shortest shutter speeds of V7 and V9 cameras are 1 or 2 μs. V4 and V5 cameras have longer minimum shutter speeds of 5 or 10 μs.

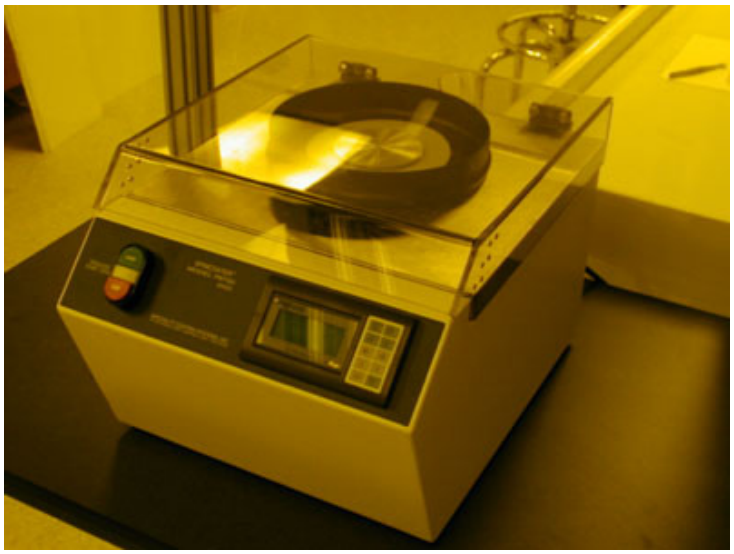

Figure 34 SCS P-6708D photoresist spinner.

Figure 35 250 watt tungsten halogen light source.

In condition of enough illumination and with current device image magnifications, the 1 μs and 2 μs high-speed camera shutter speeds gave acceptable images with acceptable image blur as could be seen from Figure 36 and Figure 37. Pictures taken with 1 μs camera shutter speed were especially clear. When the high-speed camera shutter speed went down to 5 μs, Figure 38, the image motion blur was clearly identified. When the shutter speed went further down to 10 μs, the image blur became obvious, Figure 39.

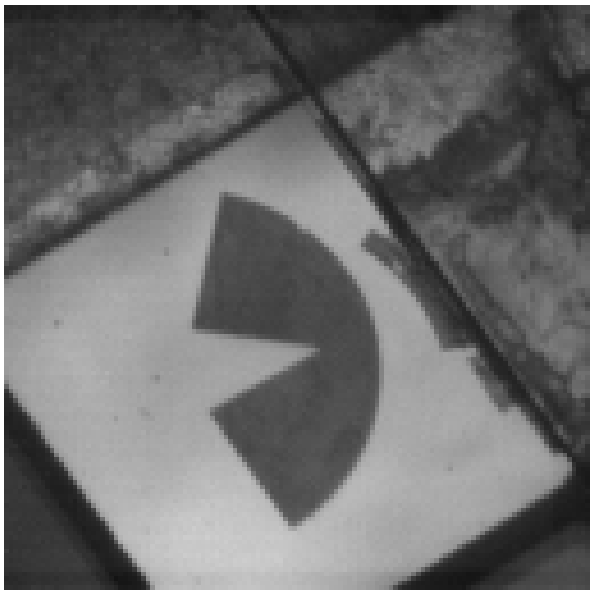

Figure 36 High-speed camera image (1us shutter speed).

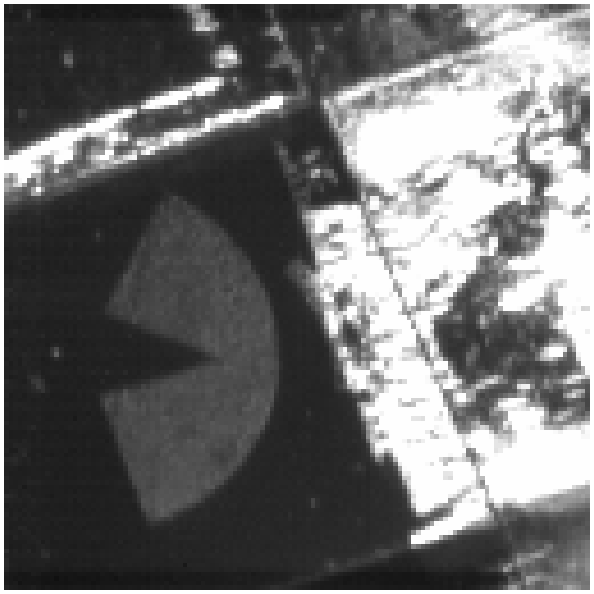

Figure 37 High-speed camera image (2us shutter speed).

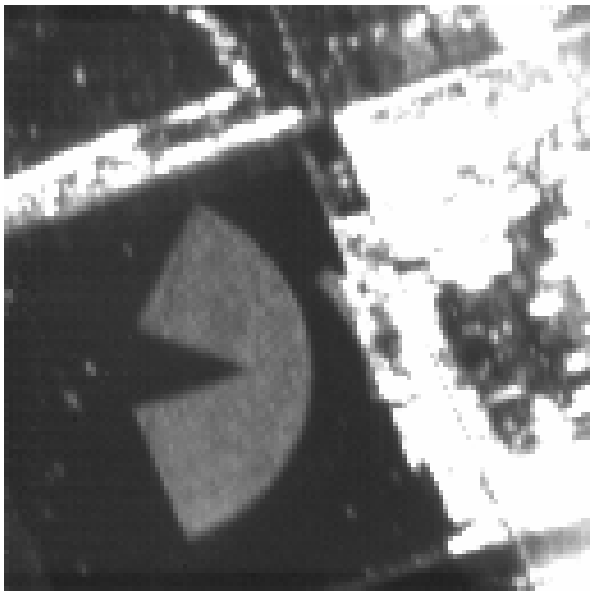

Figure 38 High-speed camera image (5us shutter speed).

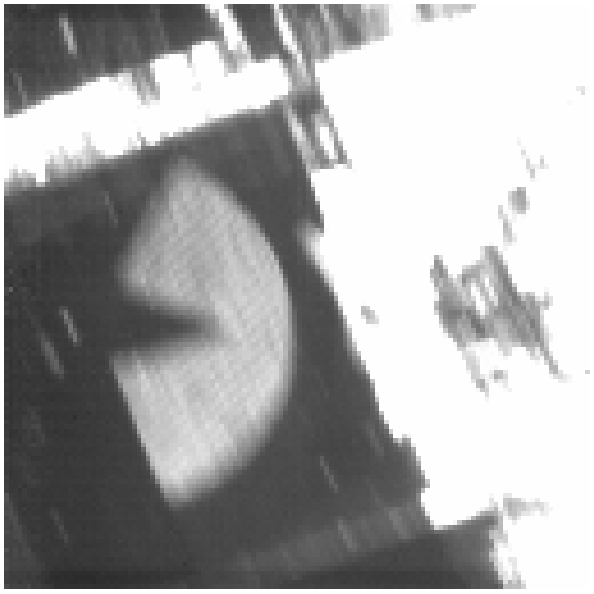

Figure 39 High-speed camera image (10us shutter speed).

Based on the above demonstration testing results, the V7.0 high-speed camera is capable of capturing pictures when the devices were put 40 mm away from the rotation

center and when the rotation speed reaches 6,000 rpm. The V7.0 high-speed camera has the highest shutter speed of 1 μs among all other Phantom cameras. The sensitivity of its COMS sensor is also the highest, 4,800 ISO/ASA. At maximum resolution, its 4,800 fps frame rate is the highest.

The image blur in the tests came from the specification limitation of the high-speed camera as well as from specified experimental conditions. At slower shutter speed, the imaged object travels more in the camera field of view than it does with higher shutter speed during the camera exposure time. When the ratio of travel distance over the dimension of the camera field of view becomes larger, the high-speed image will becomes more difficult to be identified. The portion of the blur coming from the high-speed camera is due to its shutter speed, the lower the shutter speed, the worse the blur. A few factors in the experimental conditions also contribute to the image blur. With higher rotation speed, device will pass faster under the high-speed camera, which reduces the possible exposure time of the camera. Device that was put farther away from the spinner rotation center will move faster under the high-speed camera with the same angular rotation speed and reduce possible camera exposure time. Higher magnification of the camera optical system is necessary when observing object details. With higher magnification, however, the allowed exposure time for the high-speed camera will be reduced.

4.4 Micro Time Delay Mechanism Switching Experiments

Switching tests were conducted on three-element micro time delay mechanism to

explore the speed at which the mechanism elements rotate passing their critical angles.

In the mechanism switching experiments, tests were done with the Phantom V4.0 high-speed camera that was available. The shortest shutter speed of the available V4.0 high-speed camera is 10 μs. The area being imaged was approximately 1/4 (1/2 along each linear direction) of the imaged area in the high-speed camera demonstration test. It indicated that the allowed exposure time for the high-speed camera was reduced by half. Because ISO/ASA sensitivity of the V4.0 high-speed camera was 1/3 of that of the V7.0 high-speed camera, the requirement on illumination became two times higher when other experimental conditions remained the same. To get rid of the constraints from decreased exposure time, 10 μs high-speed camera shutter speed constraint, and low light sensitivity the of the V4.0 high-speed camera, and to obtain high-speed images with acceptable blur, device was designed to be positioned closer, 20 mm, away from the photoresist spinner rotation center. The reduced rotation speed of 1,200 rpm was used.

At the beginning of micro time delay mechanism switching tests, the photoresist spinner was temporarily unavailable. Timed acceleration tests were conducted first on the single-speed centrifuge to obtain some initial device switching results without using the high-speed camera. Three-element time delay mechanisms were tested in the rotation experiments. The mechanism was fixed on the centrifuge. And timed acceleration, 3s, tests were conducted. After the acceleration procedure, the mechanism was inspected under microscope. It was found that the third element of this device switched and the three element interlocked with each other at their respective switched. Figure 40, Figure 41, Figure 42, and Figure 43 show the element interfaces after the timed switching tests. As could be seen from the figures, all the elements switched in the switching tests. The

switched elements could not went back to the original positions after the switching tests due to friction between adjacent elements.

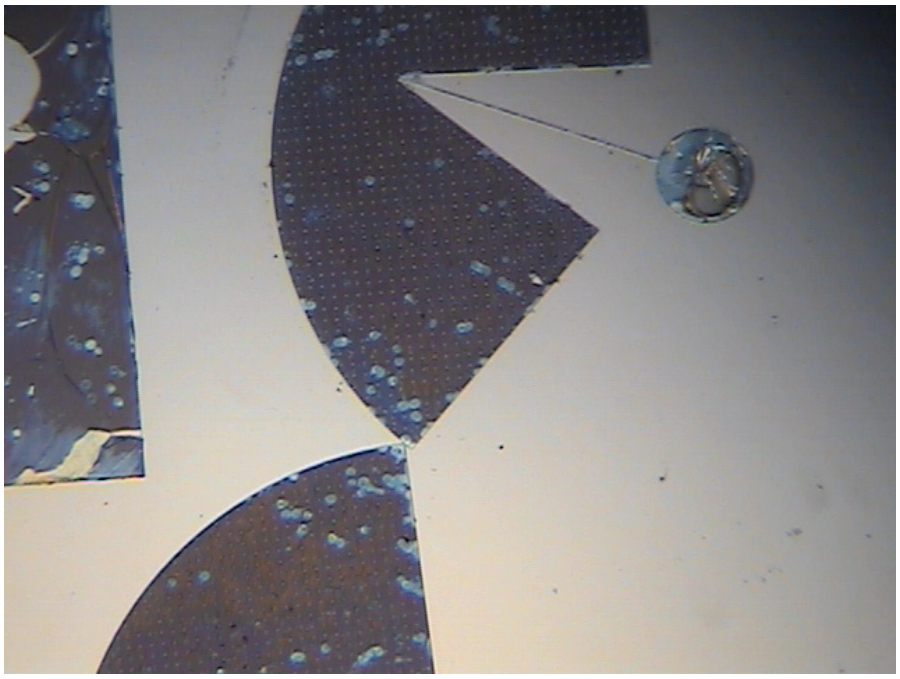

Figure 40 Overview of locked interface between element #1 and #2.

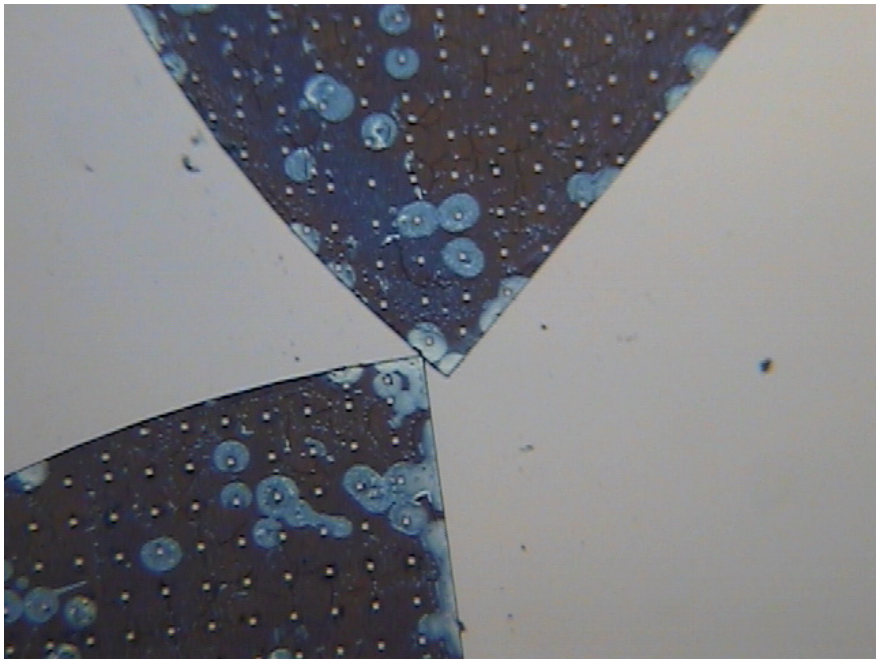

Figure 41 Detailed view of locked interface between element #1 and #2.

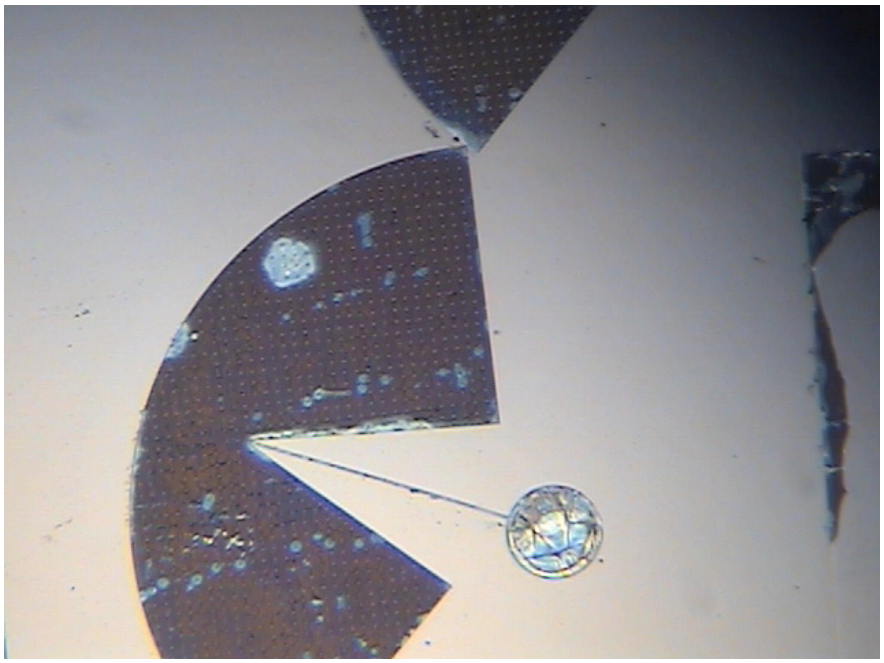

Figure 42 Overview of locked interface between element #1 and #2.

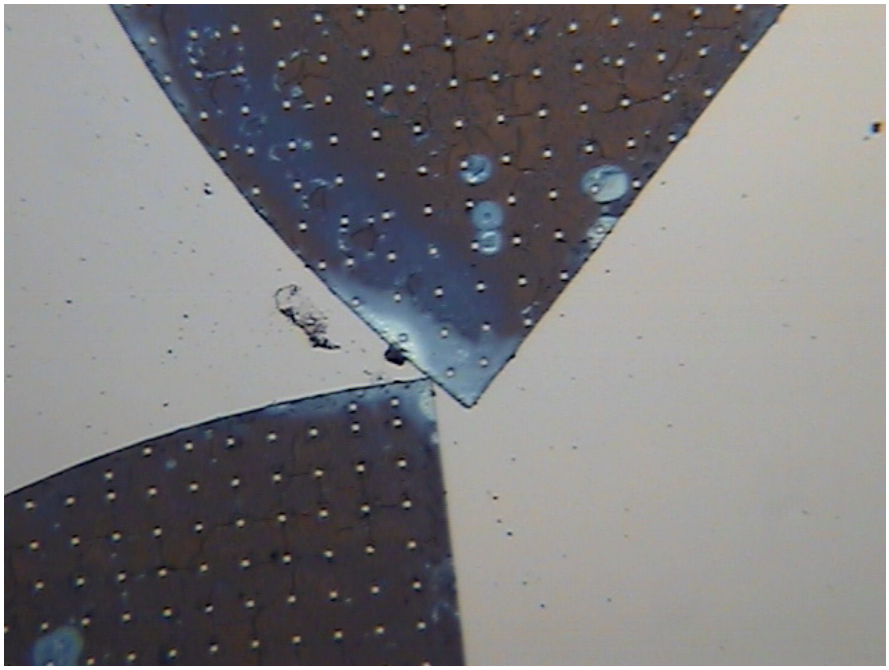

Figure 43 Detailed view of locked interface between element #2 and #3.

In order to test if the v4.0 high-speed camera was able to work with the single-speed centrifuge in the switching tests, the camera was put directly on top of the centrifuge and high-speed images were taken while the centrifuge was rotating. It was found that vibration of the centrifuge in the direction along rotation axis was too large during the centrifuge acceleration procedure. The images taken by the high-speed camera changed from in focus to out of focus while the centrifuge accelerated, which made it very hard to identify details of the micro time delay mechanism elements. As a result, the successive switching tests were changed from centrifuge rotation platform to photoresist spinner rotation platform to reduce influence from vibration along the axial direction.

To prepare for the tests with the photoresist spinner, the plastic board used in the centrifuge spinning test was modified. Its backside was polished with a series of polishing powders using a polishing machine. Large size polishing powder was applied

first and finer polishing powders were used in the successive polishing steps. The final polishing powder diameter used was as fine as 0.3μm. Polishing with small powder size made the processed plastic board flat enough to closely contact with the o-ring of the photoresist spinner chuck, which secured enough vacuum force to hold the plastic board during the rotation of the photoresist spinner.

In the experiments, the high-speed camera was designed to take one picture of the rotating micro time delay mechanism elements for every photoresist spinner revolution. The high-speed camera takes images when mechanism elements just passed under it. During the high-speed imaging procedure, the images were stored in the high-speed memory inside the high-speed camera before they could be downloaded to computer. The size of the high-speed memory limited the total number of images, i.e. the length of video that could be recorded by the high-speed camera. Typically, the recording length of the video is approximate 1 s when maximum image resolution 512×512 and full frame rate were used. The above high-speed camera recording mode reduced the number of recorded images compared with the high-speed camera working in continuous recording mode and made it possible to explore the mechanism behavior during the entire acceleration and deceleration procedure and to record longer event video. To realize this high-speed recording mode, an optical sensor was introduced to trigger the high-speed camera once the device passed under it. As shown in Figure 44 and Figure 45, illumination light was emitted from the optical emitter/sensor unit that was fixed above the rotation platform. A highly reflective tape was stuck on the surface of the rotation platform. It was put in the position that when the device paeed under the high-speed camera, light emitted from the optical emitter/sensor unit was reflected back by the

reflective tape to the optical emitter/sensor unit. An output of 5 V TTL pulse was generated from the optical emitter/sensor unit. This TTL pulse was sent to high-speed camera "Sync. Imaging" port as triggering signal to open the shutter of the high-speed camera. The camera shutter is opened for 10 μs exposure time and then closed to record one image. When the next TTL triggering pulse from the optical emitter/sensor unit arrived, the high-speed camera shutter was triggered again, the high-speed camera took a successive image. This procedure continued until the triggering process was interrupted.. For each photoresist spinner revolution, one device image was taken.

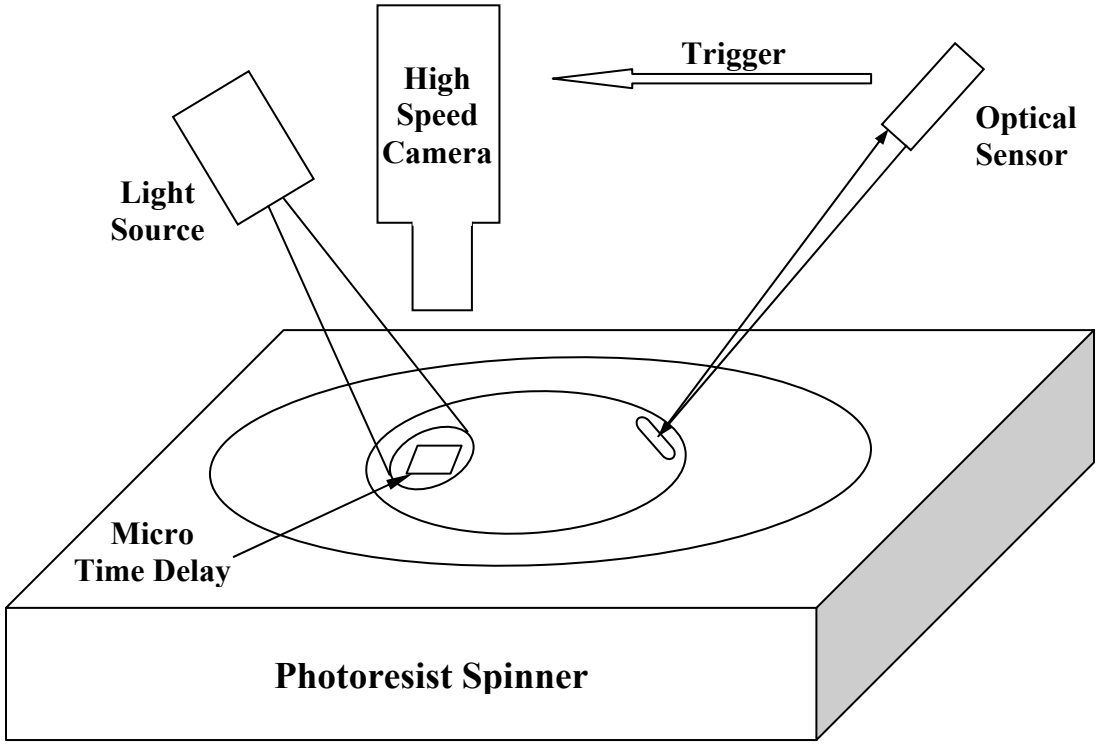

Figure 44 High-speed camera imaging system setup (1).

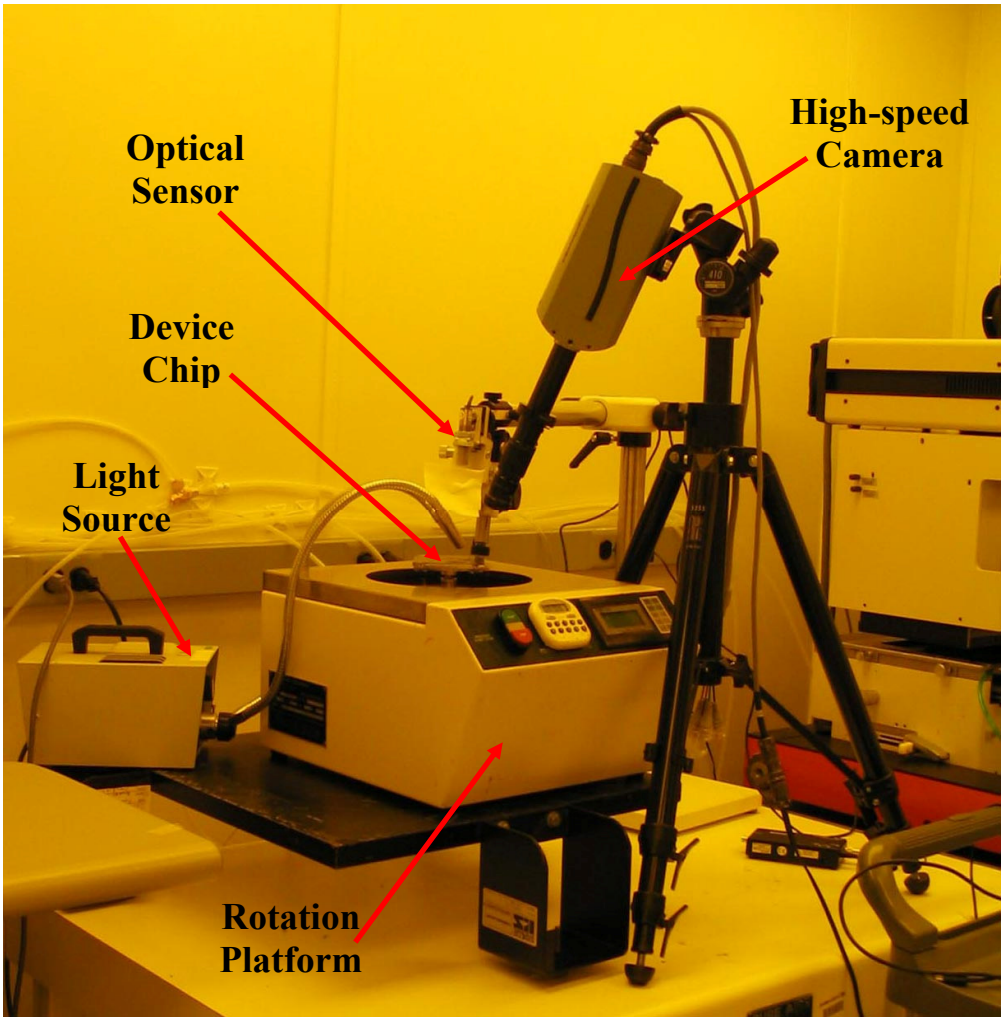

Figure 45 High-speed camera imaging system setup (2).

Before the real device tests started, a few adjustment steps were followed to verify that the high-speed imaging system setup worked properly. At first, the rotation platform, the high-speed camera, light source, and the optical emitter/sensor unit were put into approximate positions. Device chip was fixed on the plastic carrier board that was put on top of the rotation platform. After the rotation platform was powered on, it rotated at very low speed automatically. At this stage, the optical emitter/sensor unit was not connected to the "Sync. Imaging" port of the high-speed camera. The high-speed camera was set in

continuous recording mode. Precise relative position between the high-speed camera and the imaged device was adjusted by tuning tripod that held the high-speed camera and by adjusting the focus point and magnification of high-speed camera lens, so that the mechanism elements filled most of the camera field of view when passing under the camera lens. The adjustment results can be monitored directly from screen of the computer that controlled the high-speed camera. Low shutter speed and low light source intensity level were used in this step.

The second adjustment step was to synchronize the high-speed camera imaging properly with the rotation of the rotation platform, so that image of the mechanism elements was taken while passing right under the camera lens. For this purpose, the position of the reflective tape was adjusted to guarantee that a triggering pulse was generated when the mechanism elements passed right under the high-speed camera. Red light beam from the optical emitter/sensor unit was used to adjust relative position and orientation between the highly reflective tape pasted on the photoresist spinner and the optical emitter/sensor unit. The relative position between the high-speed camera and the reflective tape was adjust roughly through eye observing at the beginning. A green Light Emitting Diode (LED) indicator on the optical emitter/sensor unit that blinked upon receiving one reflective light pulse was used to further the relative position. After the adjustment, the indicator blinked when device passed under the high-speed camera. Upon finishing this alignment, output of the optical emitter/sensor unit was connected to the high-speed camera "Sync. Imaging" port. The photoresist spinner was rotated back and forth manually to trigger the optical emitter/sensor unit. The relative position between the camera and the imaged device was finely adjusted based on recorded images displayed

on the computer screen.

The third adjustment step was to slowly ramp up the photoresist spinner from 0 rpm to 100 rpm. At this rotation speed, the final relative position between the camera and the imaged device was determined. Light source intensity and imaging lens aperture were adjusted to ensure enough illumination and enough depth of focus can be obtained with the high-speed imaging system.

The optical emitter/sensor unit emitted red light on the reflective tape. Frequency of the red light wave fell in the light spectrum of the broadband light source that illuminated the imaged device. When the broadband light source became stronger, the optical emitter/sensor unit was interfered and could not output triggering signal properly. To solve this problem, a fiber optic light source was used to replace the previous broadband light source. Light from the fiber optic light source was more concentrated and thus brighter than the previous light source that illuminated larger area. Fiber optic light source also featured as cool light source, which prevented the illuminated objects from being heated up in short period.

Several tests were conducted with the above high-speed imaging system setup. A two-elements micro time delay mechanism was used in the tests. The initial tests aimed at exploring rotation speed at which the micro time delay mechanism switched. For this purpose, rotation platform ramping up time duration was fixed while varying the destination rotation speed of the rotation platform. In the tests, the ramp up time duration was set to 5 s. The final rotation speed was set to 100 rpm for the first test and 200 rpm for the second test, with 100 rpm rotation speed increasement on every successive test, until the micro time delay mechanism was able to switch. From the experiments, the

micro time delay mechanism ultimately switched at approximately 1,400 rpm. This approximate switching speed was obtained by referring to the time interval between two adjacent image frames recorded by the high-speed camera.

After the above tests, the switched device was inspected under microscope. It was found that after switching event, the mechanism elements locked together and could not went back to their original positions because of friction force between the two elements (Figure 46).

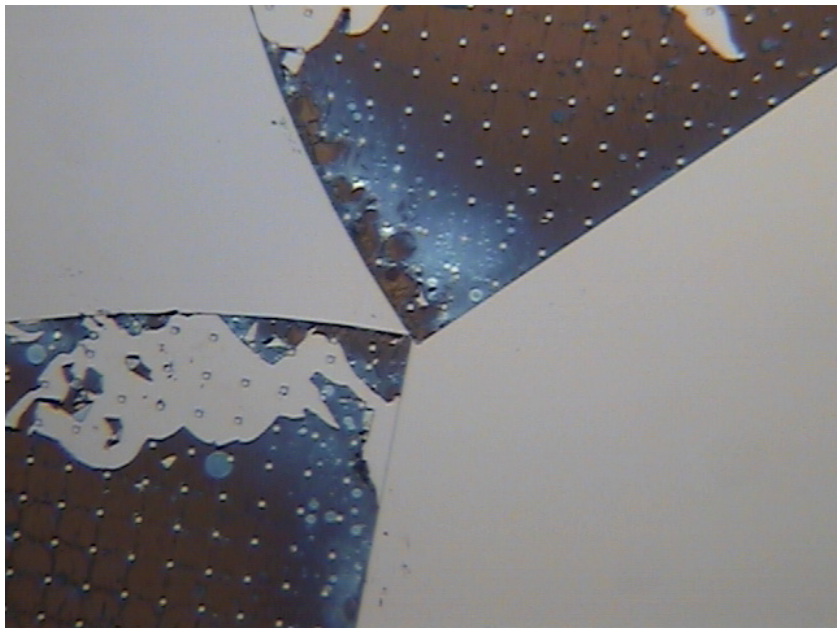

Figure 46 Interface of switched and locked elements.

Attempts were made to unlock the elements after the switching event. The device chip was fixed on platform of a probe station. Single probe was used to put elements back by slowly touching and moving elements around the location where elements contacted and locked together. The elements were unlocked successfully after these attempts as

seen in Figure 47. The success of manually unlocking the device elements made it possible to use the time delay mechanism repeatedly in tests. It was also possible to do comparative tests on the same device while changing experiment conditions.

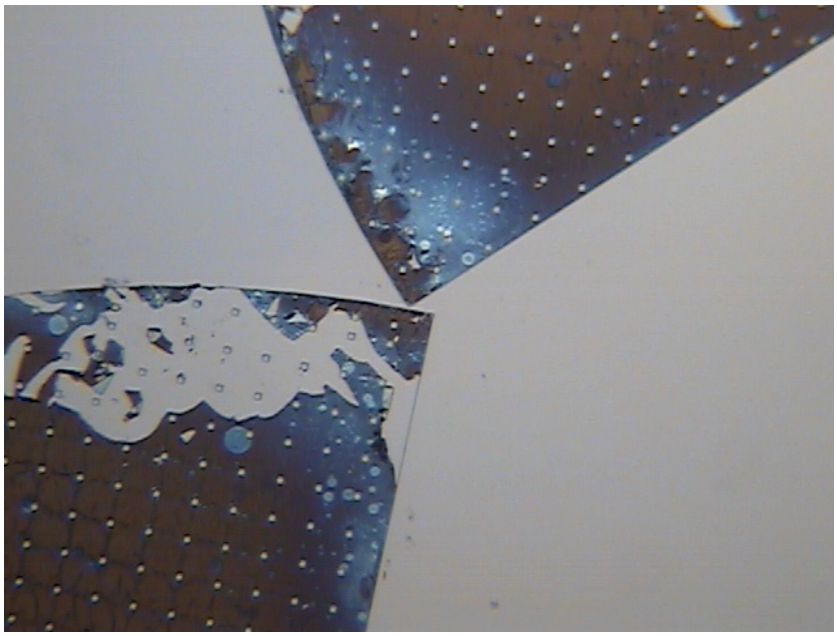

Figure 47 Interface of manually unlocked elements.

It should be noted that because the rotation speed was increased by 100 rpm on every successive test until the switching event, starting from the second ramping up procedure, the initial relative position between the two device elements may slightly different from their original relative position. Those two elements contacted with each other after the first ramping up procedure because of the friction between them. This could be observed by comparing the unlocked elements in Figure 47 with that in Figure 48 taken at the beginning of successive ramping up procedure.

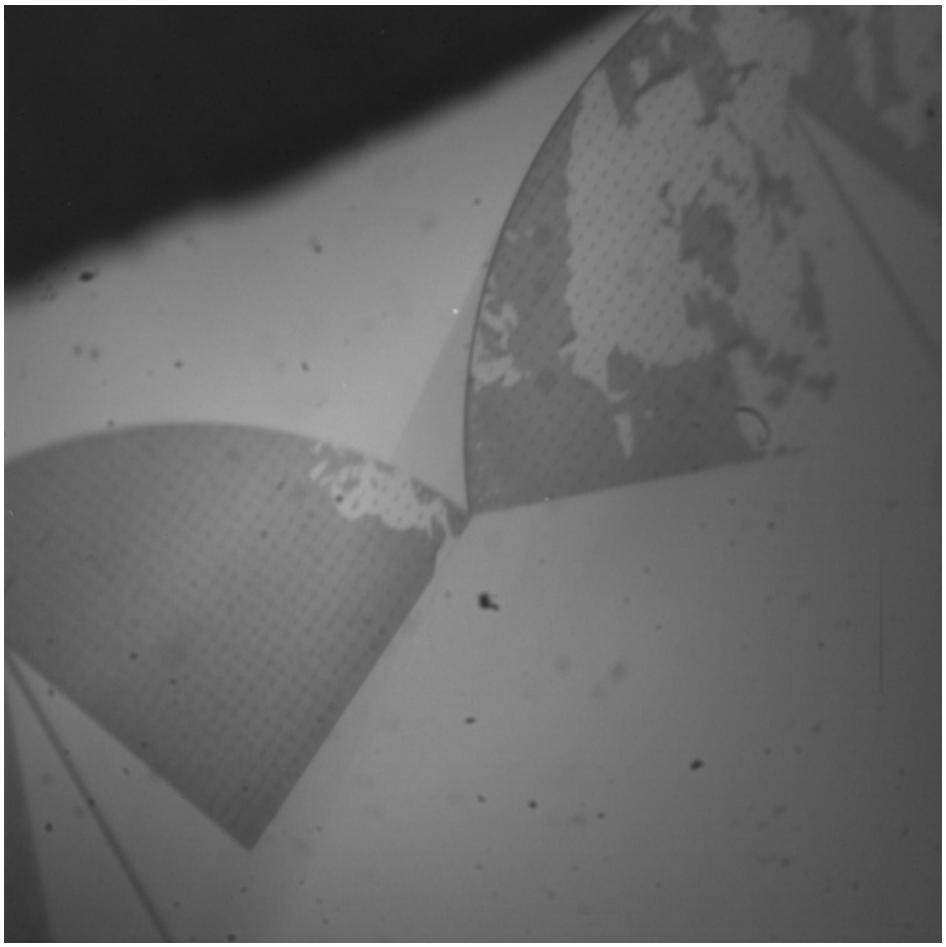

Figure 48 Elements relative position before switching event.

To get the actual rotational switching speed of the micro time delay mechanism, tests were conducted to accelerate the device from 0 rpm all the way to 1,500 rpm. It was found that the rotational switching speed was approximately 1,200 rpm, which corresponded to the designed rotational switching speed. Figure 49 shows the relative position of the elements in two adjacent images taken before and after the switching event by the high-speed camera. The arrows in the images indicate the moving direction of the mechanism elements.

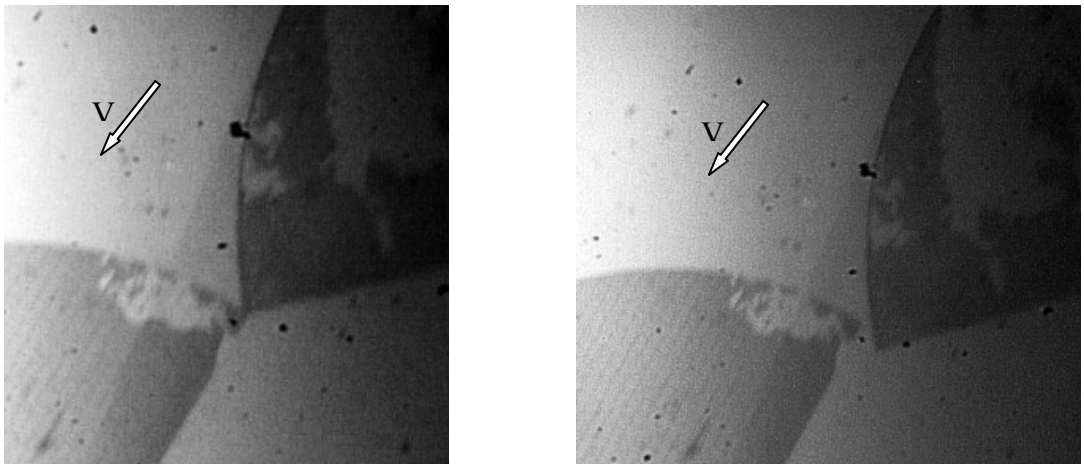

(a) **(b)**

Figure 49 Video frames showing device configuration (a) before and (b) after switching of the first inertial element. The substrate linear velocity is labeled V.

Several switching tests were conducted with different ramping up rates by changing ramping up time and keeping the same peak rotation speed as 1,500 rpm. These tests were done on the same device by unlocking the device elements after each element switching event, Table 4.

Table 4 Switching speed vs. ramping up time.

	Ramping Up Time (s)	Rotational Switching Speed (rpm)
Ramp #1	5	1239
Ramp #2	10	1204
Ramp #3	15	1231

It could be seen that the current device was not only reusable after unlocking, but also switched at similar rotational switching speed in different ramping up tests.

Relationship of element rotation angle with respect to rotation speed of the rotation platform of the second mechanism element was measured manually using high-

speed camera processing software. Seen from Figure 50, device element vibrated during the ramping up procedure. The switching event happened at approximately 1,200 rpm when element rotation angle increased sharply and beyond its designed critical angle, 1.2^{o}. After the switching event, the element continued to vibration with the element rotation angle much larger than that before the switching event. The element vibration after the element switching event came from actions of the centrifugal force as well as the element suspension spring. Friction force between contact elements was another factor that contributed to the element vibration before the switching event. It is noticed in Figure 50 that during the initial ramping up procedure, no rotation angle could be recorded by the high-speed imaging system. The reason is that there is limitation on the lowest frame rate allowed to use due to the design of the high-speed camera. Upon receiving the first triggering signal, the high-speed camera started to record. If the frequency of the trigger signal is lower than the allowed lowest frame rate, the allowed lowest frame rate is used instead, which resulted in over exposure during the initial ramping up procedure.

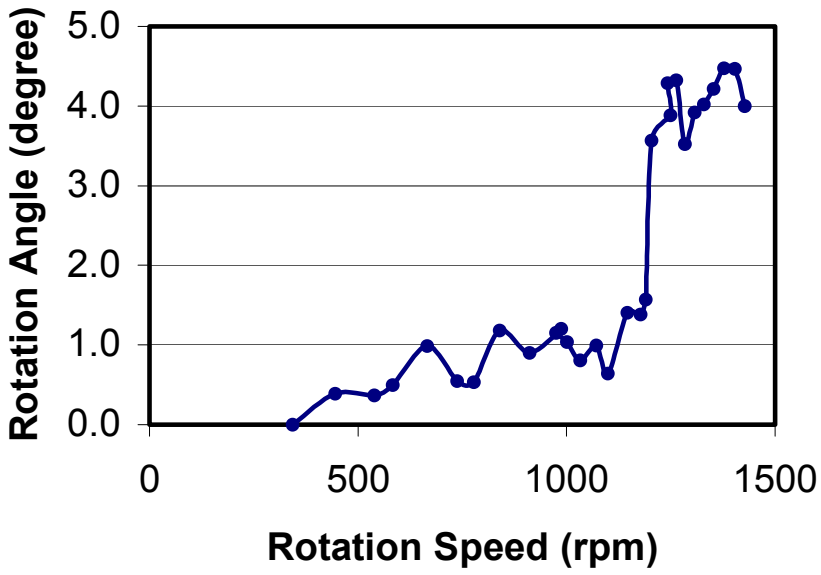

Figure 50 Experimental element switching curve.

During the rotation platform ramping up procedure, it could be observed from the high-speed images that the objected being imaged kept moving out of the fixed high-speed camera imaging window along device moving direction. Whereas during the rotation platform deceleration procedure, imaged device keep moving back into the fixed high-speed camera imaging window. The observed displacements were due to time delay of the TTL signal output from the optical emitter/sensor unit that triggered the high-speed camera. In the setup procedure of the high-speed imaging system, the high-speed camera was characterized at low rotational speed (100 rpm) to image object after the optical emitter/sensor unit detected the object position and output TTL triggering pulse. Time between the triggering TTL signal started to ramp up from 0 V until 5 V is the delay time of the optical emitter/sensor unit, which is a fixed delay time. The time duration between

the detection of imaged object and shutter opening of the high-speed camera remained the same. However, the imaged object moved more (less) within the high-speed camera imaging window with the increase (decrease) of the rotation speed of the rotation platform. As a result, the objected being imaged kept moving out of the fixed high-speed camera imaging window along device moving direction during the rotation platform ramping up procedure and keep moving back into the fixed high-speed camera imaging window during the rotation platform deceleration procedure. Method of minimizing delay time of the optical emitter/sensor unit by overcoming its low slew will contribute to keep imaged object inside the high-speed camera imaging window. For example, digital delay-pulse generator with high signal slew rate could be inserted between the optical emitter/sensor unit and the high-speed camera. Its capability of being triggered at very low voltage level (less than 1 V) and outputting 5V TTL signal with high slew rate (within 250 ns) after triggered by the optical emitter/sensor unit output signal. So that, the output signal from the optical emitter/sensor unit only needs to ramp up to less than 1 V at low signal slew rate, which reduces the influence from the slower slew rate of the optical emitter/sensor unit.

4.5 Rotation Mirror Experiments

From the above mechanism switching tests, the concept of rotary-type micro time delay mechanism was testified. The mechanism switching speed and vibration magnitude of element rotation were obtained. However, due to the triggering technique, the camera frame rate was limited by the rotation speed of the photoresist spinner. In the above

mechanism switching test, the switching speed of the specific mechanism design was approximately 1,200 rpm. It indicated that the high-speed imaging system sampled one image for every 50 ms. As revealed in the following experiments, the switching event happened within approximately 1 ms. The above 50 ms time interval between adjacent image frames is too long to be able to capture the element vibration dynamics occurred during the switching event. On the other hand, the capability of the high frame rate of the high-speed has not been fully utilized to obtain better quality high-speed images. In view of these issues, image projection plan was explored to capture the device switching dynamics during the element switching event.

In the above trigger-synchronization high-speed imaging experiments, the device chip rotated around the rotation center of the rotation platform, whereas the high-speed camera was fixed at certain distance from the rotation center of the rotation platform. With acceptable image resolution, the field of view of the high-speed camera was far from enough to cover the entire track of the rotation of the device chip. The light source could not provide enough power to illuminate large area. To solve these constraints, the high-speed camera was moved above the rotation center of the rotation platform, and the image of the device chip was displaced from the location at certain distance off the rotation center of the rotation platform to its rotation center. So that during the device rotation, the entire track of the rotation of the device chip was limited to area around the rotation center of the rotation platform. The high-speed camera was placed right above the rotation center of the rotation platform to image the pure rotating image of the device chip. A rhomboid prism was used to project the device chip image from off the rotation center of the rotation platform to its rotation center through two total reflection processes,

Figure 51. The rhomboid prism is normally used to displace light beam, ex. laser light beam without changing its direction. It was used in the experiment to displace image of the device chip. By adopting the image projection testing method, at any moment during the rotation process, the projected device chip image was always rotating within the field of view of the high-speed camera. As a result, the high-speed camera can image at maximum frame rate under acceptable image resolution. In addition, the high-speed camera can concentrate on details of the imaged device chip by using higher lens magnification. The light source only needs to illuminate device area. Small displacement of micro devices can be recorded with this high-speed imaging system design and setup.

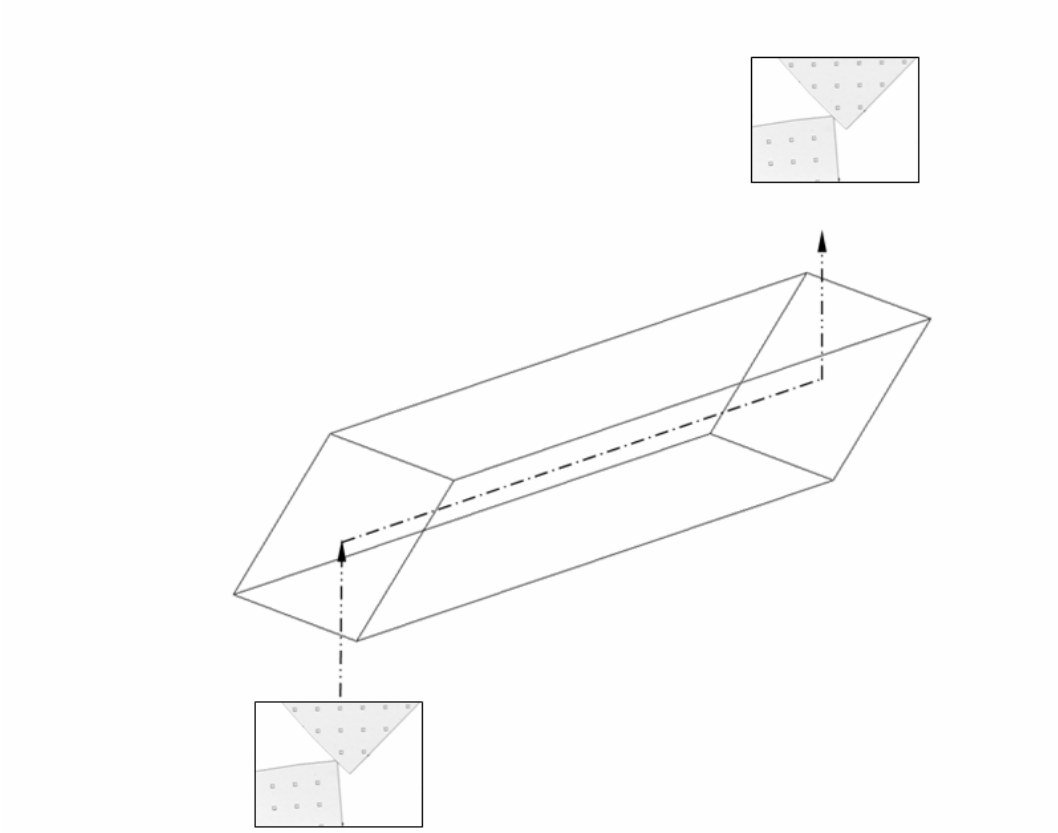

Figure 51 Schematic of image projection using rhomboid prism.

Devices were characterized experimentally using the setup shown in Figure 52 and Figure 53. Each chip was secured inside a recess on a plastic carrier using double side tape. The carrier was bolted to a computer-controlled rotation platform based on a modified photoresist spinner capable of accelerating the chip carrier to speeds of 83 rps. The center of the recess was located 28 mm from rotation center. A rhomboid prism (source Edmund Optics Inc., Barrington, NJ) was positioned with one end over the chip, and the other end centered on the rotation axis of the carrier. The rhomboid prism projected the mechanism image to the chip carrier rotation center through two total internal reflections from the end faces of the prism, thereby displacing the chip image by

a predefined radial distance defined by the length of the rhomboid prism. Using this approach, a camera positioned over the rotation axis was able to image the chip regardless of the rotation angle of the carrier, enabling long exposure times and eliminating the need for synchronizing image capture from a static camera located at the same radial distance as the chip. Thus, the time interval between two adjacent frames was determined only by the frame rate limitation of the camera. The high-speed Phantom v4.0 camera (company info Vision Research Inc., Wayne, NJ) enabled 3,700 frames per second capture with a 0.27 ms frame interval and 256×256 image resolution. A 6.5:1 ratio zoom lens, Zoom 6000 with co-axial illumination capability (Navitar, Rochester, NY) is used for image projection and illumination. Another advantage of this testing setup was that the field of view of the high-speed camera was concentrated only on the small area where the element switching occurred, allowing high resolution imaging of the switching event to be performed.

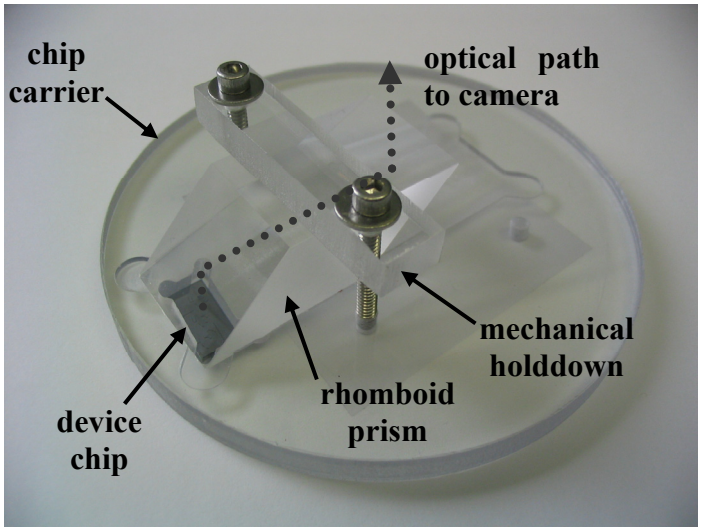

Figure 52 Chip carrier including rhomboid prism optics, with the optical path to the camera aligned to the rotation axis of the spin table.

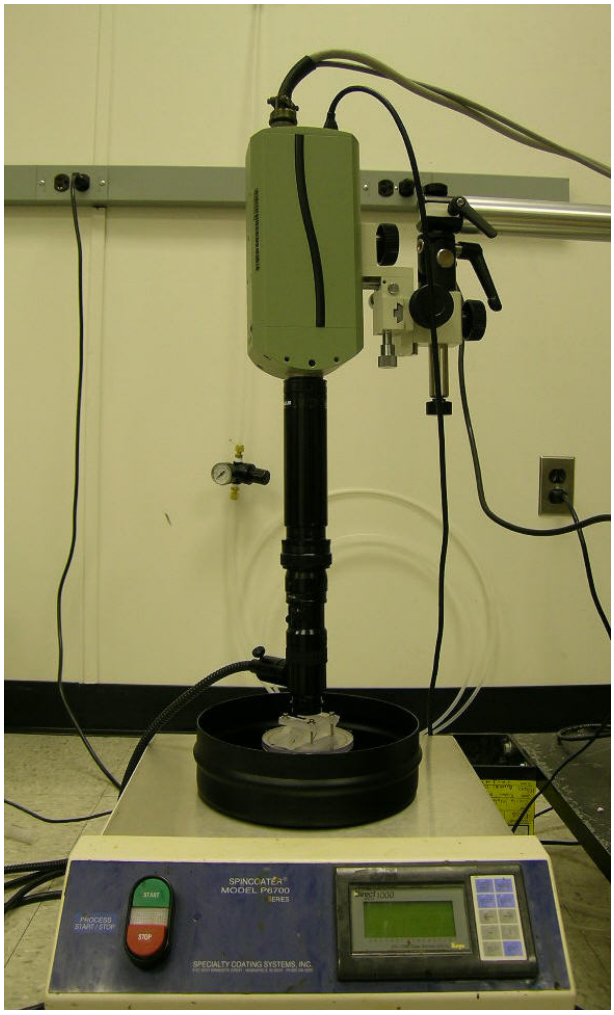

Figure 53 Overall experimental setup.

To ensure the center of projected image was aligned with the chip carrier rotation center, CNC milling was used to fabricate the plastic chip carrier, and device chips were diced to position the mechanism precisely at the chip center. Using this method position tolerance was controlled to within 100μm. Also note that the rhomboid prism covered and sealed the recess opening housing the chip, so that no air flow occurred across the chip face, preventing the mechanism elements from being damaged or blown away during acceleration. In order to keep the chip carrier in balance during rotation, an

identical rhomboid prism was fixed on the opposite side of the chip carrier. A 150W ACE® DDL fiber optic light source (Schott Fostec, Auburn, NY) was used to illuminate the mechanism through the imaging lens of the high-speed camera, ensuring sufficient brightness for high quality imaging and eliminating the need for a high-power light source. With the precise projection alignment, only the switching area need to be imaged, this reduces the requirement on the intensity of light source.

The device mechanism is fabricated from SOI wafer. The device mechanism and device substrate are all silicon materials. It was conceived during the trigger-synchronization experiment that the same high reflective silicon material makes it difficult to differentiate device mechanism from background substrate. Therefore, photoresist after DRIE process was not stripped off after the chip dicing process step. This provides high contrast between device mechanism and substrate background. However, to identify details of element through the optical system the low reflective photoresist requires brighter light source than high reflective silicon material. In the image projection experiment, attempts were made to totally remove the photoresist on top of the element surfaces. It was found that although both imaged object and substrate background were of the same high reflective silicon material, the device mechanism could be clearly identified through the high-speed imaging system. In the mean time, the high reflective surface of the device mechanism reduced the requirement on illumination. On the other hand, however, it was not easy to put the camera perfectly perpendicular to the device substrate. As a result, the light reflected back to the high-speed camera varies while the device carrier rotates. It is found in the experiment that the dynamic range of the high-speed camera can accommodate the light variation and able to obtain measurable

images.

With the above setup, each of the four different 3-element mechanism designs was tested to determine the switching dynamics and delay times.

Figure 54 shows eight successive images during a typical switching event, revealing the progressive increase in rotation angle for element #2, and finally the unlocking of element #3 once the critical angle is reached. Rotation angles were measured using image processing software provided with the camera. Angle measurement tolerance was approximately 0.2^{o}. Figure 55 shows the switching dynamics of both low-speed (design #1) and high-speed (design #4) devices. Each data point in the plots represents angle measurements from one image frame, with a time interval between successive image frames determined by the camera capture speed of 0.27 ms. Time delay was obtained by counting the number of frames between the initial rotation of element #2, and the initial rotation of element #3.

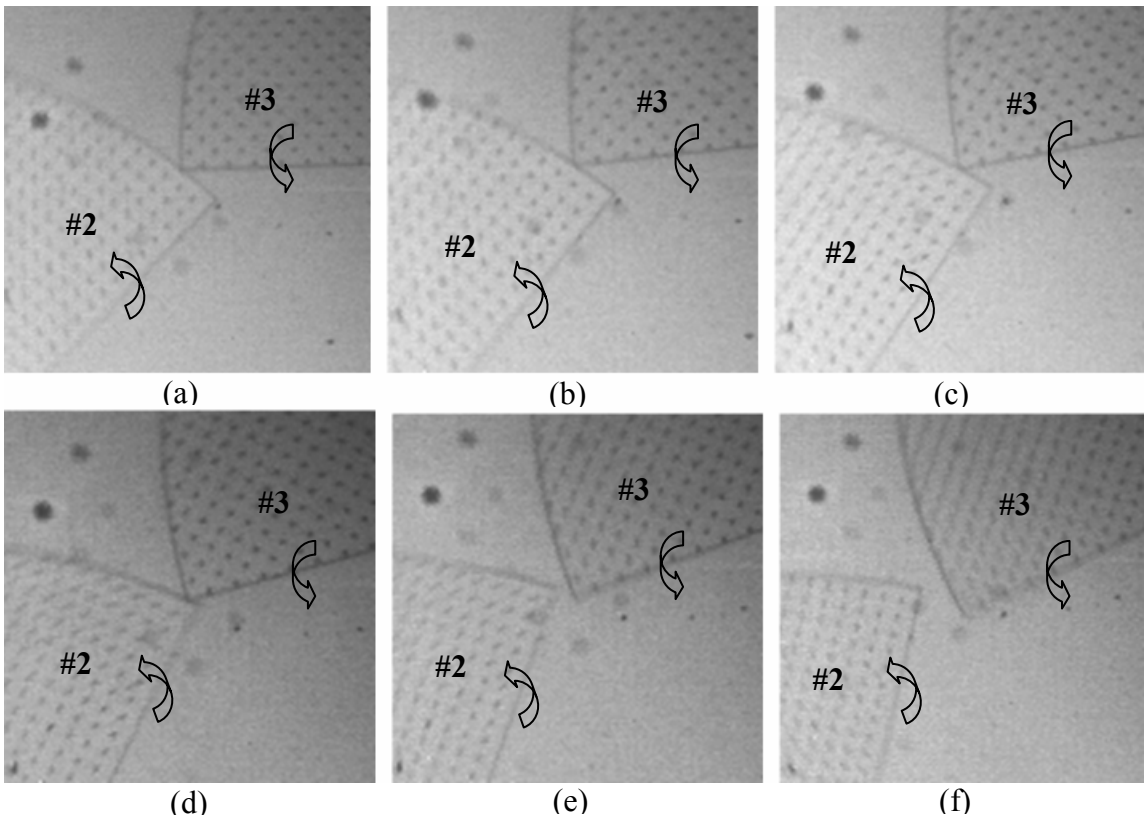

Figure 54 High-speed images of element switching event.

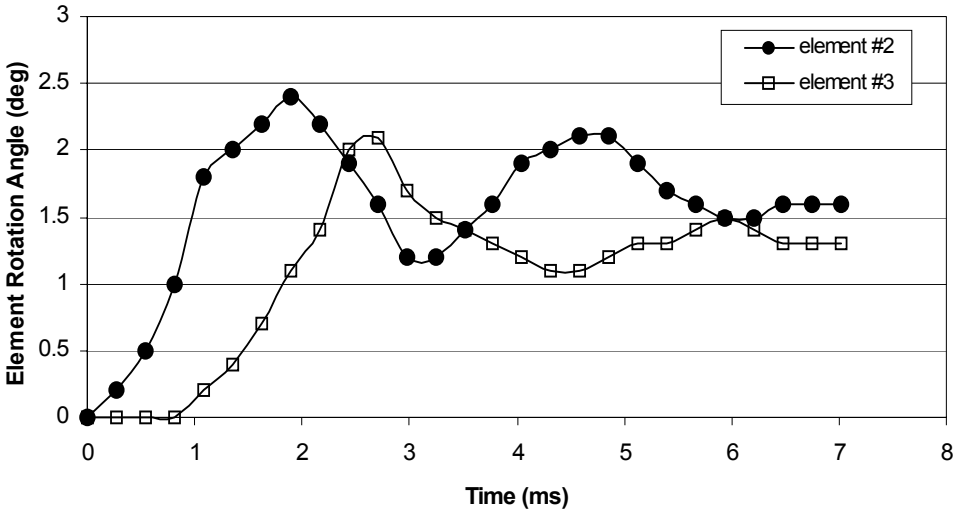

(a)

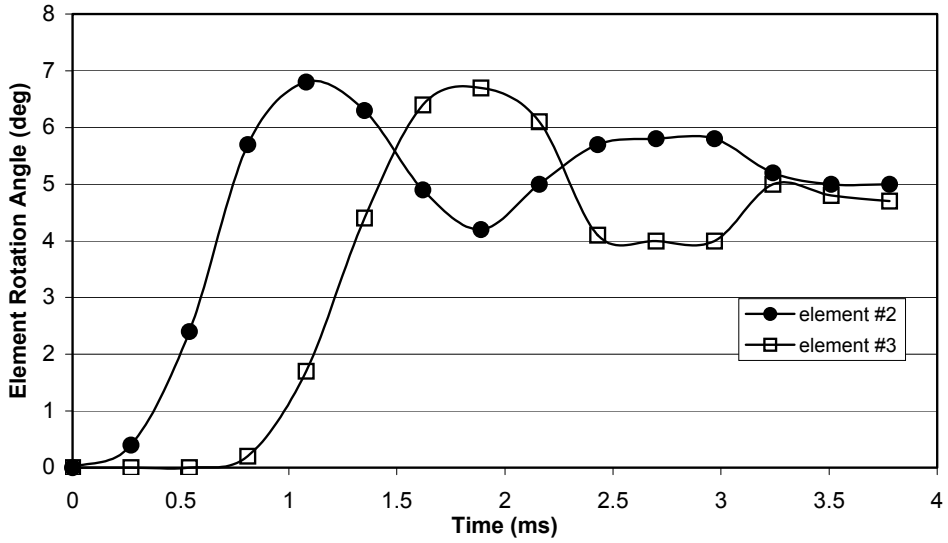

(b)

Figure 55 Experimental switching dynamics measured for (a) low-speed, and (b) high-speed designs.

Repeated tests were conducted on the mechanism designs, with each device tested at least 3 times. Both switching speed and time delay measurements were extracted from the resulting images. Switching speed was found to vary less than 5% between multiple measurements on each design. The delay time variation was within one frame interval for all devices tested. The experimental switching speed measurements are shown in Figure 56, along with the theoretical predictions provided by both dynamics simulations and analytical modeling. Error bars in this plot represent +/-1σ for the experimental data. Theoretical predictions are shown for numerical solutions to the full nonlinear equations of motion, and results of dynamics simulations using ADAMS software. A comparison of experimental and theoretical time delay measurements is shown in Figure 57. This plot also includes the predicted values from the linearized time delay expression given by

equation (2.44). Overall, the experimental results provide reasonable agreement to the nonlinear analytic model and dynamics simulations for all tested designs. For the designs with larger critical angles, the linear analytic model of equation (2.44) predicts delay time to within 1% of the experimental results, suggesting that this simple model is suitable for further design optimization without relying on complex numerical solutions or time consuming dynamics simulations. It should be noted that a relatively good fit between the analytic solutions and experimental results was achieved even though a constant friction coefficient was used to simplify the model.

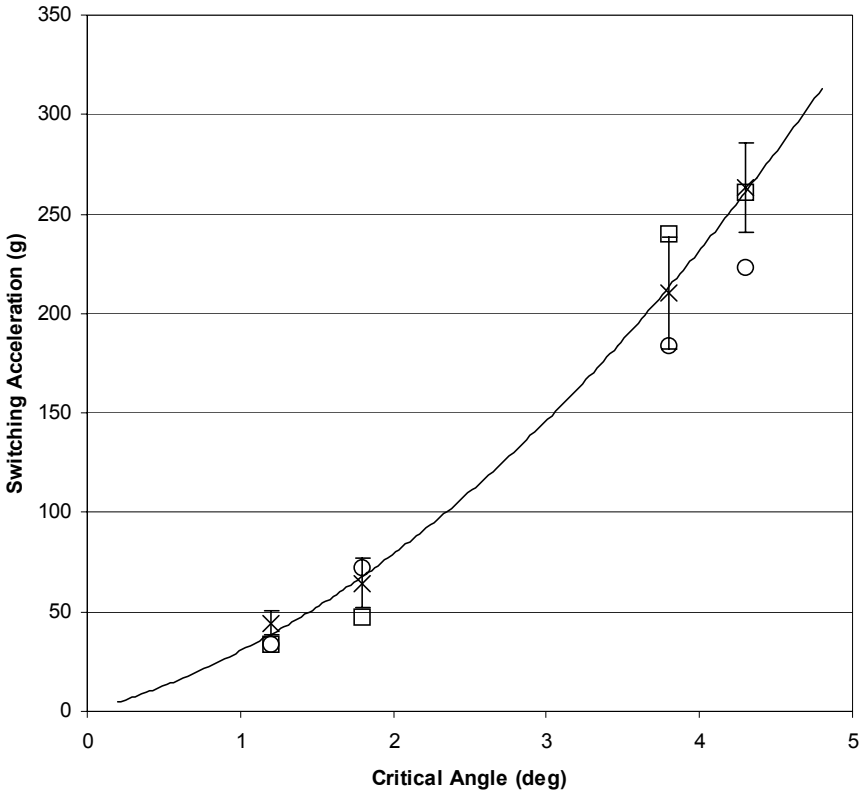

Figure 56 Comparison of experimental (×) switching accelerations with nonlinear numerical (○) and dynamics simulation (□) analyses.

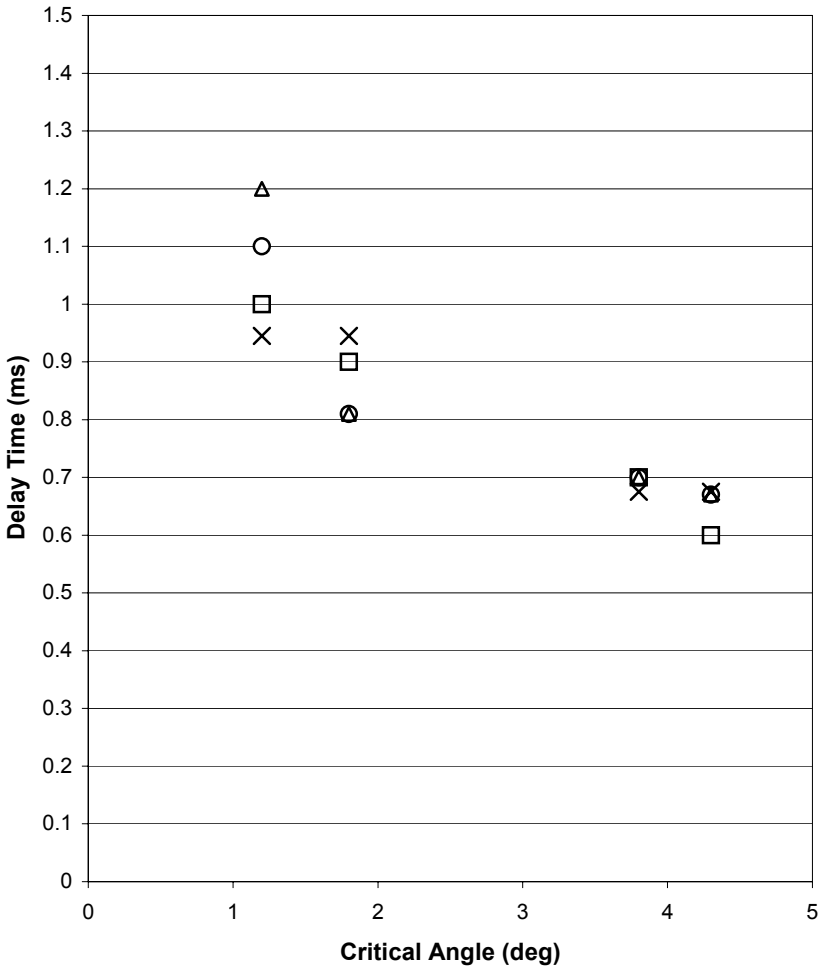

Figure 57 Comparison of experimental (×) delay times with nonlinear numerical (○), linear analytic (Δ), and dynamics simulation (□) analyses.

Chapter 5 –Time Delay Mechanism Optimization and Improvement

In order to improve the delay time of the leaf-type micro time delay mechanism, mechanism scaling, delay time optimization were studied. Attempt was made to couple the runaway escapement mechanism with the leaf-type micro time delay mechanism to increase delay time of each mechanism element. Locking mechanisms were designed to improve reliability of the leaf-type micro time delay mechanism. Mass release mechanism was also designed towards exploring the possibility of triggering other mechanisms in the S&A system after all the elements switched in a leaf-type micro time delay mechanism

5.1 Scaling Effect Study

5.1.1 Scalable Parameters

To explore the relationship between element delay time and element geometry variation, element geometry scaling effect was studied. Geometries of both element inertial mass and element suspension spring were scaled. The device thickness remained unchanged in the scaling effect study. The variable parameters of the element inertial mass include element radius (r), element mass (m_e), and element moment of inertia (I_e). The variable parameters of the element suspension include suspension beam length ($beam\_length$), torsional spring constant (k) and suspension beam moment of inertia (I_e). Suspension beam width can be scaled up. However, scaling down of the beam width was limited by constraints from device fabrication processes.

Parameters that cannot be scaled include material density (density), material Young's modulus (*E*). From equation (2.64), the influence of air damping that was considered will not change with device thickness/beam height (*beam_height*) variation.

Assuming there were no scaling on the device thickness, no scaling down on the beam width and apply scaling factor (*sf*) on the element radius, the element mass, the element moment of inertia, the beam_length, the beam moment of inertia, and the torsional spring constant. The scaling factor was defined as ratio of scaled parameter over original parameter used in the high-speed imaging tests. The above parameters were scaled according to the following rules:

For scaling down:

$$0 < \boldsymbol{sf} < 1 \tag{5.1}$$

For scaling up:

$$\boldsymbol{sf} > 1 \tag{5.2}$$

Element radius:

$$\boldsymbol{r}(\boldsymbol{sf}) = \boldsymbol{r} \times \boldsymbol{sf} \tag{5.3}$$

Element mass:

$$\boldsymbol{m_e}(\boldsymbol{sf}) = \boldsymbol{m_e} \times \boldsymbol{sf}^2 \tag{5.4}$$

Element moment of inertia:

$$\boldsymbol{I_e}(\boldsymbol{sf}) = \boldsymbol{I_e} \times \boldsymbol{sf}^4 \tag{5.5}$$

Beam length:

$$\boldsymbol{beam\_length}(\boldsymbol{sf}) = \boldsymbol{beam\_length} \times \boldsymbol{sf} \tag{5.6}$$

Beam moment of inertia:

$$\boldsymbol{I_{beam}(sf) = I_{beam}} \tag{5.7}$$

Where,

$$\boldsymbol{I_{beam} = \frac{1}{12} beam\_height \times beam\_width^3} \tag{5.8}$$

Different spring designs with different spring constant scaling effects can be used in the time delay mechanism. And, from FEA simulation results on specific straight beam suspension spring, the scaling effect of the spring constant was similar to that of the cantilever suspension spring especially when element rotation angle was small. As a result, cantilever suspension spring constant scaling effect was used in the general scaling effect study:

$$\boldsymbol{k(sf) = k \times sf^{-1}} \tag{5.9}$$

Where,

$$\boldsymbol{k = 2\frac{EI_{beam}}{beam\_length} = \frac{1}{6}\frac{E \times beam\_height \times beam\_width^3}{beam\_length}} \tag{5.10}$$

5.1.2 Scaling Effect Derivation

$$\omega_n = \sqrt{\frac{\omega_c^{\,2} m_e r_c r_e(-\cos\alpha_0) + k}{m_e r_e^{\,2} + I_e}} \tag{5.11}$$

From calculation, k is larger than $\omega_c^{\,2} m_e r_c r_e(-\cos\alpha_0)$. While scaling down, k will be increased by (sf), $\omega_c^{\,2} m_e r_c r_e(-\cos\alpha_0)$ will be decrease by (sf^3). So, ω_n can be approximated as:

$$\omega_n = \sqrt{\frac{k}{m_e r_e^{\,2} + I_e}} \tag{5.12}$$

$$\omega_n(sf) = \sqrt{\frac{k(sf)}{m_e(sf)r_e(sf)^2 + I_e(sf)}} = \sqrt{\frac{k \times sf^{-1}}{(m_e \times sf^2)(r_e \times sf)^2 + (I_e \times sf^4)}} \quad (5.13)$$
$$= \omega_n \times sf^{-\frac{5}{2}}$$

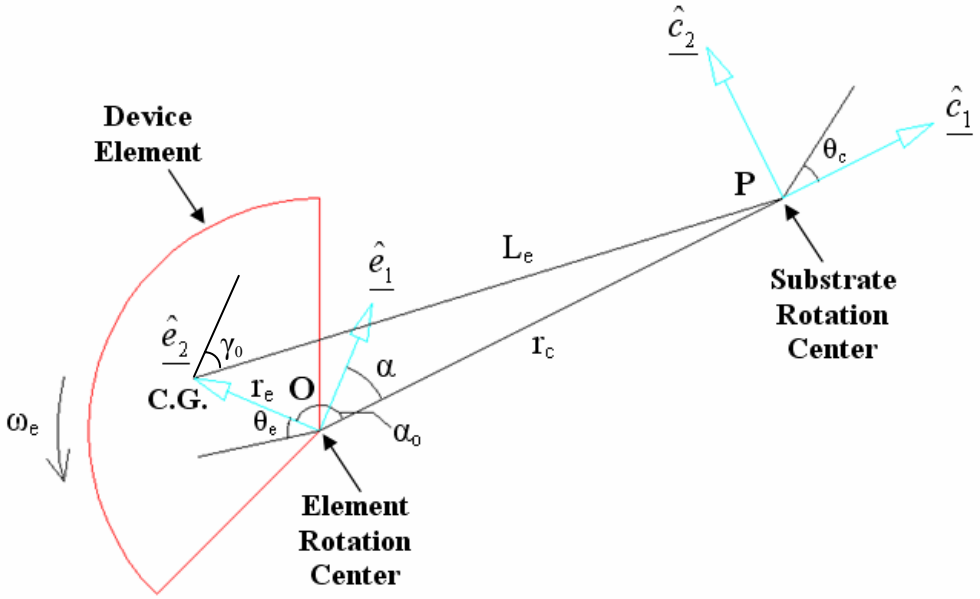

Figure 58 Scaling effect calculation of single mchanism element.

From static analysis, because $L_e >> r_e$, directions and magnitudes of centrifugal force acting on the element center of gravity, $F_{centrifugal}$ and centrifugal force in direction of $\hat{e}_1$, F_{centri_e1} remained the same during device rotation. Angle γ_0 also remains unchanged.

$$F_{centri\_e1} \times r_e = k\theta_{\max} \quad (5.14)$$

$$F_{centrifugal} \cos\gamma_0 \times r_e = k\theta_{\max} \quad (5.15)$$

$$m_e \omega_c^2 L_e \cos\gamma_0 \times r_e = k\theta_{\max} \quad (5.16)$$

$$\theta_{\max} = \frac{\boldsymbol{m}_e \omega_c^{\,2} \boldsymbol{L}_e \cos\gamma_0 \times \boldsymbol{r}_e}{\boldsymbol{k}} \tag{5.17}$$

$$\theta_{\max}(\boldsymbol{sf}) = \frac{\boldsymbol{m}_e(\boldsymbol{sf})\omega_c^{\,2} \boldsymbol{L}_e \cos\gamma_0 \times \boldsymbol{r}_e(\boldsymbol{sf})}{\boldsymbol{k}(\boldsymbol{sf})} \tag{5.18}$$

$$\begin{aligned} \theta_{\max}(\boldsymbol{sf}) &= \frac{(\boldsymbol{m}_e \times \boldsymbol{sf}^2) \times \omega_c^{\,2} \boldsymbol{L}_e \times \cos\gamma_0 \times (\boldsymbol{r}_e \times \boldsymbol{sf})}{\boldsymbol{k} \times \boldsymbol{sf}^{-1}} \\ &= \theta_{\max} \times \boldsymbol{sf}^4 \end{aligned} \tag{5.19}$$

From dynamic model,

$$\theta = \frac{-\omega_c^{\,2} \boldsymbol{m}_e \boldsymbol{r}_c \boldsymbol{r}_e \sin\alpha_0}{-\omega_c^{\,2} \boldsymbol{m}_e \boldsymbol{r}_c \boldsymbol{r}_e \cos\alpha_0 + \boldsymbol{k}} [1 - \cos(\omega_n \boldsymbol{t})] \tag{5.20}$$

$$\theta_{\max} = \frac{-\omega_c^{\,2} \boldsymbol{m}_e \boldsymbol{r}_c \boldsymbol{r}_e \sin\alpha_0}{-\omega_c^{\,2} \boldsymbol{m}_e \boldsymbol{r}_c \boldsymbol{r}_e \cos\alpha_0 + \boldsymbol{k}} \tag{5.21}$$

when

$$\cos(\omega_n \boldsymbol{t}) = 0 \tag{5.22}$$

From calculation, k is larger than $\omega_c^{\,2} \boldsymbol{m}_e \boldsymbol{r}_c \boldsymbol{r}_e (-\cos\alpha_0)$. While scaling down, k will be increased by (sf), $\omega_c^{\,2} \boldsymbol{m}_e \boldsymbol{r}_c \boldsymbol{r}_e (-\cos\alpha_0)$ will be decreased by (sf^3). So, θ_{max} can be approximated as:

$$\theta_{\max} = \frac{-\omega_c^{\,2} \boldsymbol{m}_e \boldsymbol{r}_c \boldsymbol{r}_e \sin\alpha_0}{\boldsymbol{k}} \tag{5.23}$$

$$\begin{aligned} \theta_{\max}(\boldsymbol{sf}) &= \frac{-\omega_c^{\,2} \boldsymbol{m}_e(\boldsymbol{sf}) \boldsymbol{r}_c \boldsymbol{r}_e(\boldsymbol{sf}) \sin\alpha_0}{\boldsymbol{k}(\boldsymbol{sf})} \\ &= \frac{-\omega_c^{\,2} (\boldsymbol{m}_e \times \boldsymbol{sf}^2) \times \boldsymbol{r}_c (\boldsymbol{r}_e \times \boldsymbol{sf}) \sin\alpha_0}{\boldsymbol{k} \times \boldsymbol{sf}^{-1}} \\ &= \theta_{\max} \times \boldsymbol{sf}^4 \end{aligned} \tag{5.24}$$

When $\theta = \theta_{\max}$, $\cos(\omega_n \boldsymbol{t}) = 0$.

$$\omega_n \boldsymbol{t} = \pm\frac{\pi}{2} = \text{constant} \tag{5.25}$$

$$\omega_n(\boldsymbol{sf}) = \omega_n \times \boldsymbol{sf}^{-\frac{5}{2}} \tag{5.26}$$

$$\boldsymbol{t}_{\boldsymbol{delay}}(\boldsymbol{sf}) = \boldsymbol{t}_{\boldsymbol{delay}} \times \boldsymbol{sf}^{\frac{5}{2}} \tag{5.27}$$

The above delay time is the delay time that could be realized from one single mechanism element. While scaling down, more elements are allowed to put in same area. Finally, the total delay time expressions are:

$$\boldsymbol{t}_{\boldsymbol{total\_delay}} = \boldsymbol{t}_{\boldsymbol{delay}} \times \boldsymbol{element\_number} \tag{5.28}$$

$$\begin{aligned} \boldsymbol{t}_{\boldsymbol{total\_delay}}(\boldsymbol{sf}) &= \boldsymbol{t}_{\boldsymbol{delay}}(\boldsymbol{sf}) \times \boldsymbol{element\_number}(\boldsymbol{sf}) \\ &= \boldsymbol{t}_{\boldsymbol{delay}} \times \boldsymbol{sf}^{\frac{5}{2}} \times \boldsymbol{element\_number} \times \boldsymbol{sf}^{-2} \\ &= \boldsymbol{t}_{\boldsymbol{total\_delay}} \times \boldsymbol{sf}^{\frac{1}{2}} \end{aligned} \tag{5.29}$$

Assuming only the element thickness/beam height (*beam_height*) changes with a factor of *sf_h*.

$$\begin{aligned} \omega_n(\boldsymbol{sf\_h}) &= \sqrt{\frac{\omega_c{}^2 \boldsymbol{m}_e(\boldsymbol{sf\_h})\boldsymbol{r}_c\boldsymbol{r}_e(-\cos\alpha_0) + \boldsymbol{k}(\boldsymbol{sf\_h})}{\boldsymbol{m}_e(\boldsymbol{sf\_h})\boldsymbol{r}_e{}^2 + \boldsymbol{I}_e}} \\ &= \sqrt{\frac{\omega_c{}^2 \boldsymbol{m}_e \times \boldsymbol{sf\_h} \times \boldsymbol{r}_c\boldsymbol{r}_e(-\cos\alpha_0) + \boldsymbol{k} \times \boldsymbol{sf\_h}}{\boldsymbol{m}_e \times \boldsymbol{sf\_h} \times \boldsymbol{r}_e{}^2 + \boldsymbol{I}_e}} \\ &= \omega_n \end{aligned} \tag{5.30}$$

$$\begin{aligned} \theta(\boldsymbol{sf\_h}) &= \frac{-\omega_c{}^2 \boldsymbol{m}_e(\boldsymbol{sf\_h})\boldsymbol{r}_c\boldsymbol{r}_e \sin\alpha_0 - \boldsymbol{Q}_{\boldsymbol{friction}}(\boldsymbol{sf\_h})}{\omega_c{}^2 \boldsymbol{m}_e(\boldsymbol{sf\_h})\boldsymbol{r}_c\boldsymbol{r}_e(-\cos\alpha_0) + \boldsymbol{k}(\boldsymbol{sf\_h})}[1-\cos(\omega_n\boldsymbol{t})] \\ &= \frac{-\omega_c{}^2 \boldsymbol{m}_e \times \boldsymbol{sf\_h} \times \boldsymbol{r}_c\boldsymbol{r}_e \sin\alpha_0 - \boldsymbol{Q}_{\boldsymbol{friction}} \times \boldsymbol{sf\_h}}{\omega_c{}^2 \boldsymbol{m}_e \times \boldsymbol{sf\_h} \times \boldsymbol{r}_c\boldsymbol{r}_e(-\cos\alpha_0) + \boldsymbol{k} \times \boldsymbol{sf\_h}}[1-\cos(\omega_n\boldsymbol{t})] \\ &= \theta \end{aligned} \tag{5.31}$$

$$\begin{aligned} \boldsymbol{t}_{arm}(\boldsymbol{sf\_h}) &= \frac{1}{\omega_n}\cos^{-1}\{1+\frac{[\omega_c{}^2\boldsymbol{m}_e(\boldsymbol{sf\_h})\boldsymbol{r}_c\boldsymbol{r}_e(-\cos\alpha_0)+\boldsymbol{k}(\boldsymbol{sf\_h})]\theta_{arm}}{\omega_c{}^2\boldsymbol{m}_e(\boldsymbol{sf\_h})\boldsymbol{r}_c\boldsymbol{r}_e\sin\alpha_0+\boldsymbol{Q}_{friction}(\boldsymbol{sf\_h})}\} \\ &= \frac{1}{\omega_n}\cos^{-1}[1+\frac{(\omega_c{}^2\boldsymbol{m}_e\times\boldsymbol{sf\_h}\times\boldsymbol{r}_c\boldsymbol{r}_e(-\cos\alpha_0)+\boldsymbol{k}\times\boldsymbol{sf\_h})\theta_{arm}}{\omega_c{}^2\boldsymbol{m}_e\times\boldsymbol{sf\_h}\times\boldsymbol{r}_c\boldsymbol{r}_e\sin\alpha_0+\boldsymbol{Q}_{friction}\times\boldsymbol{sf\_h}}] \\ &= \boldsymbol{t}_{arm} \end{aligned} \quad (5.32)$$

It could be seen that changing element thickness/beam height (*beam_height*) does not contribute to delay time change.

5.1.3 Scaling Effect Summary

From the above derivation, scaling down device geometry led to natural resonant frequency increase, total delay time decrease, amd maximum element vibration angle decrease.

$$\begin{aligned} \omega_n(\boldsymbol{sf}) &= \omega_n(1)\times\boldsymbol{sf}^{-\frac{5}{2}} \\ \theta_{\max}(\boldsymbol{sf}) &= \theta_{\max}(1)\times\boldsymbol{sf}^{4} \\ \boldsymbol{t}_{total\_delay}(\boldsymbol{sf}) &= \boldsymbol{t}_{delay}(1)\times\boldsymbol{sf}^{\frac{1}{2}} \end{aligned} \quad (5.33)$$

Concluded from the above results, time delay will not be increased by scaling down the element dimension.

Device thickness variation has no influence on changing time delay properties. It will be determined by trade off between satisfying requirement on anti off plane force and process limitations. The larger the device thickness, the better the device could withstand off plane force. The smaller the device thickness, the finer feature that could be realized in photolithography and DRIE processes.

5.2 Delay Time Optimization

Starting from a specific design, the following figures give the variations of element delay time and maximum element rotation angles with respect to changes of the element mass and the element torsional spring constant under both low (20 g) and high (2,000 g) centrifugal acceleration using the non-linear analytic model developed in chapter 2. In addition, the mass change in thickness direction and in plane were considered separately. Note in the figures, the x and y axes are expressed in logarithm (base 10). The "steps" that make the delay time figures not smooth come from selection of calculation step size in the numerical calculations. Smaller step size will result in smoother surfaces.

Generally, both the delay time and the maximum rotation angle increase when element mass and torsional spring constant decrease. Higher centrifugal acceleration will give shorter delay time and larger maximum rotation angle. It could also seen that with same spring constant, mass variation in thickness direction is less effective as mass variation within device plane in order to increase delay time. Reducing spring constant of the suspension spring will increase element delay time.

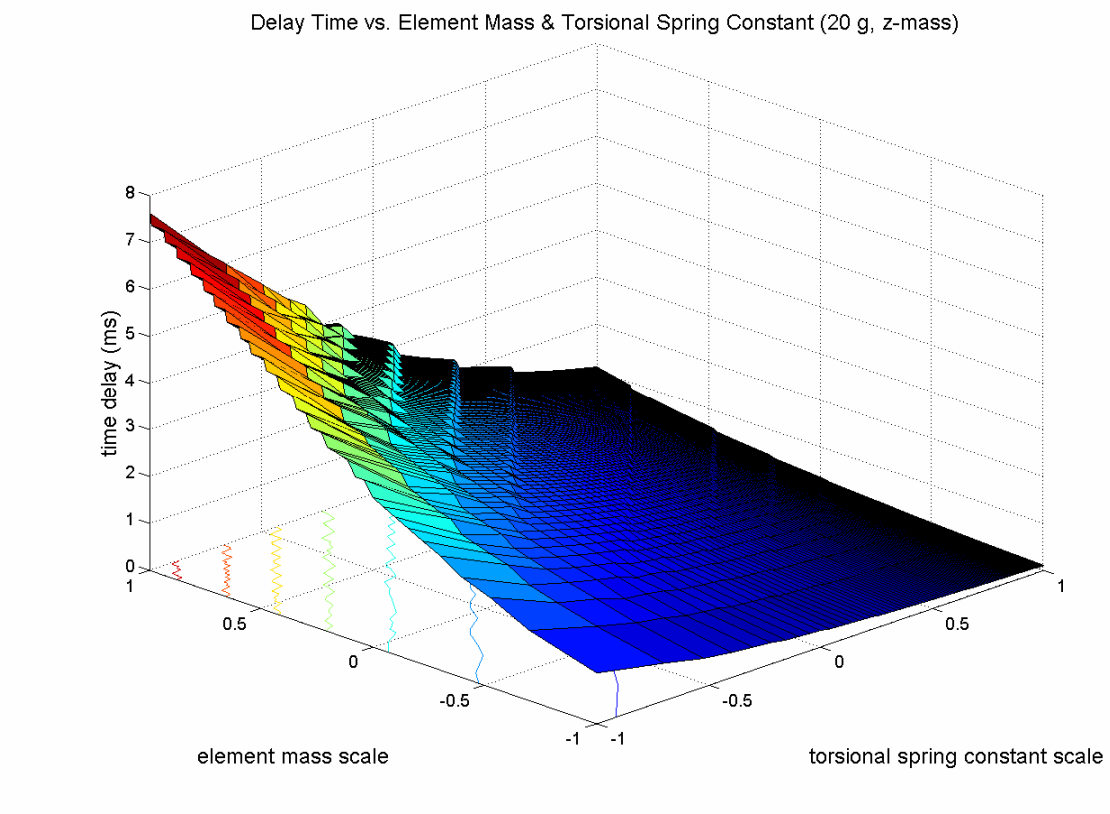

Figure 59 Delay time vs. mass (thickness) and spring constant variations (20 g).

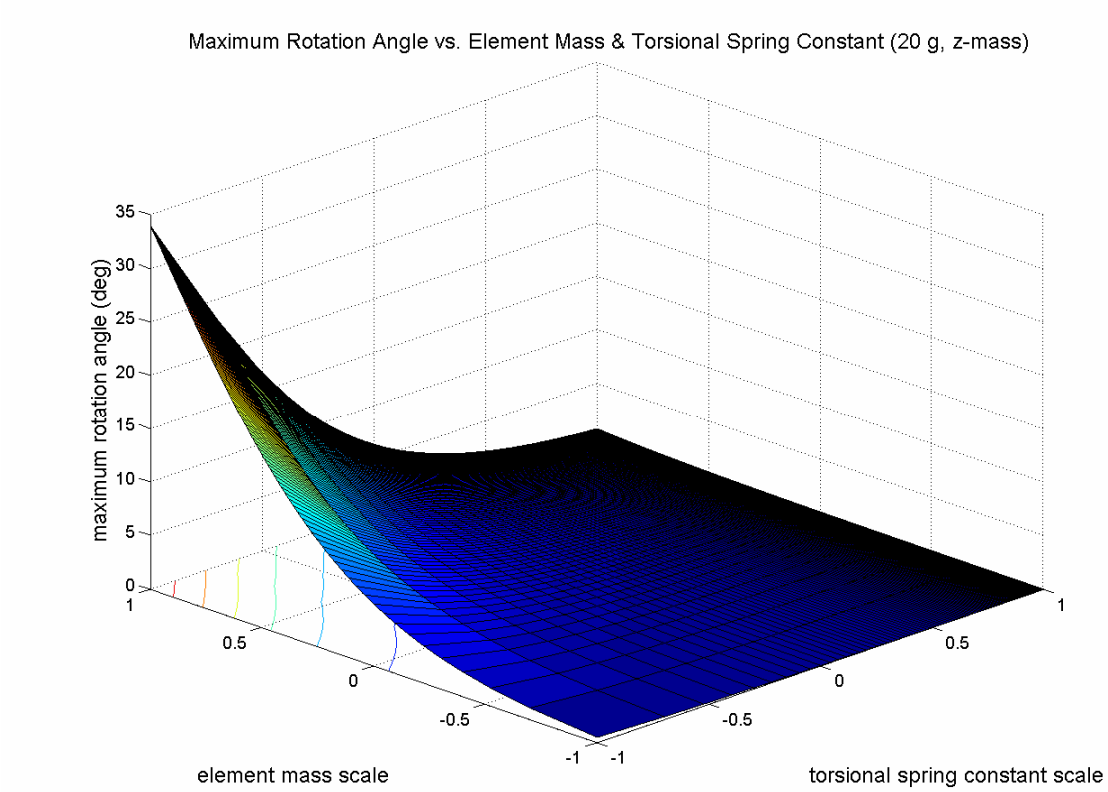

Figure 60 Maximum rotation angle vs. mass (thickness) and spring constant variations (20 g).

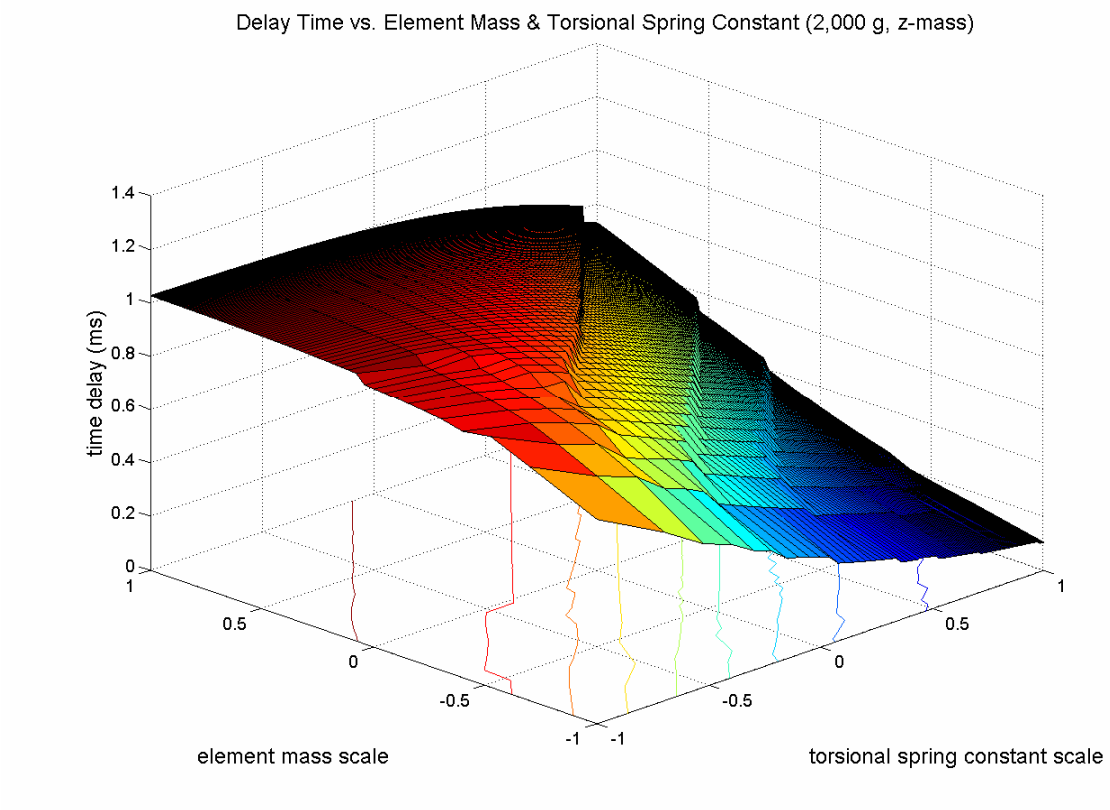

Figure 61 Delay time vs. mass (thickness) and spring constant variations (2,000 g).

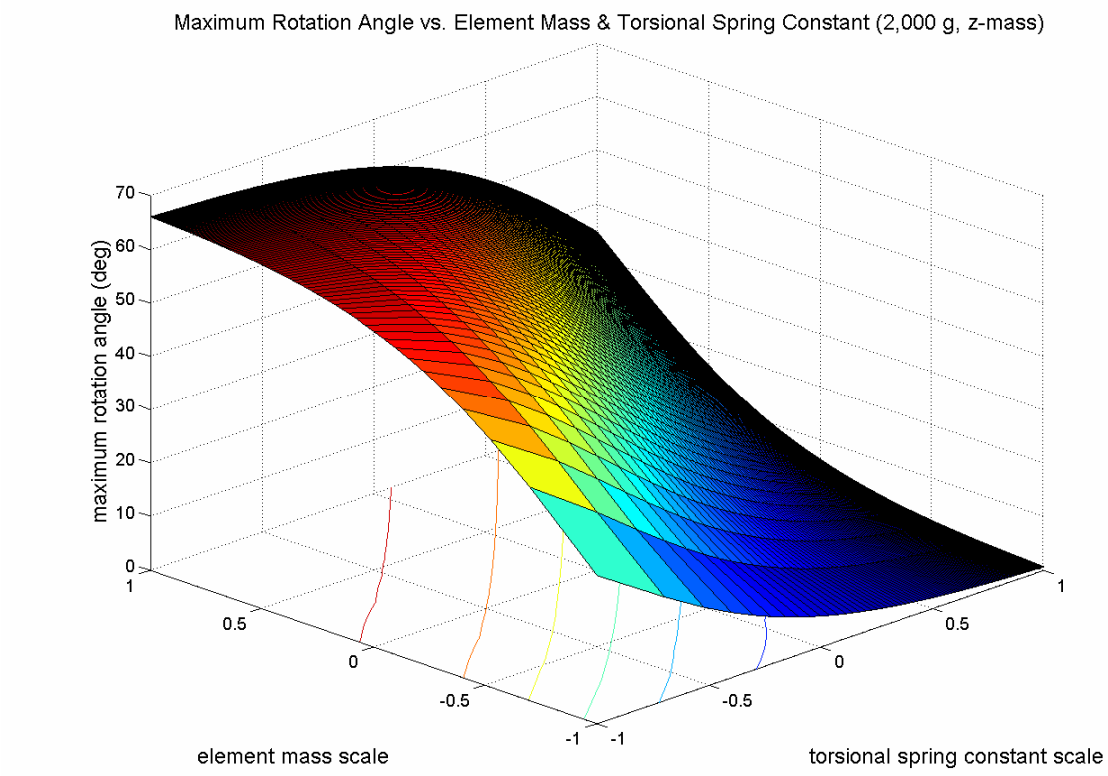

Figure 62 Maximum rotation angle vs. mass (thickness) and spring constant variation (2,000 g).

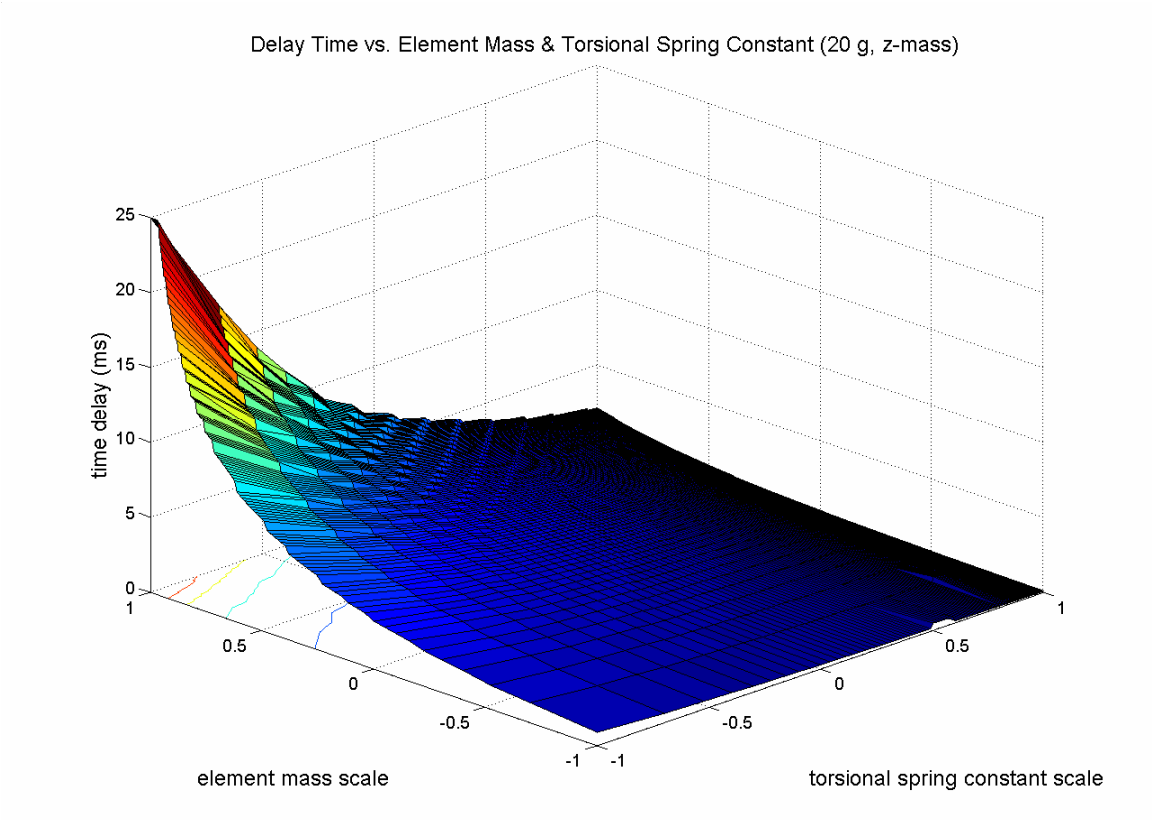

Figure 63 Delay time vs. mass (in plane) and spring constant variations (20 g).

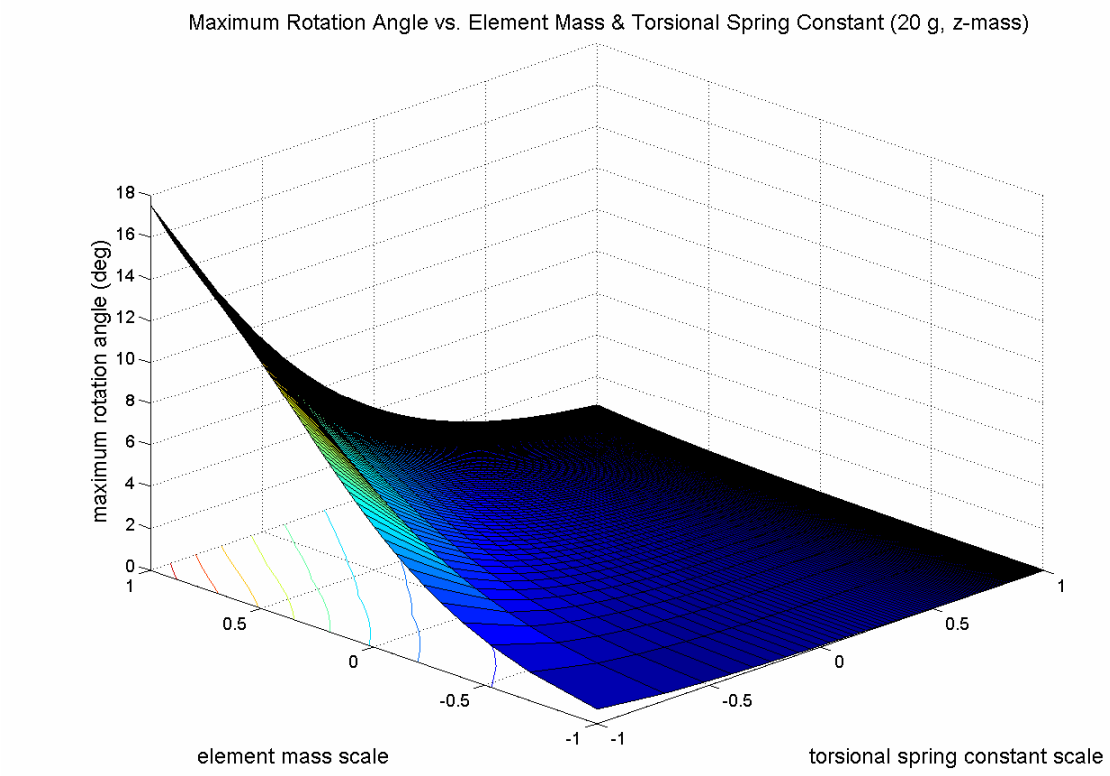

Figure 64 Maximum rotation angle vs. mass (in plane) and spring constant variations (20 g).

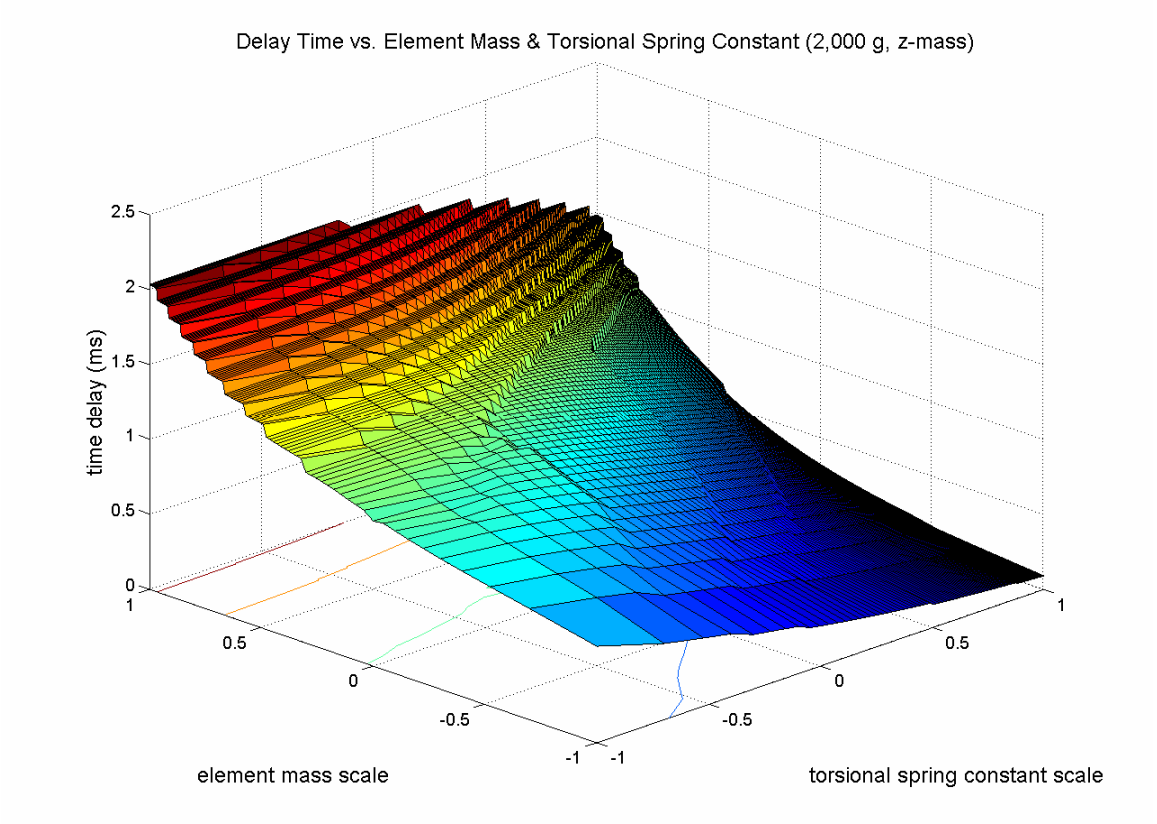

Figure 65 Delay time vs. mass (in plane) and spring constant variations (2,000 g).

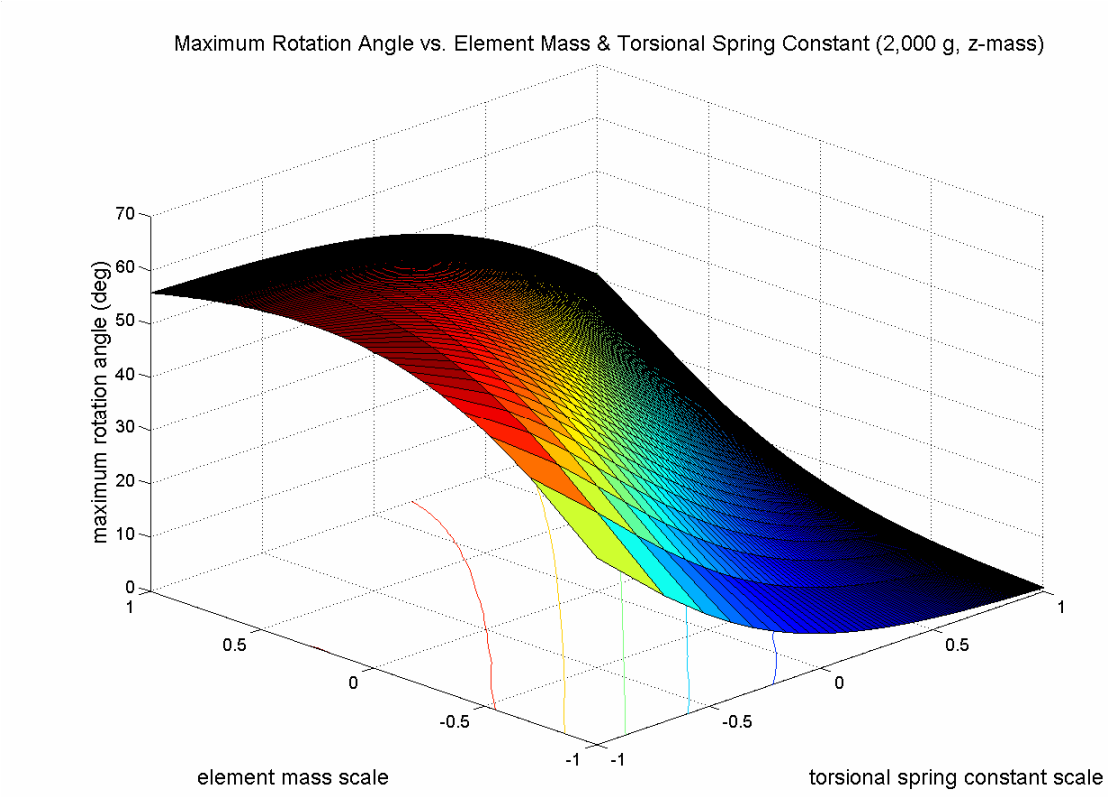

Figure 66 Maximum rotation angle vs. mass (in plane) and spring constant variations (2,000 g).

5.3 Introduce Escapement Design to Increase Delay Time

One way of increasing the delay time of the micro sequential leaf time delay mechanism is to combine different escapement designs along with the current mechanism design. As shown in Figure 67, a runaway escapement mechanism is coupled with the leaf time delay mechanism element to increase the delay time of that single mechanism element. The normal runaway escapement typically includes a gear train and an escapement pallet. The escapement pallet is used to escape energy from the gear train. In the combined mechanism design, the boundary of the leaf element was modified by

adding teeth along its boundary. An escapement pallet that matches those teeth is arranged beside the leaf element. When the element rotates, the escapement pallet interacts with the element teeth and dissipates energy from the leaf element. Through this way, the delay time of a single leaf element is increased.

Dynamic simulations using ADAMS have been done to determine the delay time improvement based on the combined delay mechanism design. A two-element time delay mechanism with the second element modified to form a runaway escapement was used in the simulation. The escapement teeth were distributed evenly along the element boundary, with 7.5^{o} separation between adjacent teeth. The tooth separation angle was small compared to normal runaway escapement design. Larger teeth separation angle gave longer delay time. However, the selection of separation angle between adjacent teeth was constraint by the maximum angle the second element was allowed to rotate, which was determined by the element suspension spring design and magnitude of centrifugal acceleration. Based on the four straight beam suspension spring design, the element rotation angle under 2,000 g centrifugal acceleration was approximately 18^{o}. The 7.5^{o} separation angle was selected to allow the escapement pallet of the runaway escapement to vibrate for two cycles. As shown in Figure 67, the escapement pallet was a star shaped pallet. Its center of mass overlaps with its center of rotation, where a torsional three straight beam suspension spring was added. Its spring constant was ¾ of that of the four straight beam suspension spring.

Comparison simulation was done on both a two-element time delay mechanism without runaway escapement design and on the two-element time delay mechanism with runaway escapement design. Both mechanisms were accelerated linearly from 0 g to

2,000 g in 15 ms, which simulated the target mechanism working environment. The switching curves of the second elements of the above mechanisms were compared to figure out the delay time variation on the caused by combining the runaway escapement mechanism design. It was noticed from the simulation results that the mechanism elements deflected clockwise with large magnitude at the beginning of the acceleration procedure due to the high acceleration from the element carrier. Because the entire acceleration procedure was as short as 15 ms, the above mechanism vibration could not be damped out before the switching event happened. To prevent this vibration behavior from happening, movement stoppers were anchored on the element carrier beside elements to constrain them from moving clockwise from their initial positions. After the movement stoppers were introduced in the simulation, the counter clockwise angular deflection of the first element was postponed compared to that of the element working under the low centrifugal acceleration environment. This phenomenon happened because the element carrier was accelerated to rotate directly. The centrifugal acceleration of the element was provided by the movement stopper. At the beginning of the acceleration procedure, essential amount of the centrifugal acceleration of the element about element rotation center was provided by the movement stopper. Only when the element carrier rotation speed increased to certain value that could provide element with enough centrifugal acceleration, did the element begin to deflect obviously. As a result, the counter clockwise deflection of the first element was postponed compared to that of the element working under low axial acceleration environment.

The delay time curves of the second elements without runaway escapement design and that with runaway escapement design were shown in Figure 68. The two

interactions and matching cycles between the escapement pallet and the leaf element could be identified by referring to two small peaks on element deflection. As could be observed in the figure, the times that element rotation angles of the two mechanisms start to increase from zero vary a little, which is the result of contact friction change between adjacent elements. The element delay time can be read from the figure by finding time that the element rotation angle starts to increase from zero degree and time that the element rotation angles reaches 15^{o}. For elements without and with escapement mechanism, these times are from 0.0172 s to 0.0175 s and from 0.0171 s to 0.0176 s respectively, which indicates that the delay times of the elements are 0.3 ms to 0.6 ms respectively. Adding the escapement mechanism with current sequential leaf time delay mechanism contributes to increase the delay time by twice in this specific design.

Based on the results from this specific design, the delay time can be further increased by increasing the mass of the escapement pallet, increasing the maximum rotation angle of the escapement pallet. Besides the runaway escapement currently considered, other types of escapement designs could also be used to further increase the delay time. To benefit from delay time increase of every time delay element, the geometry tolerances of the elements will be increased to adapt to the matching requirement between contact profiles.

Although adding escapement mechanism to the current sequential leaf time delay mechanism can increase its time delay, the element rotation angle necessary for the escapement mechanism to work is approximately 15^{o}, which can be realized when the centrifugal acceleration of the munition reaches 2,000 g with the current four straight beam suspension spring design. However, such high-g testing environment is not

available at this time.

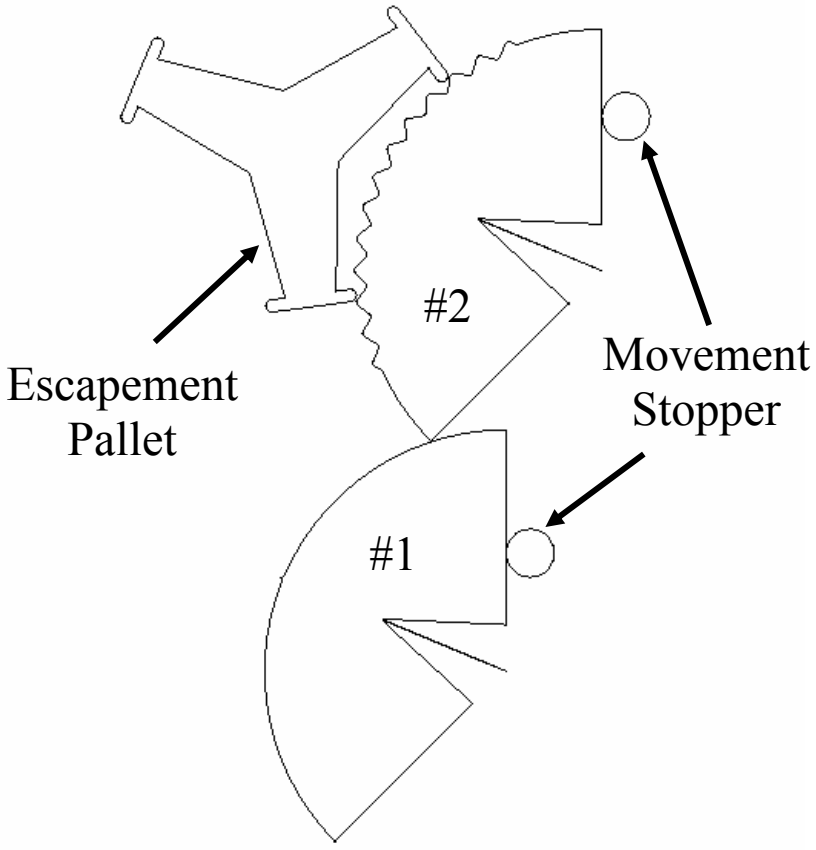

Figure 67 Combined mechanism of sequential leaf mechanism and runaway escapement.

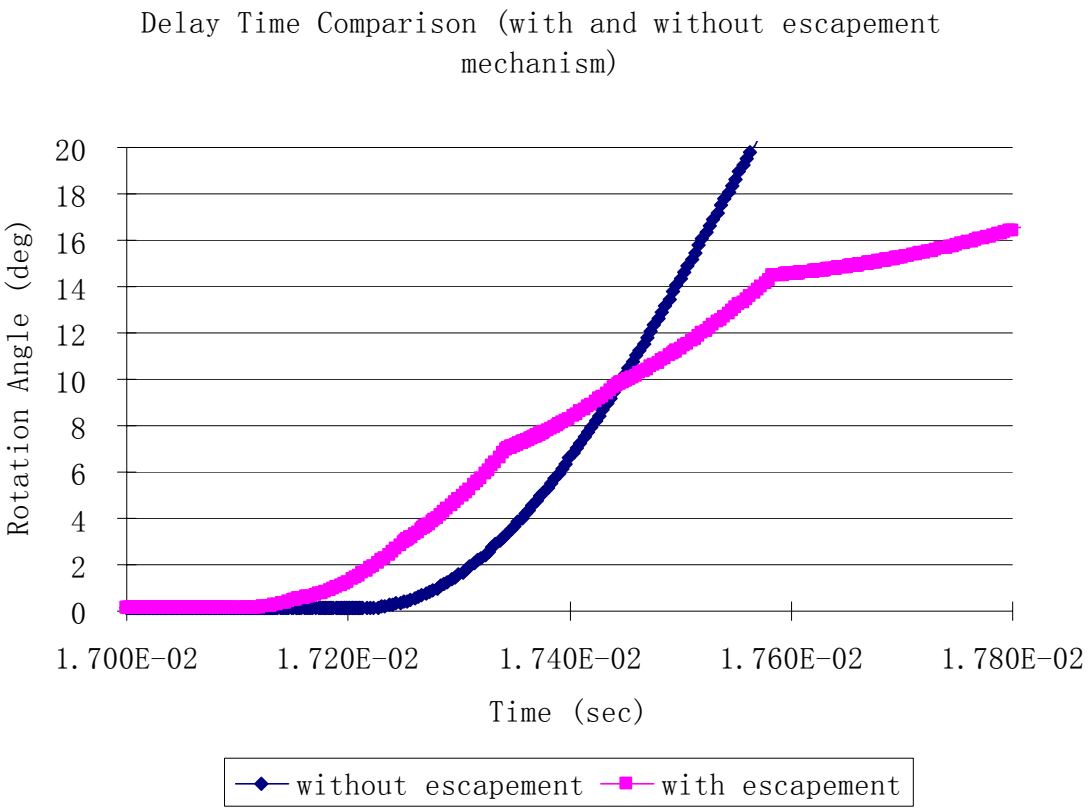

Figure 68 Switching dynamics comparison.

5.4 Locking Mechanism Design

During and after the switching event, the elements of the micro time delay mechanism vibrate and may impact with each other, what may interference the element switching dynamics. However, in the S&A system application, the reliability issue is of high priority. The mechanism vibration and impact need to be controlled to make element switching as reliable as possible. Two types of element locking mechanisms have been designed, fabricated, and tested to solve this problem.

One type of the element locking mechanisms is fish-bone shaped ratchet mechanism shown in Figure 69. In the design, a ratchet bar extends from edge of the

element like a cantilever beam. A no-back pawl pair was arranged symmetrically on both sides of a locking slot. The head of the ratchet bar is sharp, which makes it easy to go forward passing through the no-back pawl pair. Tooth pairs were distributed symmetrically on both sides of the ratchet bar. During the element switching event, the ratchet bar goes toward the no-back pawls. When the front sides of the ratchet bar teeth contact with the no-back pawls, the compliant no-back pawls bend and allow the ratchet bar teeth to pass through. When the ratchet bar tries to go backward, however, the backside of the ratchet bar teeth will contact and interact with the no-back pawls. Tips of the no-back pawls will slide toward to roots of the ratchet bar and lock it, which prevents it from moving backward. As a result, the ratchet bar is only allowed to move forward and will be locked at the farthest forward position as shown in Figure 70, which was taken after the switching event.

In a three-element micro time delay mechanism, ratchet mechanism is built on the third element. From experiments, typical relations between element rotation angles and time of element #2 and element #3 are plotted in Figure 71. Compared with Figure 55 of the relationships of three-element mechanism without ratchet mechanism, it could be seen that the angular position of the element #3 did not change once it reached maximum value, i.e. locked. The no-back pawls were anchored on the device substrate. Upon mechanism switching, the front sides of the no-back pawls provided resistance to the element #3 from moving forward, which reduced the vibration magnitude of the element #3. The backsides of the no-back pawls prevented the element #3 from moving backward. Seen from Figure 70, the no-back pawls bent towards the ratchet bar. After the switching event, the rotation angle of the element #3 remained unchanged at 3.8° after it was locked

by the no-back pawls. Since there was no locking mechanism with the element #2, its angular vibration was similar to that in a three-element mechanism without ratchet mechanism.

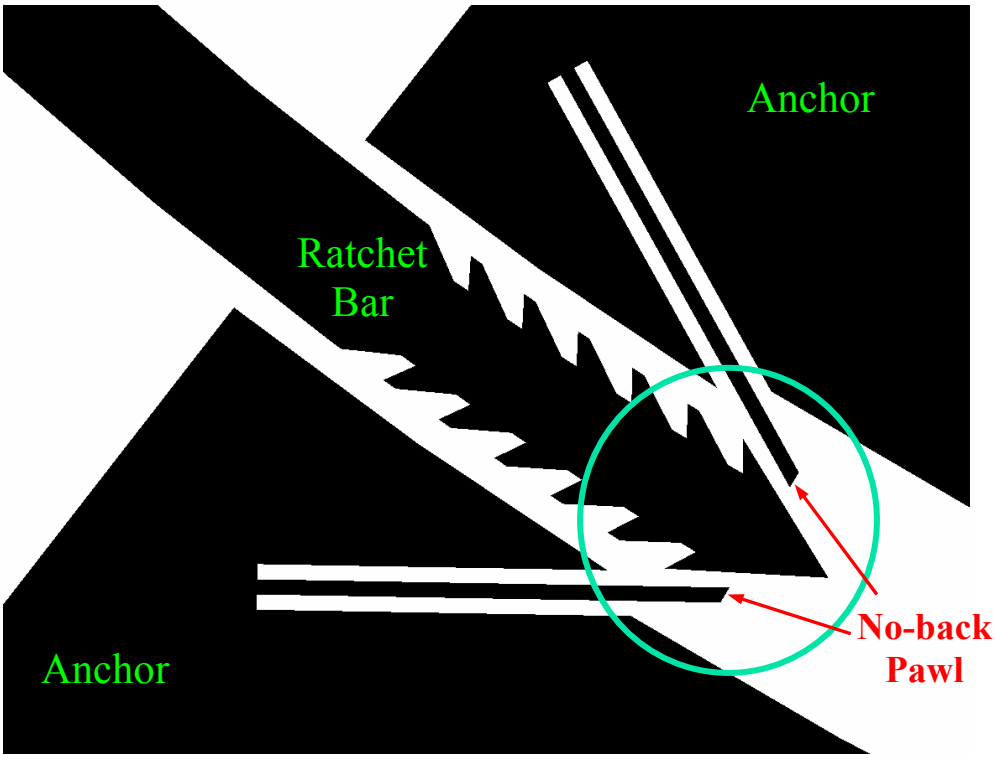

Figure 69 Schematic of locking mechanism design (1).

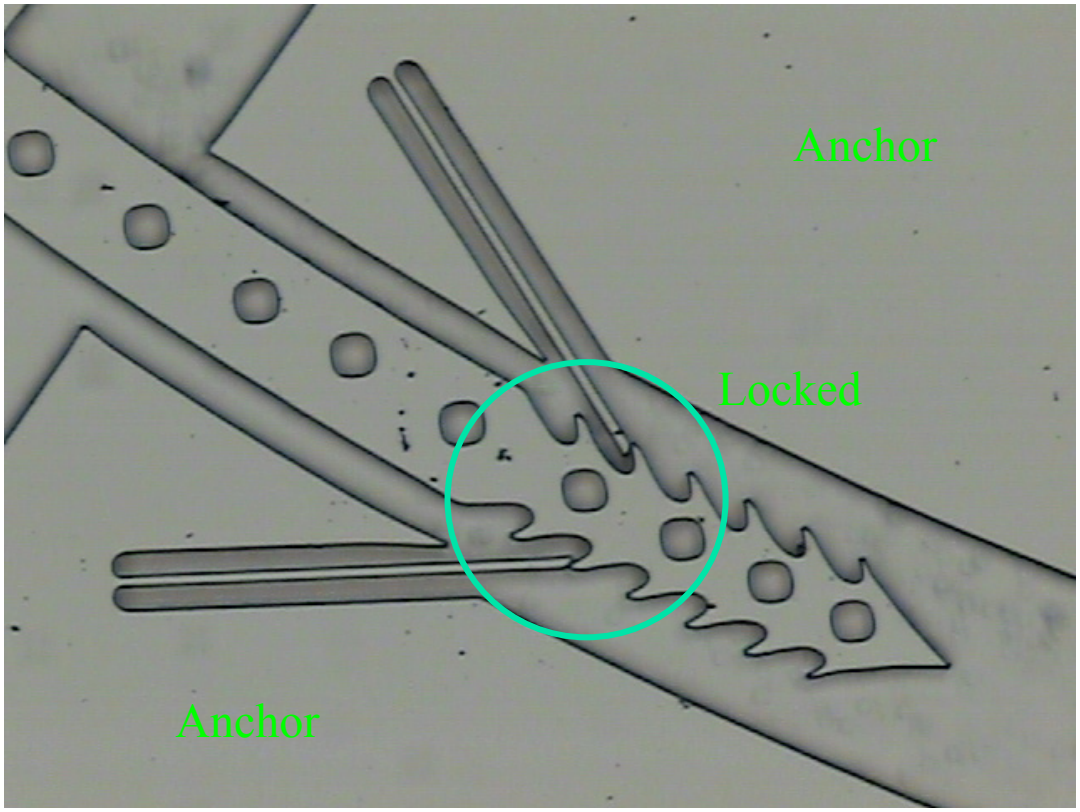

Figure 70 Locked mechanism (1).

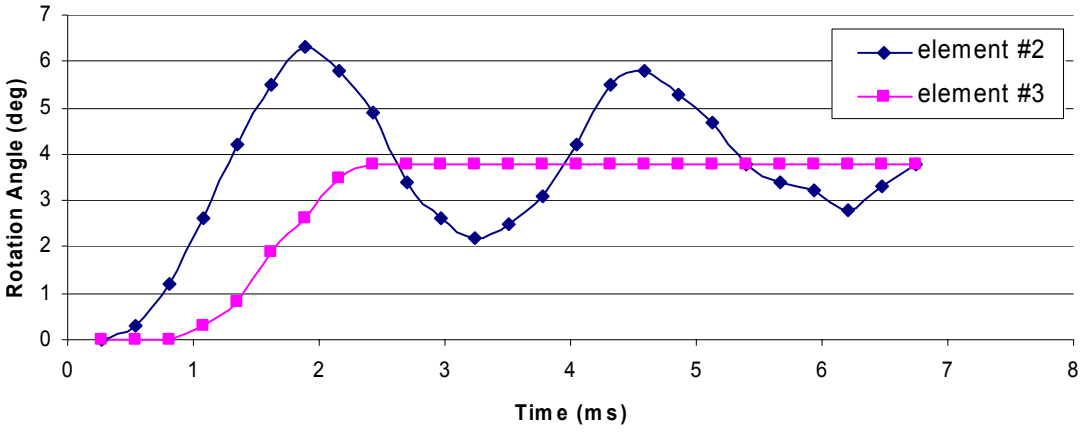

Figure 71 Element rotation angle vs. time.

Another type of the element locking mechanism that has been tested is the

cantilever type ratchet mechanism as shown in Figure 72. In this design, a hook extends from the element through a cantilever beam. No-back pawls are distributed on one side of a locking slot. When the element tries to rotate forward, the front surface of the hook will contact with the front sides of the no-back pawls. The 5μm wide narrow cantilever is easy to deflect and allows the hook to pass through the no-back pawls while moving forward. When the element tries to go backward, the backside of the hook will contact with the backsides of the no-back pawls and will be stopped.

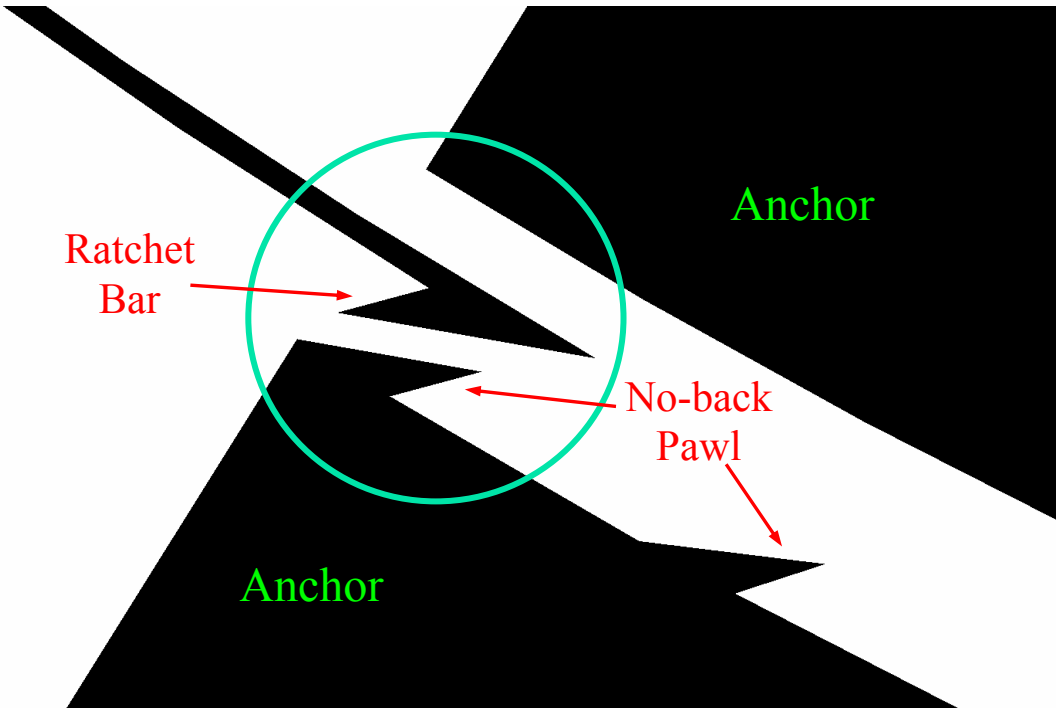

Figure 72 Schematic of locking mechanism design (2).

Spinning experiments were conducted on three-element micro time delay mechanisms with cantilever type locking mechanisms built on the third elements. From the videos taken by high-speed camera, the ratchet hook moved forward and passed beyond the no-back pawls during the element switching event. However, in some of the pictures taken right after the spinning tests, the ratchet hook were observed going backward and passed the first no-back pawl as shown in Figure 73, which indicated that the locking mechanism did not function properly.

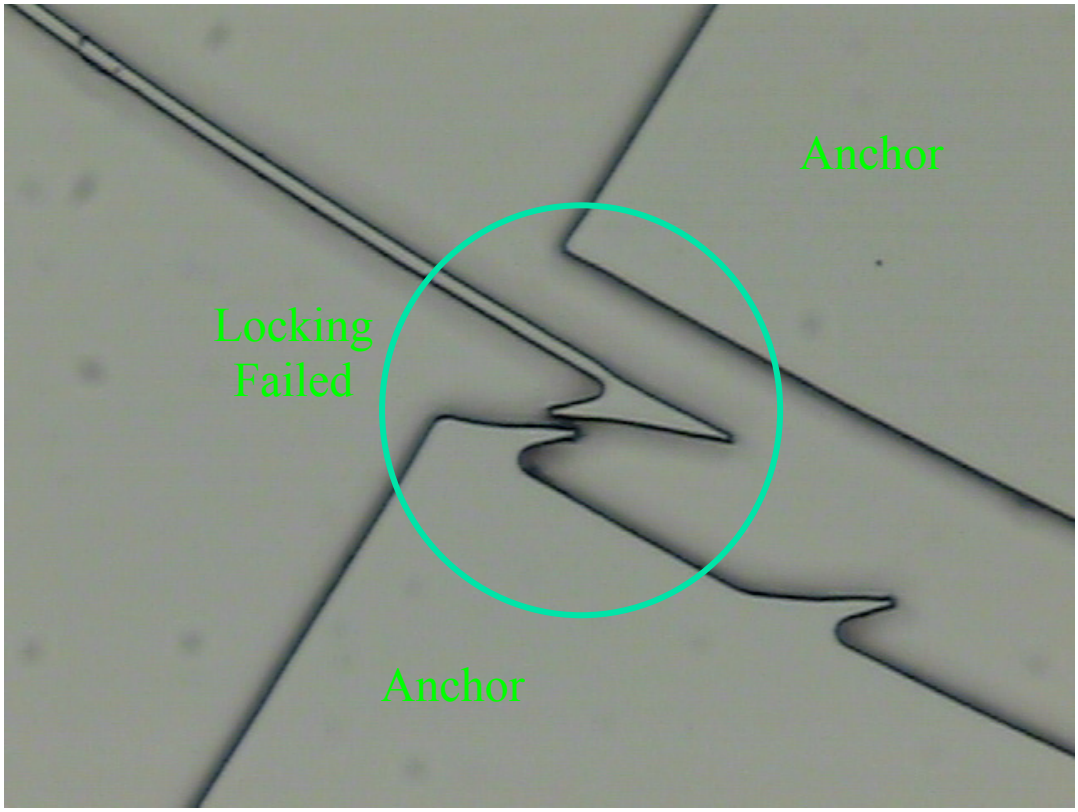

Figure 73 Failed locking mechanism (2).

This locking failure came from that the no-back pawls were only distributed along one side of the locking slot. There was space for the cantilever beam to deform in the direction away from the no-back pawls, which made it possible for the locking hook to miss the no-back pawls when moving backward. The long and narrow hook cantilever made it easy to vibrate and thus increased the possibility for the ratchet hook to miss the no-back pawls when moving backward.

Experiments were repeated for twice for both of the fish-bone shaped and the cantilever type locking mechanism designs. The dimensions of the locking mechanism were small, with typical dimension of 5 μm, It is not possible to unlock the locking mechanisms with probes after the switching tests. New device was used in each test.

From the experiments, all the fish-bone type locking mechanism worked successfully, one of the cantilever type locking mechanism worked successfully, the other one failed to lock.

The fish-bone shaped ratchet mechanism functions as element locking mechanism successfully and can be used in the micro time delay mechanism to increase mechanism switching reliability. The locking mechanism was designed to work after the element rotated passing the critical angle. So, the influence of introducing the locking mechanism to the element switching can be ignored. On the other hand, the locking mechanism prevents the switched element from vibrating backward and bumping with the next element. The influence to the delay time of the following element is reduced. More generally, the locking mechanism suggests the possibility of using more frictional elements to increase delay time of the locked time delay element.

5.5 Mass Release Mechanism Design

Attempt was made towards exploring the possibility of triggering other mechanisms in the S&A system after all the elements switched in a leaf-type micro time delay mechanism. In the attempt, the second element of a two-element mechanism was designed to release a big inertial mass after it was allowed to rotate.

As shown in Figure 74, the inertial mass was suspended by folded springs on two opposite sides. Motion of the inertial mass was constrained and guided on the other two sides by fixed square anchors. The movement of the inertial mass towards the right direction was constrained by interaction between pins on the inertial mass and the square

anchors. As a result of the above constraints, the inertial mass was only allowed to move in the left direction. Small pins were designed on the sides of the two square anchors that interacted with the inertial mass to reduce friction between them. The movement of the inertial mass in the left direction was constrained at its left-down corner by the second element of the two-element time delay mechanism. When the second element started to rotate, the inertial mass moved to the left under the action of centrifugal force.

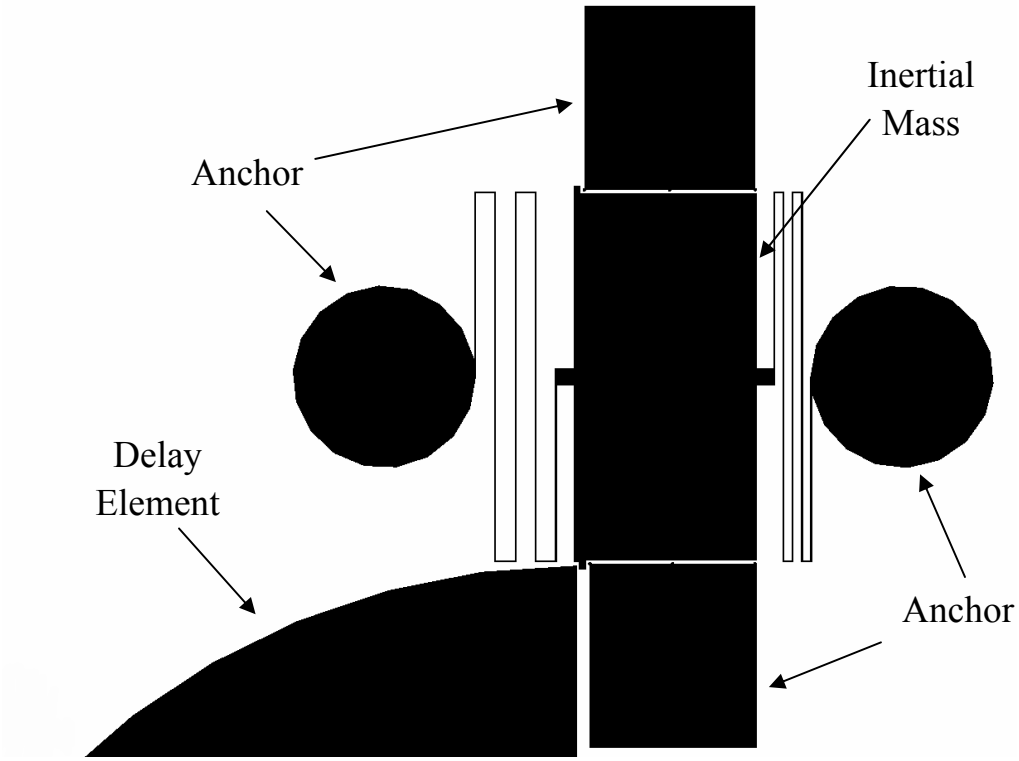

Figure 74 Schematic of mass releasing mechanism.

In the spinning tests, the movement of the suspended inertial mass was monitored using high-speed camera. The following two pictures, Figure 75 and Figure 76, recorded the initial position and the maximum displacement of the inertial mass after the element

was allowed to rotate. As shown in Figure 76, the folded spring on one side of the inertial mass was extended, and the one on the other side was compressed.

The demonstration of releasing inertial mass was to try to provide the possibility of initiating other mechanism, for example, electrical switch after certain delay time was realized by the leaf-type time delay mechanism. Further explorations need to be conducted in achieving this micro-macro interfacing function.

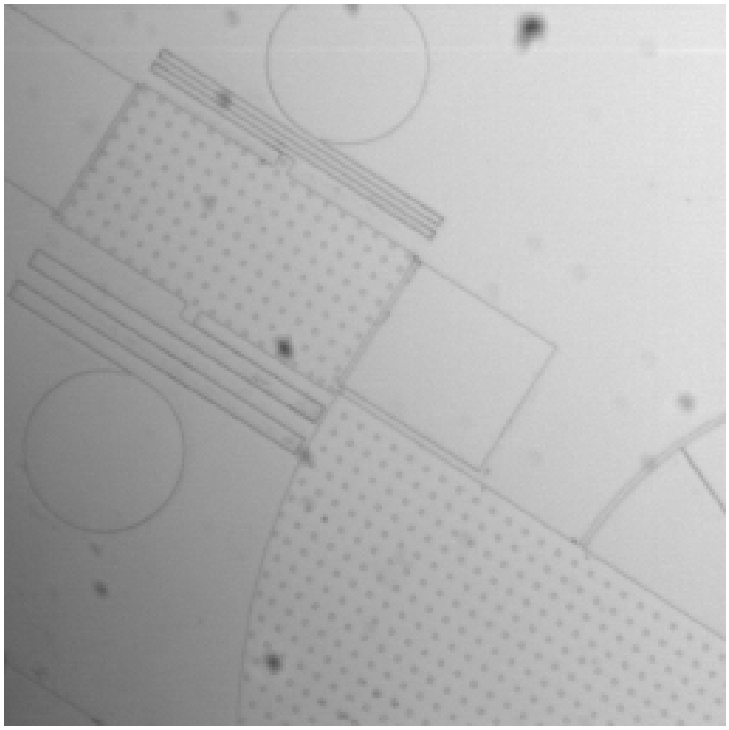

Figure 75 Initial state of inertial mass.

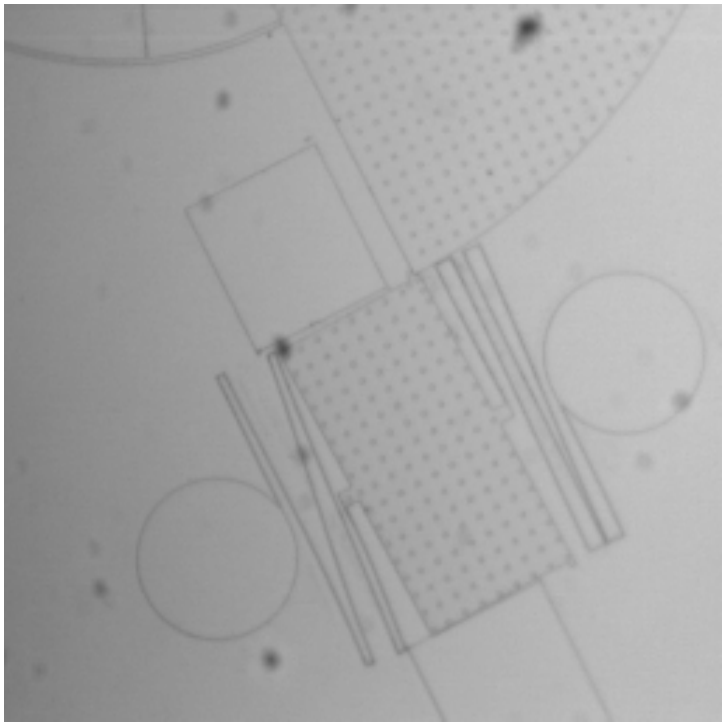

Figure 76 Maximum displaced position of inertial mass.

Chapter 6 – SOI/DRIE Based All-fiber Optical Switching

6.1 Introduction

Based on the mass releasing mechanism, a novel all-fiber optical switching mechanism was developed that provides the possibility of closing an optical route after the last element of the leaf time delay mechanism switches. The all-fiber optical switching mechanism can also be used independently for optical switching.

The all-fiber optical switch was developed based on the same SOI/DRIE technology as the leaf-type time delay mechanism so that it could be integrated with the current micro time delay mechanism design.

6.2 Design and Fabrication

6.2.1 Design and Fabrication Issues

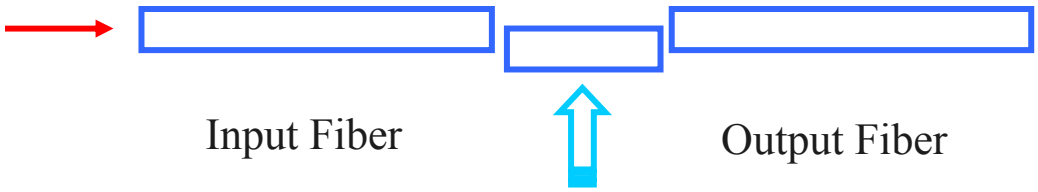

(a) Nonactuated / off state.

(b) Actuated / on state.

Figure 77 Schematic diagram of an all-fiber translation optical switch.

The optical switch concept employs short (~1mm) optical fiber segments bonded to large-displacement microactuators suspended between fixed input and output optical fibers. A schematic of a typical switch is depicted in Figure 77 in its off (a) and on (b) states. As seen from this figure, the optical switch is built up with three optical fibers, one movable single mode optical fiber and two additional fixed optical fibers which may be either single-mode or multi-mode, depending upon the desired amount of optical power transmission allowed in the off and on states of the optical switch. Multimode optical fiber will makes alignment much easier, but it will also allow more light to couple through the cladding layer of the intermediate movable optical fiber compared to a single mode optical fiber. In general, the larger the core of the output multimode optical fiber, the larger the off state optical power transmission will be. The off state optical power transmission also depends on the length of the intermediate movable optical fiber.

The intermediate fiber is actuated perpendicular to the axis of the optical fiber in the horizontal plane. The length of the intermediate fiber is chosen from a combination of fabrication constraints and design considerations. While shorter fibers can enable higher-density switch arrays, this initial study employed longer fiber segments which are more readily fabricated with high precision, and which provide larger gaps between input and output fibers to ensure very low coupling efficiency during the off state of the switch. Currently, the length of the intermediate optical fibers is approximately 1mm, although shorter segments are also possible. During the switch on-state, the fiber cores are brought into coaxial alignment, with a mechanical stop used to limit the travel of the microactuator and ensure repeatable fiber alignment. Final alignment accuracy is limited by fiber diameter tolerance, rather than tolerances imposed by the microfabrication of microactuation processes.

The intermediate optical fibers are fabricated using a two-step process, which is amenable to parallel and thus cost-effective, manufacture. First, one end surface of the intermediate fiber is cleaved using a commercial optical fiber cleaver. Following cleaving, the other end is cleaved to generate a fiber segment with a length slightly larger than the desired 1mm dimension, followed by end surface polishing to reach the final length with an optical-quality surface. In this polishing process, a bundle of cleaved fibers is placed through a small aperture in a precision-milled 1 mm thick Printed Circuit Board (PCB) plate. Wax is used to hold the fibers in the hole, with one side of the plate secured against a larger aluminum block to act as a reference position for the fiber bundle as well as a holder for the polishing process. Fine alumina power (0.05μm) is used as the polishing material to make the fiber end surface optically-flat.

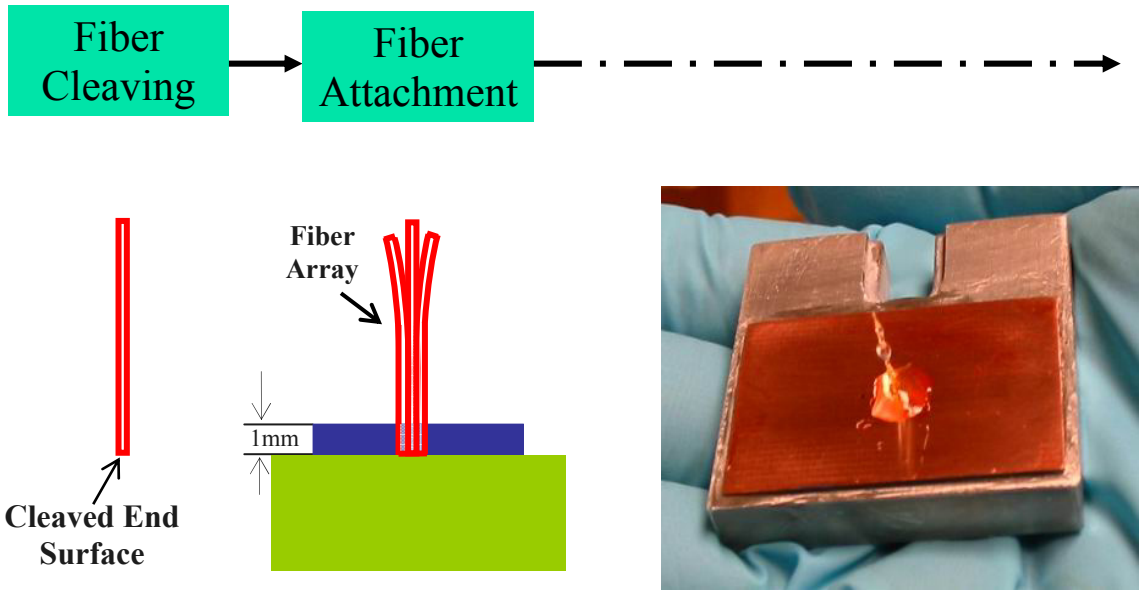

Figure 78 1mm fiber fabrication processes (1).

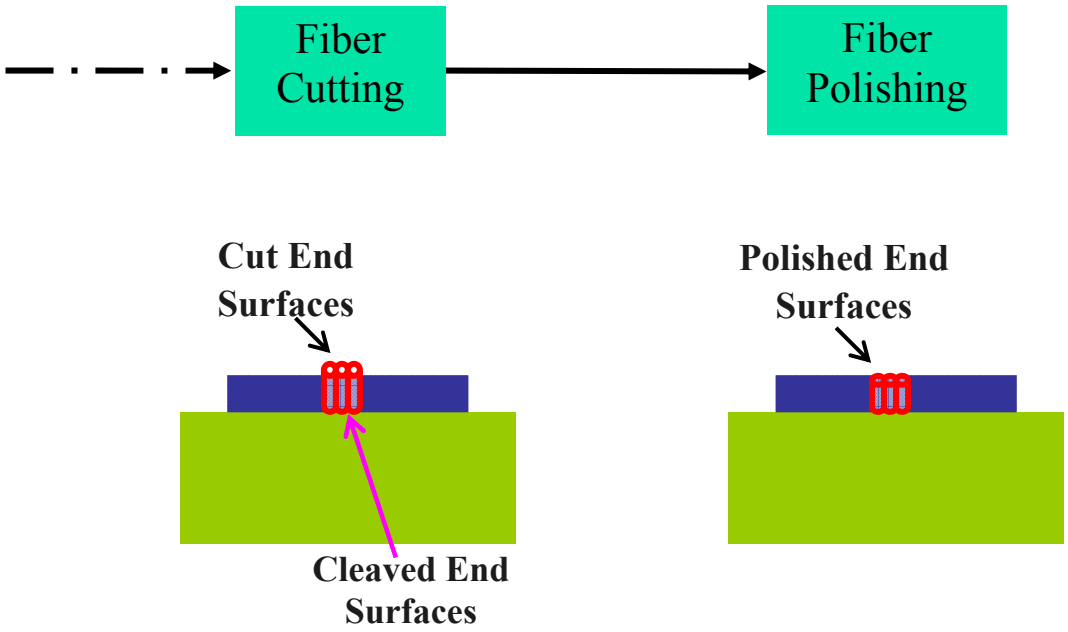

Figure 79 1mm fiber fabrication processes (2).

The silicon-based switching platform employs SOI/DRIE technology, with HF etching used to release the microactuator elements and prevent the integrated optical fibers from contacting the bottom silicon surface. To ensure optimal alignment of the fiber in the vertical direction, the intermediate actuation fiber must be integrated into the chip before HF release, resting directly on the buried S_iO_2 layer of the SOI wafer. However, since the silica waveguides will also be etched during the HF release process, it is vital that the optical fiber surfaces be protected during the etch. A combination of metal coating and thermal wax has been used to successfully protect the optical fiber form being etched by concentrated HF (49%) for more than 30 min, which is sufficient to achieve complete device release. The optical fiber body was coated with metal (100 Å Chromium / 2500 Å gold) by thermal evaporation. A rotation mechanism in the evaporator chamber was employed to evenly coat the circumference of the fiber. The optical fiber was fixed on the etched structure with a thermoset epoxy (EPO-TEK 353ND or EPO-TEK 353ND-T), which is capable of resistant to HF etching for more than 90 min, and resistant to acetone which is used to dissolve the wax following HF release. The epoxy was applied between the intermediate movable optical fiber and the actuator while the optical fiber was pushed against the top silicon sidewall of the actuator using a probe station. The epoxy is specially designed for fiber optics application with excellent chemical resistance, but requires a long cure process. To reduce residue stresses which could lead to fiber misalignment, the epoxy was gelled at room temperature overnight and put into the oven to go through three temperature ramp steps (80 Celsius, 120 Celsius, 150 Celsius; one hour for each step). After the intermediate movable optical fiber has been aligned and bonded to the silicon microactuator, wax is applied on the two end

surfaces of the intermediate optical fiber for protection. Temperature is a critical parameter to control the viscosity of the wax during the cure procedure. Under certain temperature, wax will be in the softened state and will stay at the place where it was applied. At higher temperature, wax will flow smoothly between the space under the optical fiber and above the silicon dioxide layer and will fill out the whole space. The typical temperature used through experiments was 100 ^{o}C. The wax product itself (SKYCOAT NAR-45456) is initially in a liquid state, solved into acetone. During heating, bubbles are often generated which can cause undesirable displacement of the wax. This issue can be solved by cure the wax in a vacuum oven to reduce bubble expansion inside wax. As indicated by the experiment results, the metal, wax, epoxy composition can successfully protect the intermediate movable optical fiber during the HF etching process.

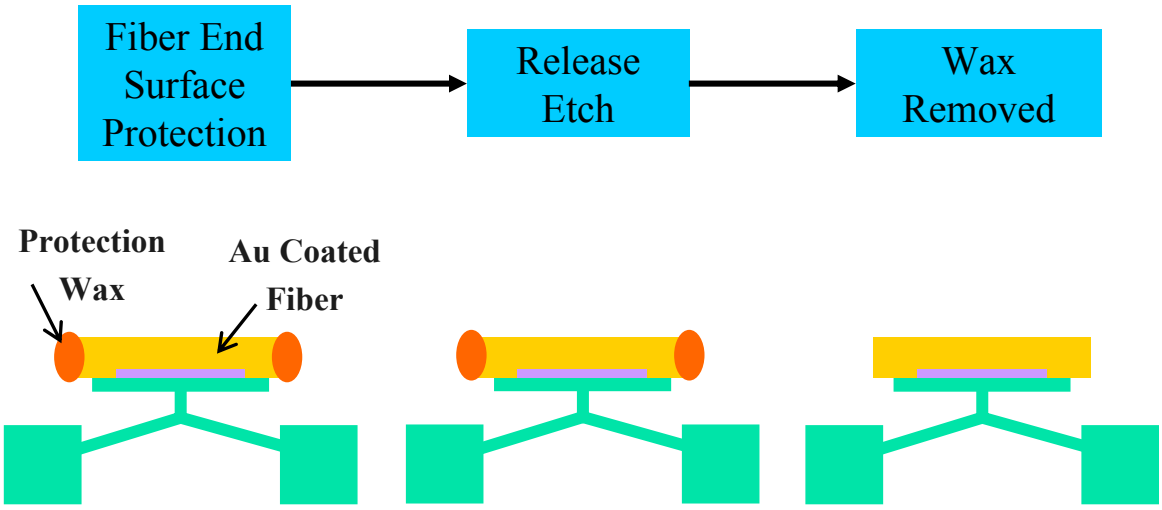

Figure 80 Fiber attaching process.

Fiber alignment was realized by top silicon sidewalls which constraint the optical fiber movement of all three optical fibers in the direction perpendicular to optical fiber

axis and within the horizontal plane. The alignment in the vertical direction was guaranteed by the top surface of the buried oxide layer. For alignment consideration, before HF etching, wax was also applied to the optical fiber channels, besides being applied on the intermediate movable optical fiber, to make sure that the input and output optical fibers are of the same level with the intermediate movable optical fiber after HF etching. The input and output fiber have not been coated as the intermediate fiber during the experiments conducted so far, but it is possible to do that in the future experiments for more critical alignment consideration.

6.2.2 Microactuator

Thermal actuator has been demonstrated as active switching elements to move the intermediate optical fiber. The thermal actuator is a V-beam thermal actuator previously explored in our group [8]. The beam width is 15μm and beam length is 2000μm. Using a current source to characterize the deflection, displacement results for a typical V-beam actuator used in this work is shown in Figure 81.

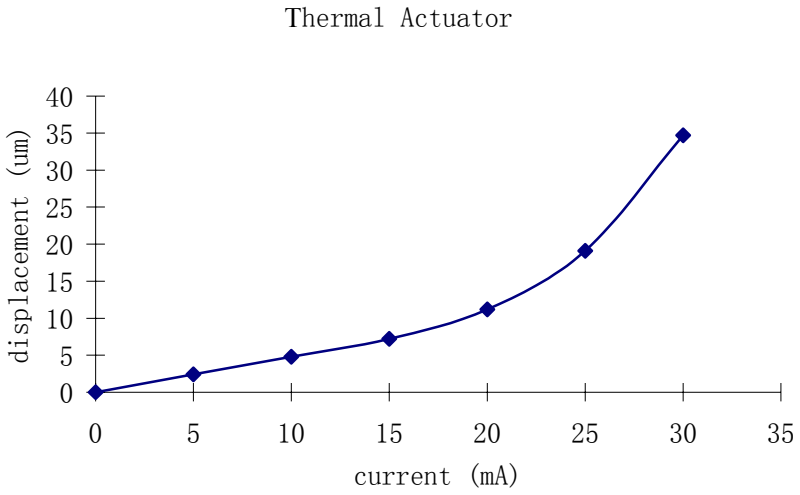

Figure 81 Thermal actuator deflection curve.

6.3 Experimental Results

All-fiber optical switches have been fabricated using the process described in the previous section. Different viscosity epoxies were used in each case. In Figure 82, a low viscosity epoxy was used, and as a result the epoxy on the surface of the actuator tended to delaminate from the microactuator. Despite this delamination, sufficient epoxy remained between the sidewall of the comb structure and the optical fiber to hold the fiber in place during testing.

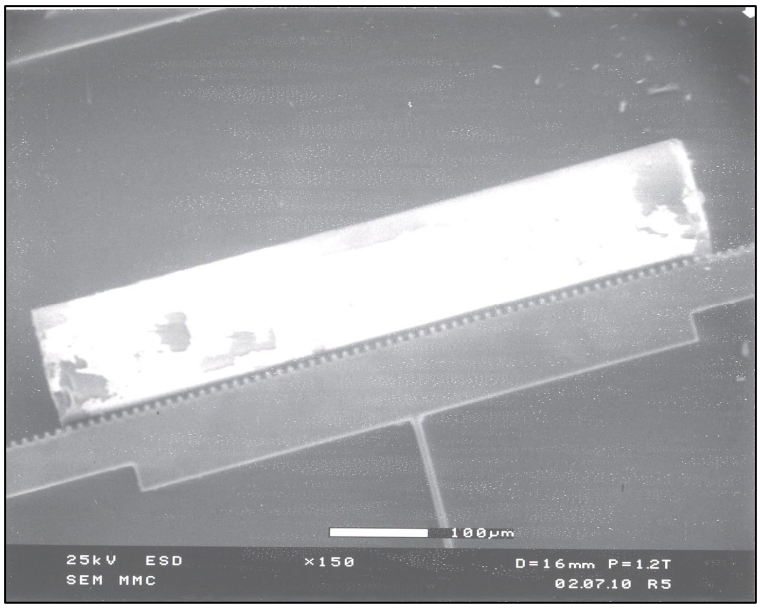

Figure 82 Micrograph of a short fiber segment bonded to the electrothermal microactuator.

Optical transmission efficiencies have been measured as a function of actuation parameters. Figure 83 and Figure 84 show the optical test setup. Light emitted from a laser light source and transmitted to the optical switch through input optical fiber. The output optical fiber transfers light from the optical switch to the power meter. Figure 83 (reverse actuation logic of Figure 77) shows the power transmission efficiency of a particular optical switch based on a thermal V-beam microactuator design. In this test, a 1 mW 1550 nm source is used to input optical power to the switch through a single-mode optical fiber. As indicated in the figure, the maximum power transmission efficiency for single mode input optical fiber, single mode intermediate movable optical fiber and single mode output optical fiber is around 30%. The off state power transmission is beyond the resolution capability (around 15µW) of the power meter used in the experiment.

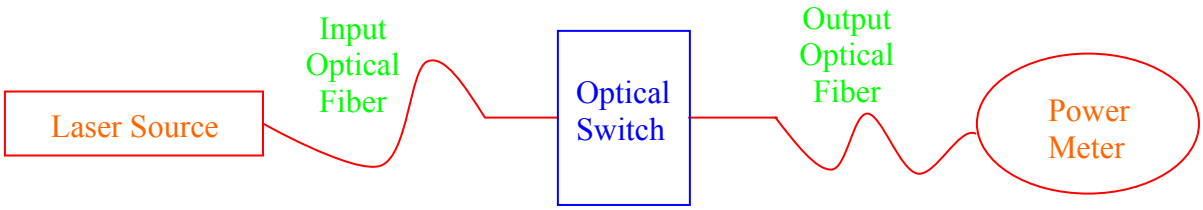

Figure 83 Optical transmission efficiency test setup (1).

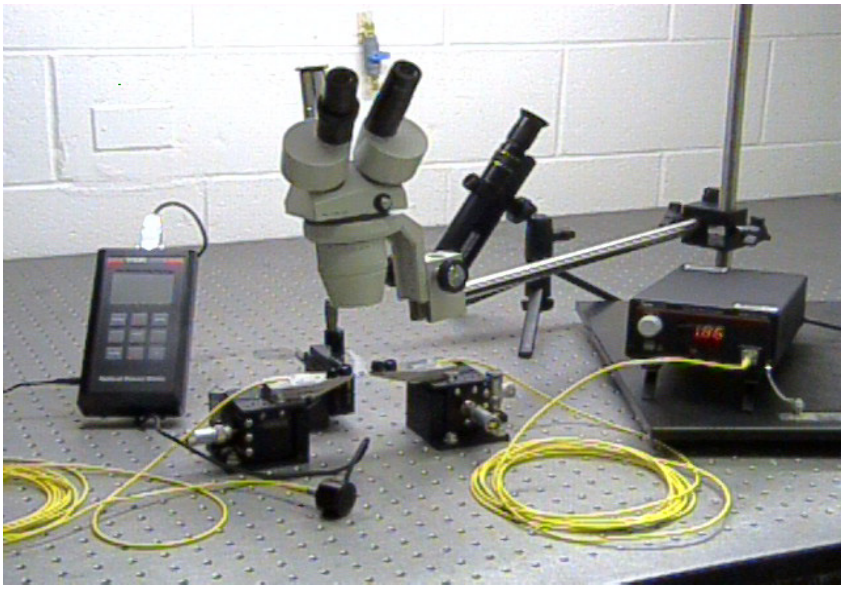

Figure 84 Optical transmission efficiency test setup (2).

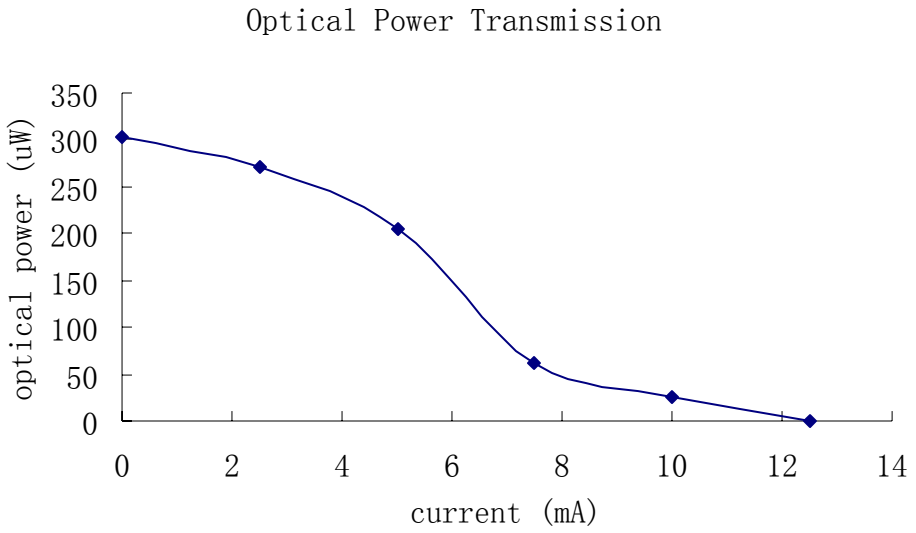

Figure 85 Optical power transmission vs. thermal actuator current.

Theoretical calculations on optical power coupling efficiency have been conducted. Coupling efficiency at a perpendicular interface is given by the Fresnel reflection loss formula [45],

$$\eta_{reflection} = 1 - \left[\frac{n_1 - n_2}{n_1 + n_2} \right]^2 \tag{6.1}$$

where n_1 is the refractive index of one medium and n_2 is the refractive index of the other.

The reflection loss at air-glass interface (n_{glass}=1.45, n_{air}=1) is 3.4%. The total refection loss accumulation on four air-glass interfaces is 13.6%.

The primary loss of the current experiment comes from the mechanical misalignment. For fiber-fiber direct coupling, there are three types of mechanical misalignment, lateral misalignment, longitudinal misalignment and angular misalignment as shown in Figure 86 [46].

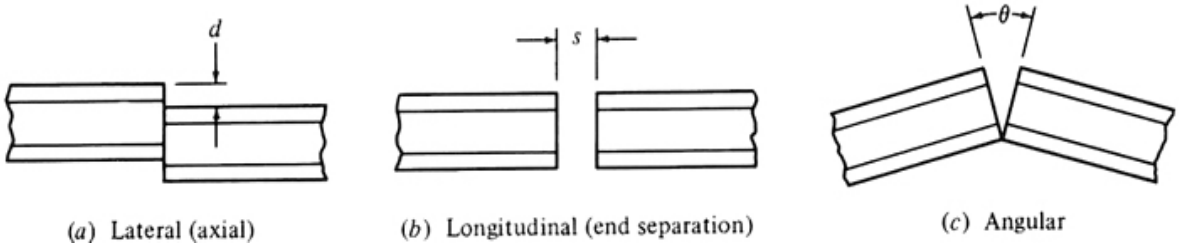

Figure 86 Mechanical misalignment of fiber to fiber direct coupling.

The main loss in the coupling experiment comes from the lateral and angular misalignment. Two equations [47] show the contribution of lateral misalignment ($L_{SM;lat}$) and angular misalignment ($L_{SM;ang}$) on power transmission efficiency.

$$L_{SM;lat} = -10\log\left\{\exp\left[-\left(\frac{d}{w}\right)^2\right]\right\} \tag{6.2}$$

where W is the mode-field radius, and d is the lateral displacement shown in Figure 86.

$$L_{SM;ang} = -10\log\left\{\exp\left[-\left(\frac{\pi n_2 W\theta}{\lambda}\right)^2\right]\right\} \tag{6.3}$$

where n_2 is the refractive index of the cladding, and θ is the angular misalignment in radians.

Based on the above two equations and from Figure 87, transmission efficiency could be seen to go down to "zero" with around either 12 μm lateral misalignment or 9^o angular misalignment. Both lateral misalignment and angular misalignment put challenge on single mode fiber to single mode fiber alignment in the experiment.

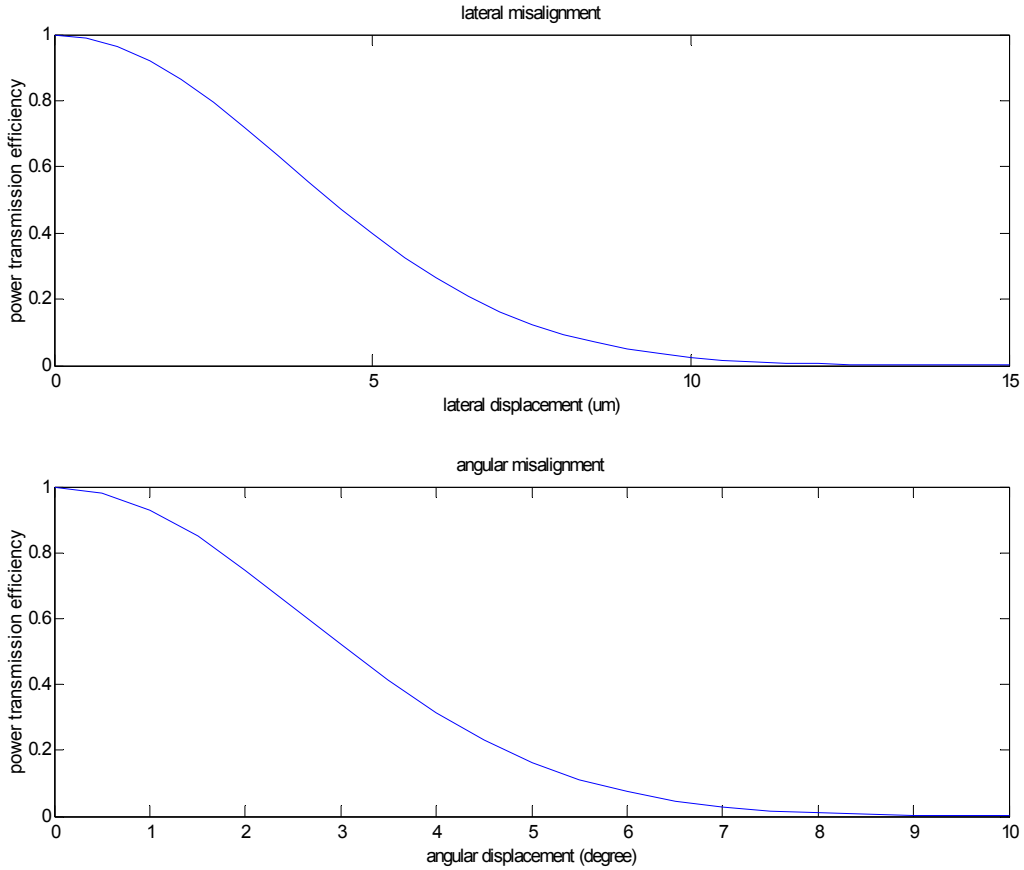

Figure 87 Power transmission efficiency vs. lateral and angular misalignment.

6.4 Discussion

The concept of an all-fiber optical microswitch, in which a short optical fiber segment bonded to a microscale actuator provides a switchable optical transfer path between input and output fibers, has been demonstrated. The fabrication process has been validated, and is conceptually amenable to massively-parallel manufacture, although additional research will be required to achieve this goal. Initial optical characterization of the switches suggests that there is significant room for improvement in power

transmission efficiency. In particular, it was found that the alignment accuracy during the bonding process is particularly critical. The main source of misalignment in current devices is that the width of the fiber channels which constrain the input and output optical fiber are slightly larger than the diameter of standard input single mode optical fiber. To improve this alignment, future switches employing tighter fiber-holding channels and mechanical "drop-out" alignment structures are currently being studied. More accurate and higher resolution equipments should also be adopted for characterization. The height of the top silicon is another important parameter, which is currently being investigated. The silicon height is critical since it affects the flow of wax during the fiber protection process, the flow of epoxy during fiber/silicon bonding, fiber alignment accuracy, and actuation efficiency.

The experiments have been done so far demonstrated the novel all-fiber MEMS optical switch concept. Some initial results have been obtained. At the same time, the experiment results posed some questions, like process optimization and optical fiber alignment improvement. Later improvement will be conducted to find solution to these questions and to reach high power transmission target.

To integrate the optical switch design with the micro time delay mechanism, the short optical fiber can be bonded either on the inertial mass that will be released by the last element of the micro time delay mechanism or be bonded directly on the last mechanism element. When the element rotate passing a specific angle the inertial mass or the last mechanism element will bring the short fiber into the position to aligned with the other two fixed fibers and close the optical route. The element locking mechanism can be used to hold the inertial mass or the last mechanism element in position so that the

movable optical fiber will be fixed after aligning with the other input and output fibers. Since either the inertial mass or the mechanism element can displace for up to approximately tens of μm, the short movable optical fiber bonded to them can be either single mode fiber or multimode fiber.

Chapter 7 – Results Summary and Future Work

7.1 Results Summary

All-mechanical micro time delay mechanisms aimed at providing arming delay and thus assuring a safe separation distance between exit from the launch barrel and arming of the munition have been designed, fabricated, and characterized. The designs of the micro time delay mechanisms came from macro scale leaf-type multiple-element time delay mechanisms. However, the leaf-type mechanism was designed to respond to munition rotation instead of a constant linear acceleration in the direction of the projectile axis as the macro scale mechanisms.

The mechanisms were designed both analytically and numerically. An all analytic model described the mechanism switching dynamics was developed. Full non-linear model considering non-linear suspension spring, friction, and air damping was developed. ODE equations of mechanism switching speed and element delay time were derived and solved numerically. Linearized model was developed for evaluation at design stage. Multiple-element vibration dynamics were simulated in ADAMS to validate the linearized model. Mechanism devices were designed based on the developed analytical model and numerical simulation results. Fabricated devices were tested on rotation platform that simulate the mechanism working environment. The switching actions of micro time delay mechanism were recorded using specifically designed high-speed camera imaging system. Fabricated mechanism arrays designed to initiate switching at centripetal accelerations from 44 to 263 g were characterized using a high-speed camera, with delay times of between 0.67 and 0.95 ms achieved for single elements within the

arrays. Element parameters optimization and scaling effects have been studied for increasing delay time of the micro time delay mechanism.

By combining the leaf-type micro time delay mechanism with run away escapement, the delay time of the micro time delay mechanism was increased approximately by twice from the dynamic simulation of specific example. The results exhibit the potential of combining other type of escapement with the current leaf-type micro time delay mechanism and extend the delay time of every mechanism element.

Two types of locking mechanisms were developed to increase the reliability of switched mechanism. The fish-bone type locking mechanism had been successfully demonstrated. The cantilever type locking mechanism could not function reliably.

An all-fiber optical switch was demonstrated to provide the possibility of closing an optical route after the last element of the leaf time delay mechanism switched.

A generic high-speed imaging system was developed to monitor and record micro-scale vibration dynamics of elements while the mechanism device rotating on the macro-scale rotation platform. The images of mechanism devices were projected from certain distance away form the rotation axis of the rotation platform to the rotation axis. The linear velocity of element was substantially reduced. Image processing techniques were used to reduce motion blur and used to assist the finding of element orientation from high-speed images.

7.2 Future Work

Increasing delay time of the time delay mechanism is necessary to satisfy

different delay time requirements for different applications. The delay time of a single mechanism element will be improved by designing more compliant suspension spring. Appending escapement mechanism with the current time delay mechanism configuration is one approach of increasing the delay time. Based on the current research work, the high-g testing environment is necessary to test the improved time delay mechanism design with runaway escapement. The shape and tolerance of the matching teeth on the pallet and the element need to be optimized to make the mechanism run smoothly yet capable of dissipating more energy within each escapement oscillation cycle. The pallet oscillation angle, the pallet moment of inertia, and the spring constant of the pallet suspension spring influence delay time of every element and pallet pair.

Compared with macro scale time delay mechanism, the micro time delay is small in dimension and fabricated using micro fabrication technology. The driving force that the last mechanism element in the chain could provide is small. Approaches need to be explored to effectively integrate with, align with, and trigger other mechanisms of the S&A system after desired delay time.

Packaging technology need to be studied to protect the micro time delay mechanism from exposing to the atmospheric environment to prevent mechanism element from sticking on the substrate, and to protect device from being damaged during the launching process. Long-term reliability should be studied to prevent element stiction and to monitor changes on element contacting surfaces.

When the high-g testing environment is setup, the high-speed camera imaging system needs to be improved to accommodate to the system changes. The changes include rotation speed increase of the rotation platform and/or larger distance from

element to rotation center of the rotation platform. In case the rotation speed is increased, the advanced high-speed camera, like Phantom V7.1 can be used in the high-speed imaging tests. Under the current testing environment, the frame rate 3,700 rps with 256×256 image resolution is the limit of the V4.0 camera. The time resolution is 0.27 ms. The V7.1 high-speed camera could take image at 27,000 fps with 256×256 image resolution. The time resolution goes to 0.037 ms. Besides, the V7.1 camera is approximately two times more sensitive than the V4.0 camera, which reduced the requirement on illumination. The optional capability of "Continuous Data Stream" of the V7.1 camera provides real time data output from the camera. There is no limitation of recording time from the high-speed camera.

References

[1] MIL-HDBK-757(AR), Military handbook, fuzes, 15 April 1994.

[2] Personal communication with Mr. Lawrence Fan, MEMS and Fuze Manager from Indian Head Division, Naval Surface Warfare Center, (IHDIV, NSWC) in Oct. 2000.

[3] C.H. Robinson, R.H. Wood and T.Q. Hoang, "Development of inexpensive, ultra-miniature MEMS-based safety and arming (S&A) device for small-caliber munition fuzes", *23rd Army Science Conference*, Co-02, 2002.

[4] A. R. Atwell, R. S. Okojie, K. T. Kornegay, S. L. Roberson, and A. Beliveau, "Simulation, fabrication and testing of bulk micromachined 6H-SiC high-g piezoresistive accelerometers," *Sensors and Actuators, A, Physical*, v.104, n.1, pp.11-18, 2003.

[5] A.R. Atwell, "Silicon carbide MEMS devices for harsh environments", *Ph.D. Dissertation*, Cornell University, 2002.

[6] D. Jean, "Integrated MEMS mechanical shock sensor", *48th Annual Fuze Conference*, 2004.

[7] M. Deeds, "Miniature flow sensor for use as a S&A second environment sensor", *47th Annual Fuze Conference*, 2003.

[8] K. R. Cochran, "Development of a micro optical switch Fabricated by deep reactive ion etching (DRIE) for high-power transfer applications", *M.S. Thesis*, University of Maryland, College Park, 2003.

[9] J. Hendershot, "Weapon fuzing / safety & arming technology program overview", *48th Annual Fuze Conference*, 2004.

[10] M. Madou, "Fundamentals of microfabrication", CRC Press, Boca Raton, FL, 1997.

[11] W. E. Ryan, “Rotary-type setback leaf S&A mechanisms, analysis and design,” Technical Report, HDL TR1190 (U-149244), Harry Diamond Laboratory, Adelphi, MD, Feb. 1964.

[12] J. Liu, L. Fan, D. DeVoe, “SOI/DRIE all-fiber optical switch for high-power applications”, SPIE Micromachining and Microfabrication, Vol. 4983, 2002.

[13] M. E. Anderson, “An analysis of the runaway escapement as a mechanical Acceleration-Integrator,” Masters Thesis, University of California at Los Angeles, June, 1966.

[14] L. P. Farace, “Runaway escapement redesign M125A1 modular booster,” Technical Report, ADA0097733, Frankford Arsenal, Philadelphia, PA. Dec 1974

[15] G. Lowen, and F. Tepper, “Dynamics of the pin pallet runaway escapement,” Technical Report, ADB0289355, Army Armament Research and Development Command Dover NJ, June 1978.

[16] A. C. Wang, and T. W. Lee, “On the dynamics of intermittent-motion mechanisms. Part2: geneva mechanisms, ratchets, and escapements,” J. Mechanisms, Transmissions, and Automation in Design, Vol. 150, pp. 541-551, 1983.

[17] M. G. Orrell, “MC2969 escapement study,” Technical Report, SAND84-0193, Sandia National Labs., Albuquerque, NM, June, 1984.

[18] L. P. Farace, “A gearless safe and arming device for artillery firing (program summary and mathematical analysis),” Technical Report, ADA0412981, Frankford Arsenal, Philadelphia, PA. Sep. 1975.

[19] M. Kenig, “Failure analysis of gearless safety and arming device,” Technical Report, AD7800147, Frankford Arsenal, Philadelphia, PA, Nov. 1973.

[20] N. Czajkowski, “A theoretical and experimental analysis of the dynamics of Junghan's escapement,” Masters Thesis, University of Maryland, College Park, June, 1955.

[21] K. Schulgasser, and C. Dock, “Development of the dock escapement,” in Proc. of the Timers for ordnance Symposium, Vol. 1, pp. 15-34, Harry Diamond Laboratory, Adelphi, MD, Nov. 1966.

[22] D. Popovitch, Timing escapement mechanism, U.S. Patent 3,168,833, Picatinny Arsenal, Dover, NJ, Feb. 1965.

[23] R. W. Baker, “Analysis of a rotary-type, multiple leaf, setback sensor for a safety and arming mechanism,” Masters Thesis, University of Rhode Island, June 1977.

[24] K. Cochran, L. Fan, D.L. DeVoe, “High-power optical reflector microswitch for safety and arming applications,” *J. Micromech. Microeng.*, v.14, n.1, pp.138-146, 2004.

[25] L. Fan, H. Last, R. Wood, B. Dudley, C.K. Malek, Z. Ling, "SLIGA based underwater weapon safety and arming system," *Microsystem Technologies*, vol. 4, pp. 168-171, 1998.

[26] A. Hausner, “An analysis of friction in a T293 setback leaf system,” Harry Diamond Labs, Washington D. C., Tech. Rep. AD602624, 1960.

[27] G. D. Aydlett, “A review of George Graham’s classic escapement, or Dead-beat by design”, Columbia, Pa. : National Association of Watch and Clock Collections, 1973.

[28] J. H. Bickford, “Mechanism for intermittent motion”, Industrial Pres, New York, 1972.

[29] F. G. Kelly and J. L. Zar, “An improved fuze escapement for the Mark 18 and other

U. S. Navy mechanical time fuses", *Journal of Applied Mechanics*, vol. 13, pp A285-A290, 1946.

[30] S. B. Tuttle, "Mechanisms for engineering design", Wiley, New York, 1967.

[31] Balakumar Balachandran, E. B. Magrab, "Vibrations", Pacific Grove, Calif.: Brooks/Cole, 2003.

[32] S. M. Barnes, S. L. Miller, M. S. Rodgers, and F. Bitsie, "Torsional ratcheting actuating system," in *Proc. MSM 2000*, San Diego, CA, Mar. 27-29, 2000, pp 273-276.

[33] W. O. Davis, "Mechanical analysis and design of vibratory micromachined gyroscopes," Ph.D. Thesis, University of California, Berkeley, 2001.

[34] B. Bhushan and X. Li, "Micromechanical and tribological characterization of doped single-crystal silicon and polysilicon films for microelectromechanical systems devices," *J. Materials Research*, vol. 1, pp. 54-63, 1997.

[35] A. Padmanabhan, "Silicon micromachined sensors and sensor arrays for shear-stress measurements in aerodynamic flows," Ph.D. Thesis, Massachusetts Institute of Technology, 1997.

[36] S. S. Rao, "Mechanical vibrations," 3rd ed., Addison-Wesley, Reading, Massachusetts, 1995.

[37] N. Maluf, "An introduction to microelectromechanical systems engineering", Artech House, Boston, Massachusetts, 2000.

[38] O. Gigan, H. Chen, S. Renard, and F. Marty, "Fabrication and characterization of resonant SOI micromechanical silicon sensors based on DRIE micromachining, freestanding release process and silicon direct bonding", *Proceedings of SPIE - The*

International Society for Optical Engineering, v 4936, 2002, p 194-204.

[39] F. F. Sherman, "In-plane microactuators for fluid control application and radio frequency (RF) signal switching", *Ph.D. Dissertation*, University of California, Los Angels, 1998.

[40] C.H. Robinson, R.H. Wood and T.Q. Hoang, "Development of Inexpensive, Ultra-miniature MEMS-based Safety and Arming (S&A) Device for Small-caliber Munition Fuzes", *23rd Army Science Conference*, Co-02, 2002.

[41] C. R. Brooks, and Ashok Choudhury, "Failure Analysis of Engineering Materials", *McGraw-Hill*, New York, 2002.

[42] J. C. Russ, "The Image processing Handbook", 3rd Edition, *CRC Press LLC*, 1998.

[43] J. C. Russ, "The Image processing Handbook", 1st Edition, *CRC Press LLC*, 1992.

[44] P. Tuft, "The radon transform – theory and implementation", *Ph.D. Dissertation*, Technical University of Denmark, 1996.

[45] J. P. Powers, "An introduction to fiber optic systems", Richard D. Irwin, Inc., and Aksen Associates, Inc., 1993.

[46] G. Keiser, "Fiber-Optic Communication Systems", 3rd Edition, *Govind Agrawal, Wiley*, 2000.

[47] D. Marcuse, D. Gloge, and E. A. J. Marcatili, "Guiding properties of fibers", in S. E. Miller and A. G. Chynoweth, eds., Optical Fiber Telecommunications, Academic New York, 1979.